AAEC/E334

AAEC/E334

AUSTRALIAN ATOMIC ENERGY COMMISSION

RESEARCH ESTABLISHMENT

LUCAS HEIGHTS

DENSE PLASMA FOCUS – A LITERATURE REVIEW

by

JOHN TENDYS

January 1976

ISBN 642 99696 2

AUSTRALIAN ATOMIC ENERGY COMMISSION
RESEARCH ESTABLISHMENT
LUCAS HEIGHTS

DENSE PLASMA FOCUS - A LITERATURE REVIEW

by

JOHN TENDYS

ABSTRACT

The dense plasma focus (DPF) is a convenient source of short, intense neutron pulses, and dense, high temperature plasma. This review of the literature on the DPF indicates that its operation is still not understood, and attempts to show where the present data is either inadequate or inconsistent. Because the plasma conditions and neutron and X-ray fluxes vary from shot to shot, it is maintained that, to resolve inconsistencies in the present data, spectra need to be measured with energy and time resolution simultaneously, and cannot be built up from a large number of shots. Time resolutions of the order of 1 nsec for pulse lengths of about 100 nsec make these requirements especially difficult. Some theoretical models are presented for the neutron output and its spectrum, but no self-consistent description of the plasma in the focus region is likely for some time.

National Library of Australia card number and ISBN 642 99696 2

The following descriptors have been selected from the INIS Thesaurus to describe the subject content of this report for information retrieval purposes. For further details please refer to IAEA–INIS–12 (INIS: Manual for Indexing) and IAEA–INIS–13 (INIS: Thesaurus) published in Vienna by the International Atomic Energy Agency.

COMPUTER CALCULATIONS; MATHEMATICAL MODELS; NEUTRON EMISSION; NEUTRON FLUX; NEUTRON SOURCES; NEUTRON SPECTRA; NEUTRONS; PLASMA FOCUS; PLASMA FOCUS DEVICES; REVIEWS; TIME RESOLUTION; X–RAY SPECTRA

CONTENTS

(continued)

CONTENTS (continued)

1. INTRODUCTION

Coaxial accelerators were studied for many years in the puffed-gas mode [Marshall 1960; Butler, Cook & Morse 1968] to obtain a burst of plasma moving at high velocity for injection into various experimental fusion machines. Operation with a static filling was carried out initially to study the acceleration process [Patrick 1959]. This second mode of operation with higher pressures led to a high density plasma region at the end of the centre electrode [Mather 1963, 1964] called a dense plasma focus (DPF). No longitudinal magnetic field was applied in this mode. When a filling of deuterium or deuterium-tritium mixture was used, the DPF was found to be a high intensity source of neutrons (around 10^{10} neutrons per shot) in a short burst (typically lasting 100 nsec).

There are two major designs for the plasma focus gun, namely the Mather and the Filippov types. In the Mather design, the coaxial electrodes are longer than their diameter and there is a distinct constant velocity run-down stage for the discharge. On the other hand the Filippov type has an electrode with a length similar in size to its diameter; the outer electrode forms the outside wall and end of the discharge vessel. The centre electrode has an insulator over its whole length and the discharge occurs between the end of the electrode and walls of the vessel. The focus for the two types of gun appears to be similar. (A dense plasma region can occur also for the pulsed gas mode [Vasileva, Pergament & Yaroslavski 1969], but it is much smaller since the amount of gas involved is much less.)

There has been considerable interest in intense pulsed sources of neutrons for high resolution time-of-flight studies in solid state physics, nuclear physics and reactor engineering [USAEC-LASL 1966]. The DPF has the advantages of neutron fluxes greater than 10^{17} neutron sec^{-1}, and relatively low cost; however, it has only small average fluxes owing to the low repetition rates (typically one shot every few minutes).

Much effort is being allocated to finding the scaling laws for the neutron output with various input parameters, especially the input energy. If the scaling laws found at low energies hold at much higher energies, and the repetition rate is increased, the DPF will be a competitive neutron source. To study these two factors, a joint program has been set up by the laboratories at Culham, Jülich and Frascati* to build a facility capable of 1 MJ. Initially, this project will use a Filippov gun [Maisonnier *et al.* 1972].

---

* *Culham Laboratory, Abingdon, United Kingdom; Institut für Plasmaphysik der KFA, Jülich, West Germany; Laboratori Gas Ionizzati, Frascati, Italy.*

Other methods for increasing the energy input into the focus include the input of currents of 2 MA or more from explosively-driven generators [Bernard *et al.* 1971(b)], and the direct addition of energy into the focus with a pulsed electron beam [Freiwald *et al.* 1971]. The results obtained so far are inconclusive.

The high temperature obtained (at least 2 keV) makes the focus a useful source for the study of spectroscopic lines in the soft X-ray region (1 to 30 Å) from high ionisation states, *e.g.* Argon XVII [Peacock, Speer & Hobby 1969]. Vacuum spark gaps and various plasma devices allow the study of lines up to several hundred electron volts but, in the plasma focus, optical transitions can be obtained up to 4 keV. This is a much higher energy than had been obtained in the laboratory previously, especially for the inert gases which are difficult to excite. These lines have astrophysical importance (*e.g.* for solar flares) but, owing to a lack of laboratory data, they have been difficult to identify.

During the late stages of the operation of the gun, a jet is formed on the axis in front of the centre electrode. It is maintained by the flow of magnetised plasma remaining in the gap between the electrodes after the initial front has passed. It was found that such a jet could be maintained for around 100 μsec, with a negative centre electrode, by a suitable addition of gas [Henins, Marshall & Newton 1968]. This jet was called a continuous flow pinch, and the temperature and streaming energy were around 100 eV. A simple fluid model indicated that any temperature could be obtained by the suitable choice of current and filling density, and that the flow pinch is stable to various instabilities which disrupt the usual Z-pinch. Hence, it was considered as a possible candidate for a thermonuclear fusion reactor if the jet could be made sufficiently long [Newton 1968; Morozov 1969].

The possibility of producing thermonuclear temperatures in such a pinch flow device was apparently strengthened by the neutron emission from the DPF [Morozov 1968; Henins, Marshall & Newton 1968]. As will be seen in Section 5, it now seems most likely that the neutron emission in a DPF occurs as a transient condition during the establishment of such a flow. This stage of the DPF will not be discussed further, since very little work has been done on it. The simple fluid model referred to above may not be reliable, since several other computer simulation studies do not agree with it [Butler, Cook & Morse 1967].

In this review, a general survey is given of the experimental results obtained to 1972 and the theories to explain various features of the plasma

focus. A critical analysis of the experimental data is not possible, since very few reports contain sufficient detail of the conditions under which experimental data were obtained.

Brief notes are made of the main diagnostic methods so far applied to the focus, and their limitations in relation to the non-reproducibility of the focus from shot to shot, its very short life and its small size (1 mm dia. x 20 mm long). Ideally, all the measurements should be made for a given spectrum on one discharge.

The observations made with fast image converter cameras can be difficult to interpret, but they do give an approximate picture of the events during the discharge. The range of the camera can be extended into the X-ray region by observing the image formed on a thin scintillator screen. The number of frames which can be obtained per shot is normally small so only short periods can be observed of any given event, although they have good space and time resolution.

Similar problems hold for pulsed, laser interferometry and Schlieren photography which are used to obtain densities and density gradients. Exposures of 1 nsec are possible, but the number of frames is typically three with a separation of 5 to 10 nsec.

Probe measurements have proved possible during the acceleration and run-down phases but not during the focus. At the latter time, the high temperatures and electric fields destroy the probe.

Spectral observations of the current sheath are possible in the visible portion of the spectrum if gases heavier than D_2 or H_2 are used, and some temperatures have thus been deduced. It has not been possible, so far, to obtain X-ray spectra of sufficient energy resolution because of the large number of recording channels required, and it is not possible to build up the spectrum using many shots. Similarly, only time-resolved neutron fluxes have been obtained. Neutron spectra have been obtained with nuclear emulsions.

The usual operation of the gun is with the centre electrode as the anode and most results refer to this mode. Some reports claim that there is little difference if the centre electrode is the cathode, while others find a very marked reduction in neutron output. Furthermore, there are many variations of the two basic forms of the gun with slight modifications of the inner and outer electrode geometries. These do not seem to affect most features of the DPF and, in this review, there will be reference only to a particular polarity or geometry should the results differ in this case. Otherwise, it is presumed that all variants give similar results.

The review is divided into several sections which correspond roughly to different diagnostic techniques; since different techniques are required for different stages, the sections also correspond to descriptions of the various stages of the discharge. Section 2 deals mainly with the current sheath in the run-down stage as observed by optical and probe measurements. The collapse stage of the current sheath as observed in visible light and with laser pulses is considered in Section 3, while Section 4 deals with the X-ray emissions. Section 5 discusses neutron emission and together with Section 4 offers some immediate interpretations of the data, with the more detailed theories being left to Section 6.

2. THE RUN-DOWN STAGE

2.1 Apparatus

The Mather plasma focus gun [Mather 1965] consists of two coaxial electrodes connected to an electrical energy source, usually a capacitor bank working in the range 14 to 50 kV (Figure 1). The electrodes are typically 20 cm long, with the centre and outer electrodes having diameters

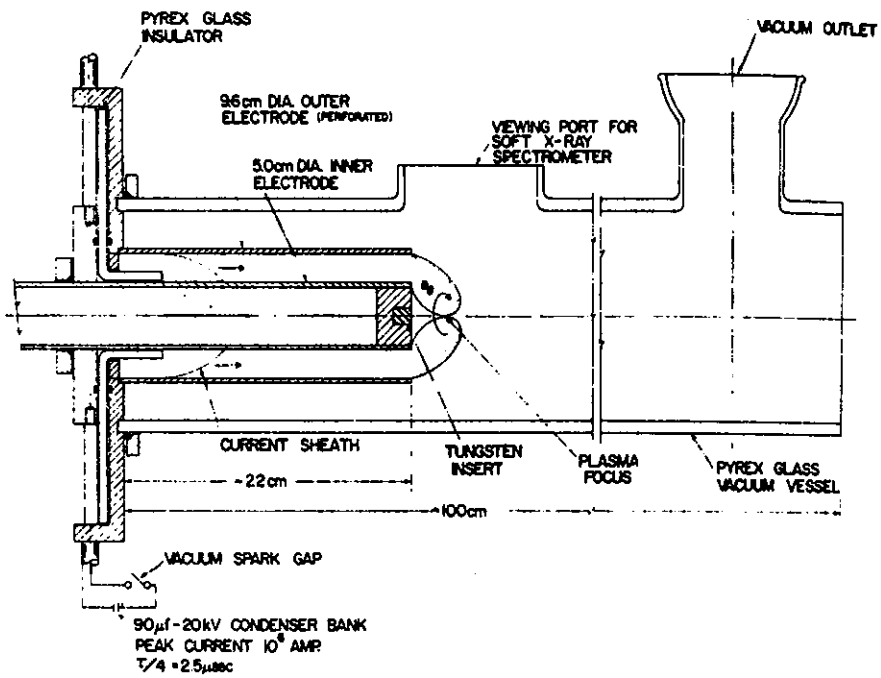

FIGURE 1
Schematic representation of the dense plasma focus apparatus
(Source: Mather & Bottoms 1968)

of 5 cm and 10 cm respectively. As the operating voltage is increased it is necessary to increase the size of the gun also, otherwise difficulties arise from arcing and 'restrikes' between the electrodes after the initial breakdown. At the breech end, the electrodes are separated by a Pyrex glass or ceramic insulator which has a sleeve for some distance over the inner electrode. This

distance is usually about 5 cm but, as the voltage is raised, it must be lengthened to avoid restrikes along the glass during the discharge (for example, at 50 kV it is 10 cm).

Since the coaxial gun has an inductance of the order of 40 nH, it is necessary for the capacitor bank and connecting cables to have a smaller inductance so that much of the applied voltage will appear across the gun. A typical value is 15 nH; this needs to be modified for the higher voltages, since there is apparently an upper limit (which depends on the particular machine) to the voltage that should be applied to the gun.

The cables from the capacitor bank need to be resistively terminated at the gun to help damp persistent oscillations, which are due to stray capacitances and inductances produced when the apparatus is switched on, and also to match the cable and gun impedances [Mather *et al.* 1971].

The outer electrode is perforated to allow some degree of observation from the side and the centre electrode has a heavy metal insert (*e.g.* tungsten) to reduce the erosion from electron bombardment.

Variants of the basic plasma gun either replace the outer electrode with a small number of rods [Bernard, Coudeville & Watteau 1970] or open it out to a flat plate at the back of the gun [Butler *et al.* 1969] (Figure 2).

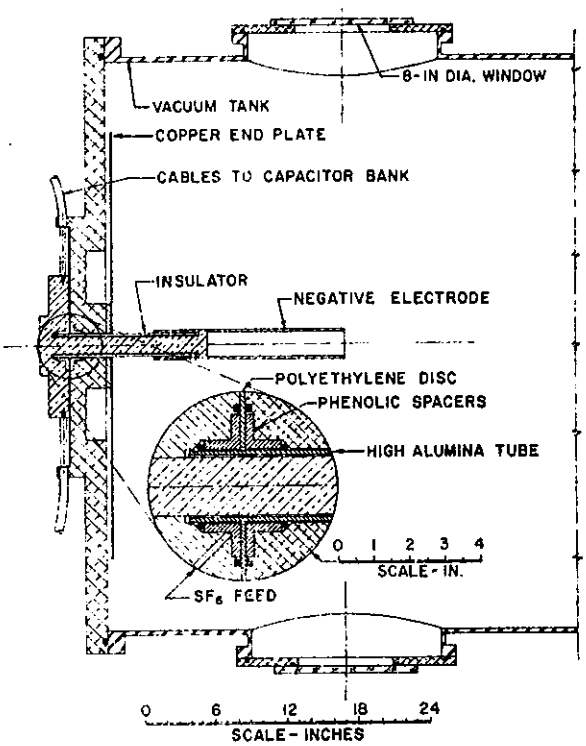

FIGURE 2
Experimental arrangement
(Source: Butler et al. 1969)

The Filippov gun has the insulator covering the whole of the centre electrode except its end, and the wall of the vacuum chamber is made of metal to act as the outer electrode as shown in Figure 3 [Petrov *et al.* 1960; Filippov, Filippova & Vinogradov 1962]. The general dimensions tend to be much larger than the Mather gun, *e.g.* the centre electrode diameter of 100 cm for the experiment described by Filippov *et al.* [1971]. The properties of the focus are apparently independent of the gun type; most of the published results were obtained on a Mather gun.

The gun is filled to a static pressure of 1 to 10 torr, usually with hydrogen or deuterium. When the voltage is applied between the electrodes,

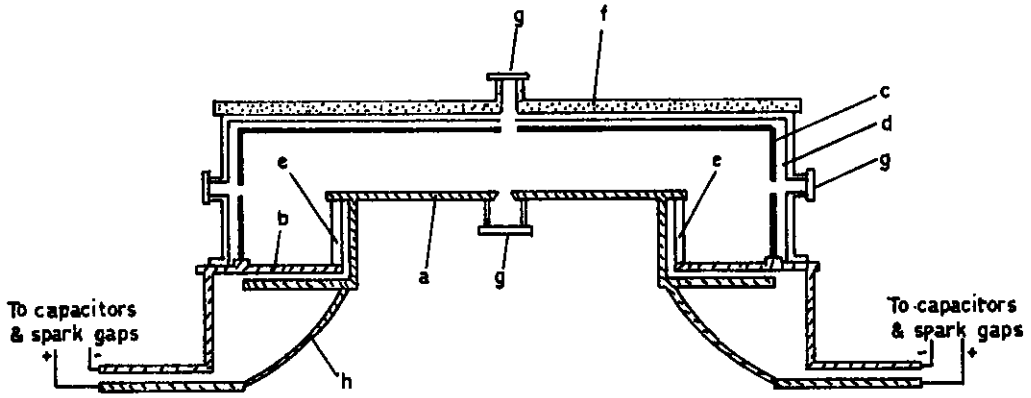

a	anode	e	porcelain insulator
b	cathode	f	vessel lid
c	liner	g	viewing ports
d	liner insulation	h	variable inductance

FIGURE 3
Schematic arrangement of the Filippov gun

breakdown occurs across the insulator. The self-magnetic field, B_θ, interacts with the current to drive this current sheath away from the insulator as an inverse pinch, and then along the annular space between the electrodes. When the current sheath reaches the end of the centre electrode, the gas collapses under the magnetic pressure to a line focus off the end of the electrode. This region has a high temperature and density from which a very intense burst of X-rays is emitted; with a D_2 filling, a burst of neutrons is emitted also. At later times, the focus re-expands to form a hot plasma jet extending about 10 cm beyond the electrode.

2.2 The Current Sheath

The initial breakdown occurs across the insulator in the form of filaments [Mather & Williams 1966; Bostick *et al.* 1966]. These filaments are blown off the insulator by the magnetic field and, about 1 μsec after breakdown, merge to form a uniform thin parabolic current sheath between the electrodes. The experimental measurements taken on the sheath are its velocity, shape and temperature.

Observation of the current front with an image converter camera set for a 5 nsec exposure shows the near-parabolic shape, and a plume of gas issuing through the perforations in the outer electrode implies motion of the gas along the front [Mather & Bottoms 1968]. At a given voltage, when the

pressure has increased sufficiently, the breakdown filaments can easily be seen, and they maintain themselves up to the collapse stage [Bostick *et al.* 1966]. For lower pressures, the filaments merge early in the acceleration stage and only a uniform sheath propagates to the end of the gun [Mather & Williams 1966].

The initial formation of the current sheath has not been studied, so the arrangement used has been determined empirically. This seems to produce a satisfactory current sheath, but as the applied voltage increases it is found that restrikes (*i.e.* a second breakdown some time after the first sheath has left the insulator) become more frequent. When this occurs, no satisfactory focus is obtained, presumably because the second arc at the breech shorts out the gun and little energy can be delivered to the first sheath. Mather *et al.* [1971] have found that a general optimisation of the sleeve length, electrode diameters and lengths, pressure of operation and changes in the actual voltage applied across the electrodes (by introducing inductances into the cables) has allowed operation up to 52 kV bank voltage, with a production of 3×10^{11} neutrons. Apparently, good foci can be obtained if the voltage at the electrodes is kept to less than 12 kV.

The velocity of the front becomes constant shortly after establishment of the sheath between the electrodes. Over a pressure range of 50 μm Hg to greater than 1.5×10^3 μm Hg and a range of voltages and currents, the velocity varies approximately as $\rho^{-\frac{1}{4}}$ and $V^{\frac{1}{2}}$, where ρ is the filling density and V is the breech voltage.

As seen in Figure 4 (a) to (d), good agreement is obtained except for very low applied voltages (V = 8 kV for Figure 4(b) and V = 5 kV for Figure 4(c). In Figure 4(a), the velocity is measured in terms of the time taken by the sheath to get to the end of the electrode; hence the functions are inverted to become $\rho^{\frac{1}{4}}$, $V^{-\frac{1}{2}}$. In Figure 4(c), B_o is the magnetic field behind the sheath; it is related to the current I, or voltage V through the circuit parameters. When B_o is related to V, the density factor becomes $\rho^{-\frac{1}{4}}$ because I as a function of V contains the sheath velocity). The deviations from the theory of the measurements are apparently dependent on the experimental situation and do not follow a consistent pattern.

In the system having no outer electrode [Butler, Cook & Morse 1969], reasonably good agreement is found for pressures of 80 μm to 500 μm and voltages up to 20 kV (Figure 4(d)).

The prediction that the velocity should vary with $\rho^{-\frac{1}{4}}$ and $V^{\frac{1}{2}}$ (or with B_o, *i.e.*I and $\rho^{-\frac{1}{2}}$) comes from the two-dimensional 'snowplough' theory. It will

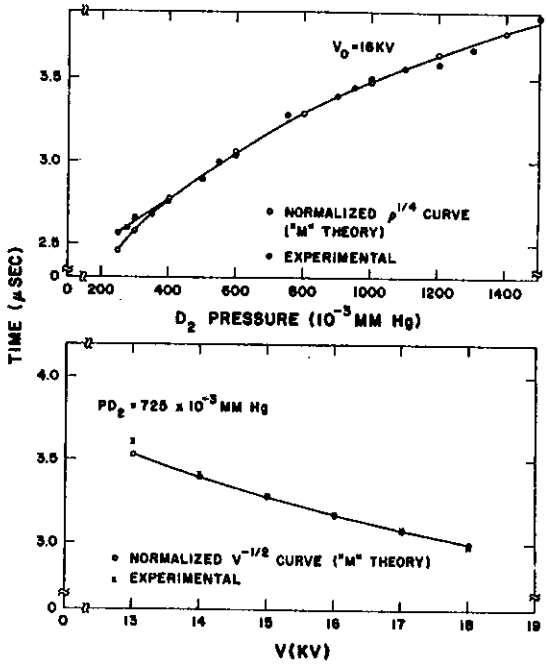

(a) Time to current singularity vs pressure and voltage. (Source: Mather 1965)

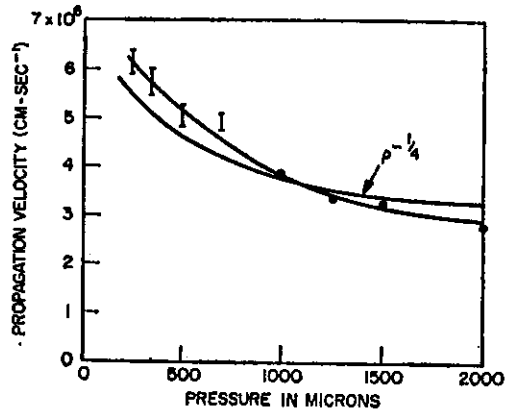

(b) Propagation velocity of luminous front as a function of helium gas pressure. (Source: Lie et al. 1967)

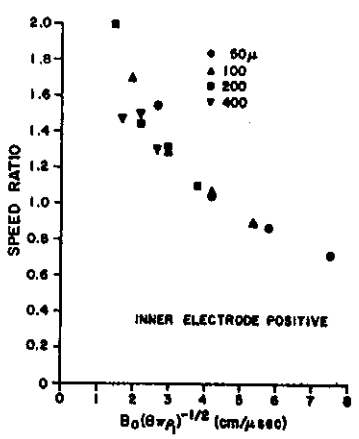

(c) Ratio of the speed of the current sheet observed by Keck to the speed $u_S = B_0(8\pi\rho_1)^{-1/2}$ plotted against the latter speed. The points are coded according to the gas pressure (in microns) in the tube before the discharge. (Source: Fishman & Petschek 1962)

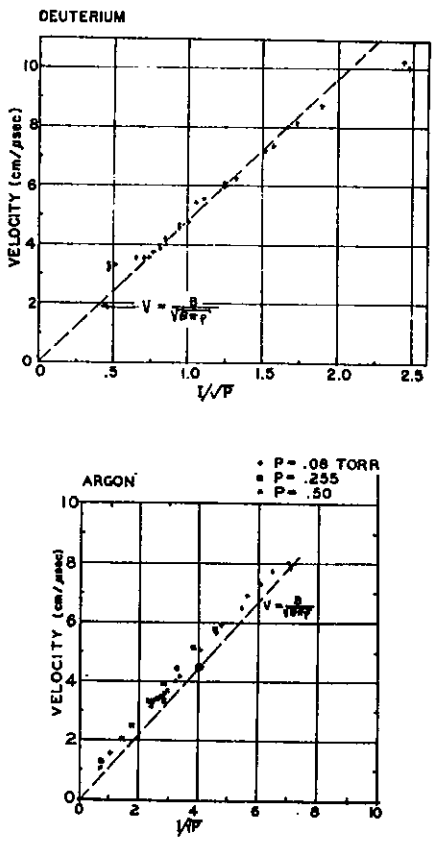

(d) "Snowplow" velocity measurements in deuterium and argon. The velocity was changed by changing the ambient gas pressures, except in the case of argon where gas pressure was set and the current was changed by applying different voltages from the capacitor banks. The absissa values are relative and proportional to $B/(8\pi\rho)^{1/2}$. (Source: Butler et al. 1969)

FIGURE 4(a) – (d)

be seen, from the assumptions below, that it is not surprising that there can be considerable disagreement with the experimental results.

The analytical model for the current sheath has been formulated in various ways [Fishman & Petscheck 1962; Butler, Cook & Morse 1969; Potter 1970], but the major assumptions made are:

(a) Fluid equations can describe the flow, since the ion-ion collision length is short compared to the shock thickness.

(b) The plasma conductivity is infinite, so the driving current flows in a thin layer separating magnetic field and plasma. This is a reasonable assumption since the magnetic Reynolds number R_m is large (to obtain reasonable values of quantities for the plasma gun, $R_m > 15$).

(c) Time independence - this is justified by the experimental observation that after about 1 μsec the current sheath has a constant velocity and shape.

(d) Cylindrical symmetry.

(e) A one-fluid model is adequate since the ion-electron collision time is very short at the temperatures encountered (2 eV to 50 eV).

In a reference frame moving axially with the shock, the undisturbed gas flows uniformly in the z-direction towards the shock. When the gas strikes the shock, its momentum is altered and it is carried by the flow along the shocked layer (which is assumed to be very thin). No gas penetrates through the current sheath. The conservation equations [Butler, Cook & Morse 1969] are:

$$\frac{B_o^2 r_o^2}{8\pi r^2} - \rho u^2 \cos^2\theta + \frac{\sigma v^2}{2\pi r}\frac{d\theta}{ds} = 0 \quad , \qquad \ldots(1)$$

$$\frac{d}{ds}(v\sigma) = 2\pi r u \rho \cos\theta \quad , \qquad \ldots(2)$$

$$\frac{d}{ds}(v^2\sigma) = 2\pi r u^2 \rho \cos\theta \sin\theta - 2\pi r \frac{dP}{ds} \quad , \qquad \ldots(3)$$

and

$$\frac{d}{ds}(v\varepsilon) = \frac{2\pi r u \rho}{2\gamma} \cos\theta \{u^2\cos^2\theta + (u\sin\theta - v)^2 - u_c^2\} + \frac{2\pi r \delta}{\gamma}\frac{dP}{ds} \quad , \qquad \ldots(4)$$

where s is the arc length along the shock from the centre electrode;

r_o is the centre electrode radius;

B_o is the azimuthal magnetic field at r_o behind the shock;

ρ is the mass density ahead of the shock;

u is the flow velocity of the undisturbed gas (*i.e.* the negative of the axial shock velocity);

θ is the angle made by the shock surface with the local radius;

v is the velocity of flow in the shock layer;

σ is the mass per unit arc length (integrated with respect to the azimuthal angle around the axis);

ε is the internal energy per unit arc length;

u_c is the velocity at which the kinetic energy equals the ionisation energy;

γ is the ratio of specific heats ($\gamma = 5/3$ is used here);

δ is the shock thickness; and

P is the pressure in the shocked layer.

The internal energy per unit volume $\varepsilon/2\pi r\delta$ is related to the pressure through

$$P = \frac{(\gamma-1)\varepsilon}{2\pi r\delta} \quad ,$$

and the pressure P is taken to be the average of the kinetic pressure on the front and the magnetic pressure on the back

$$P = \tfrac{1}{2}(\rho u^2\cos^2\theta + \frac{B_o^2 r_o^2}{8\pi r^2}) \quad .$$

If the pressure and internal energy are neglected and the centrifugal term $d\theta/ds$ in Equation (1) is assumed small (since the sheath curvature is small except near the electrode), then the sheath shape $Z(r)$ and the velocity U_s of the shock are given by the equation of Fishman & Petscheck [1962]

$$Z(r) = \tfrac{1}{2}r_o\{\, r/r_o\, [(r/r_o)^2-1]^{\frac{1}{2}} - \ell n\,(r/r_o + [(r/r_o)^2 - 1]^{\frac{1}{2}})\, \} \quad , \qquad \ldots(5)$$

and

$$U_s = \frac{B_o}{(8\pi\rho)^{\frac{1}{2}}}$$

for constant current I, *i.e.* constant B_o.

For the assumption of constant voltage V, Potter [1970] derives

$$U_s = (2\mu_o\rho)^{-\frac{1}{4}}\ (r_o\ \ell n\ \frac{r_2}{r_o})^{-\frac{1}{2}}\ V^{\frac{1}{2}} \quad ,$$

where $\mu_o = 4\pi \times 10^{-7}$ H m^{-1}; and

r_2 = radius of the outer electrode for a coaxial system.

This analytical solution is independent of the thickness of the shock,

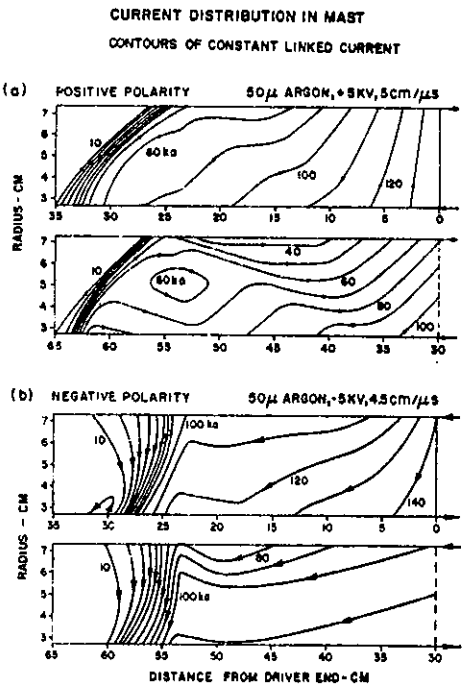

(a) Contour plots showing current distribution for positive and negative centre electrode. Note that the axial scale of the figure has been compressed by a factor of 2. (Source: Keck 1962)

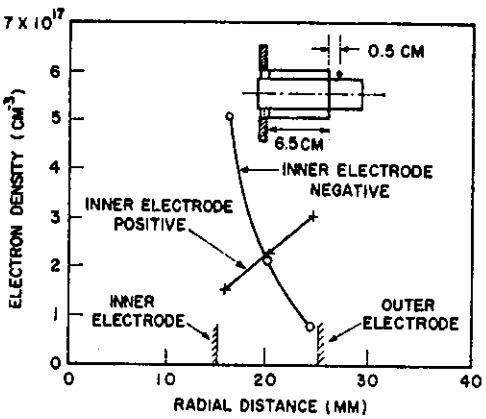

(b) Radial distributions of electron density for both electric polarities at 0.5 cm from outer electrode. Insert shows the accelerator geometry. (Source: Lie et al. 1967)

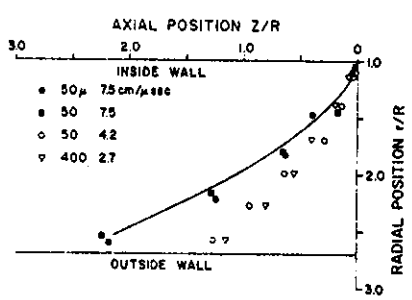

(c) Comparison of the shape of the current sheet observed by Keck with Eq. (4). The experimental positions were taken to be the points of maximum current density. The code indicates the gas pressure (in microns) in the tube before the discharge and the speed computed from Eq. (3) corresponding to the initial conditions. All observations were made at a station 60 cm down the tube except those represented by the squares, which were made at 30 cm. (Source: Fishman & Petscheck 1962; Eq. (3) & (4) are from this source).

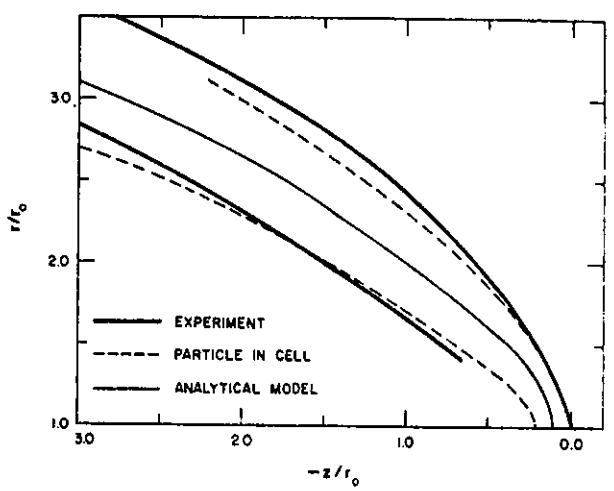

(d) Sheath shape comparison of experiment with particle-in-cell calculation and analytical model predictions during equilibrium phase. Dimensions are scaled to the electrode radius r_0. (Source: Butler et al. 1969)

FIGURE 5(a) – (d)

and does not distinguish whether the centre electrode (CE) is positive or negative. As seen above, the velocity is predicted with reasonable accuracy by the theory for a range of pressures and voltages.

For the coaxial-electrode system, there is a difference between the shapes of the front for positive and negative CE operations (see Figures 5(a) and (b)). The comparison of the experimental results for positive CE operation with Equation (5) is seen in Figure 5(c); the agreement is good for some conditions, but not others. (R in Figure 5(c) is the quantity r_o defined above.)

For the gun with no outer electrode, there appears to be no difference between positive and negative operations [Butler *et al.* 1969]. In Figure 5(d) the comparison is shown of the experimental results for the shape and thickness using the analytical expression (Equation (5)), and a computer model result. A one-fluid, time-dependent model with similar assumptions for the equation of state was solved by the particle-in-cell method [Amsden 1966] and the solution corresponds closely to the experimental results.

The structure of the sheath has been studied with holographic interferometry, together with carefully time-correlated magnetic probe measurements and image-converter pictures [Butler *et al.* 1969]. A composite diagram, together with tracings of the interferometer fringes, is shown in Figure 6. The luminous sheath is the shock through which the density rises, with the current maximum just behind the luminous region. The current sheath is the plasma region.

While the above results show a sharply defined front to the sheath, together with a current distribution limited to a region behind the front, the evidence from magnetic probe measurements (Section 2.4) is considerably more complicated; it indicates a backward axial current flow through the region behind the sheath.

Estimates of the temperature and electron densities have also been made. For a 5 kV gun, at a pressure of 0.5 torr He, the intensity ratio of He II 4686 Å to He I 5876 Å lines gives 4.2 eV ± 15% [Lie *et al.* 1967] with an electron density of $\sim 2 \times 10^{17}$ cm^{-3} (Figure 5(b)). For higher voltage guns, an estimate can be made from resistance measurements of the sheath. Just before collapse at the end of the electrode, a value of about 30 μΩ for a sheath thickness of 1 cm has been obtained [Mather & Bottoms 1968]; this implies a temperature about 60 eV from the classical relation for resistivity [Spitzer 1956]. This value is consistent with computer results obtained from a two-fluid model of the plasma focus gun as described in Appendix A [Potter

1971].

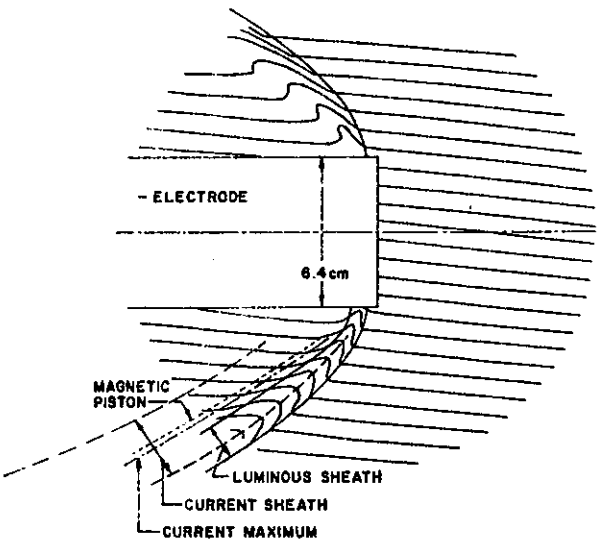

FIGURE 6(a)

Tracings of interference fringes with outlines of luminous sheath and current sheath taken from Fig. 6(b) under the same conditions. (Source: Butler et al. 1969)

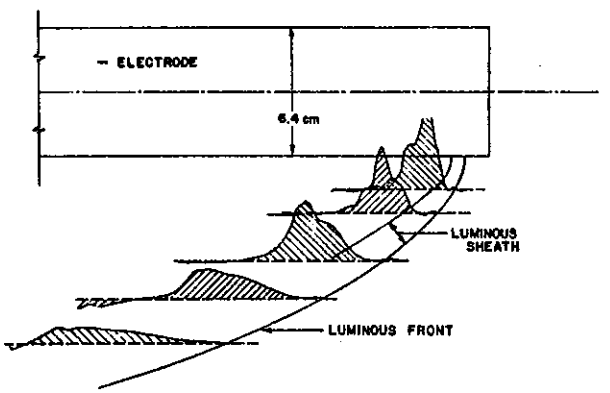

FIGURE 6(b)

Current density distribution at five radial positions under the following conditions: 0.43 torr filling pressure 240 kA current, 10^7 cm/sec front velocity. The current traces are not normalised. (Source: Butler et al. 1969)

The most serious limitation of the model for the sheath is the lack of a more realistic consideration of the ionisation levels that must exist near the outer electrode. As will be seen later (Section 2.3) about half the energy input to the gun can be required to ionise the gas. It is also known, from shock front studies in T-tubes (another form of magnetically-driven shock tube), that there exists a dense, cool layer of neutral gas along the wall of the tube [Maclean & Ramsden 1965]. Even the computer models show the formation of this layer but, owing to the lack of a neutral component and the imposed boundary condition at the wall, the effect of this layer is small in this model.

2.3 Electrical Measurements

Measurements of the circuit current and voltage at the electrodes can be used to determine how the initial capacitor energy partitions during the discharge.

A voltage divider at the breech of the gun and a Rogowski loop will give typical voltage and current traces as shown in Figure 7(a) and (b) [Mather & Bottoms 1968].

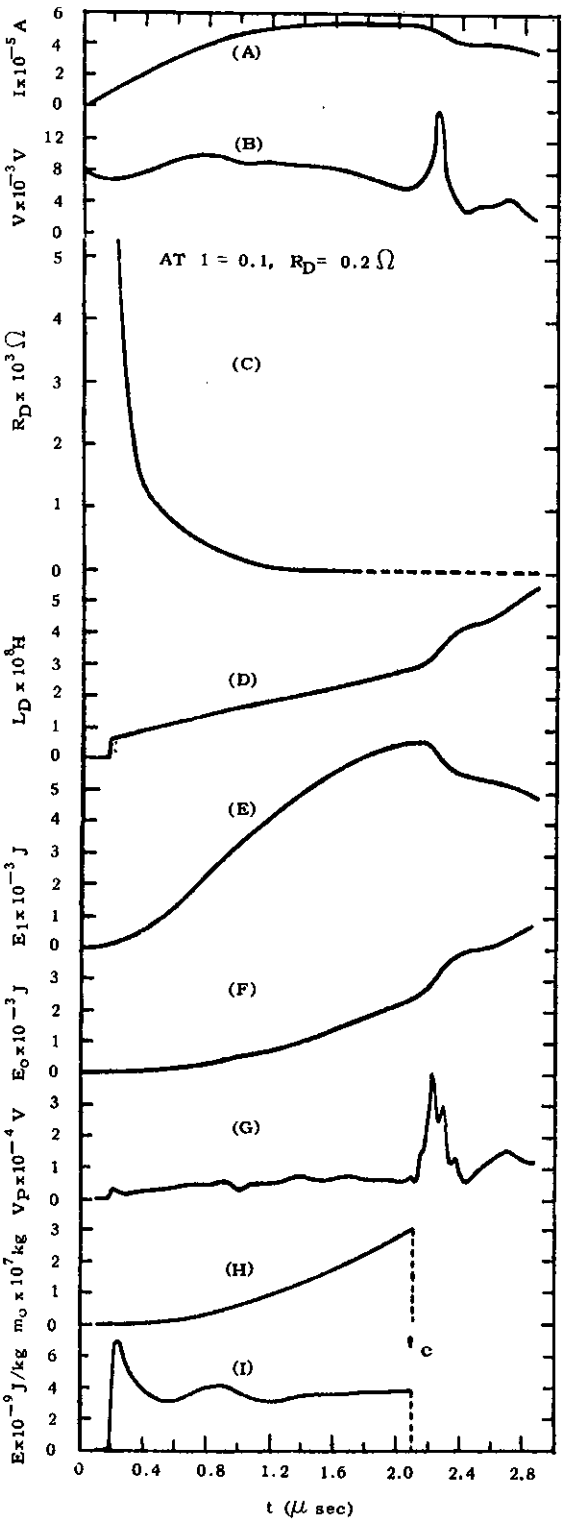

Typical data and results for a 17.3 kV discharge showing

(A) discharge current I(t),

(B) breech voltage V(t),

(C) plasma sheath resistance $R_D(t)$,

(D) plasma inductance $L_D(t)$,

(E) inductive magnetic energy $E_1(t)$,

(F) mechanical energy of sheath $E_o(t)$,

(G) pinch voltage $V_p(t)$,

(H) mass accumulated $m_o(t)$, and

(I) internal energy of plasma sheath per unit mass E(t).

Meter–kilogram–second units are used throughout. Curves (A)–(C) represent measured quantities.

FIGURE 7(a) – (i)

(Source: Mather & Bottoms (1968))

The curves given are for the following conditions:

Initial voltage V_o = 17.3 kV;

Total capacitance C = 90 μf;

External inductance L_e = 16 H;

External resistance R_e = 3.3×10^{-2} Ω;

Initial number density of filling gas = 4.9×10^{17} cm^{-3} of D_2;

Length of electrodes = 200 mm.

If the voltage drop V_R across the current sheath is measured with a coaxial electric probe connected between the inner and outer electrodes near the end of the accelerating section of the tube, the resistance of R_D of the sheath can be calculated (Figure 7(c)). The voltage at the breech of the gun is represented by the voltage V(t) across a-b in the equivalent circuit in

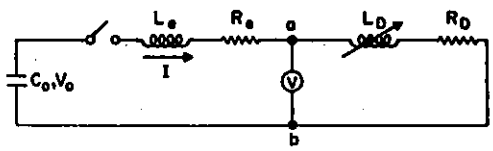

FIGURE 8
Equivalent electrical circuit of the discharge
(Source: Mather & Bottoms 1968)

Figure 8 and is given by the equation

$$V(t) = \frac{d}{dt}(L_D I) + IR_D \quad ,$$

where L_D is the inductance of the gun. The quantities R_e and L_e are the external resistance and inductance of the leads and capacitor bank. The following quantities can then be calculated:

(a) *Discharge inductance*

$$L_D(t) = \frac{\int_o^t (V - IR_D)\, dt}{I}$$

From this expression it is possible to obtain the velocity of the current sheath during its motion between the electrodes since, for a coaxial system

$$L_D \propto \text{length of the electrodes}$$

and hence

$$\frac{dL_D}{dt} \propto \text{velocity of the current sheath.}$$

(b) *Magnetic energy storage*

$$E_1(t) = \tfrac{1}{2}(L_e + L_D) I^2 \ .$$

(c) *Mechanical energy of the sheath*

$$E_o(t) = \tfrac{1}{2} \int_o^t \left(\frac{dL_D}{dt}\right) I^2 \, d\tau + \int_o^t R_D \, I^2 \, d\tau \quad ,$$

where $\dfrac{dL_D}{dt}$ is obtained from (a).

The mechanical energy, $E_o(t)$, consists of internal energy (*i.e.* heat energy and ionisation energy) and kinetic energy. Since image-converter photographs indicate the movement of gas along the front to the outer electrode, it is not possible to deduce either the mass contained in the sheath at any instance, or the kinetic energy, without using a detailed model. Any attempt to construct such a model would require the degree of ionisation to be known.

The spike on the voltage trace and the sudden reduction of the current are characteristics of a good focus. If breakdown has occurred across the insulator during the acceleration stage, then both the voltage and current traces are smooth [Peacock *et al.* 1968]. This is because the breakdown acts as a short and isolates events inside the gun from those outside it. The voltage spike begins at the start of the collapse, since the inductance rises sharply at that time.

The resistance, R_D, of the discharge is obtained from the measurement V_R as $R_D = V_R/I$. In Figure 7(c) the typical value of R_D after about 1 μsec is $\sim 30 \times 10^{-6}$ Ω. If a sheath thickness of 1 cm is assumed, Spitzer's relation for the resistivity η, is given by

$$\eta = 6.5 \times 10^3 \, Z T^{-3/2} \, \ell n \, \Lambda \ \Omega\text{-cm}$$

where Z is the charge number of the ion, T is the temperature in kelvin, and $\ell n \, \Lambda$ is the Debye cut-off factor (the usual factor of 10 is used here) which gives a temperature around 60 eV.

Up to the collapse time t_c, about 2.7 kJ of mechanical energy has been supplied to the sheath (Figure 7(f)). To ionise totally the gas in the tube swept up by the sheath to time t_c requires about 1.2 KJ and hence 1.5 KJ remains for the kinetic energy and the heating of the front.

The discharge inductance is seen to rise linearly, showing that the sheath velocity becomes constant. For a cylindrical geometry,

$$\frac{dL_D}{dt} = 0.002 \, \ell n \, (r_2/r_o) \, v_s \ \mu\Omega, \quad \text{which with } r_2/r_o = 2 \text{ and } dL_D/dt \simeq 10.6 \ m\Omega \text{ (from Figure 7(f))}, \text{ gives } v_s \sim 7.5 \text{ cm } \mu\text{sec}^{-1}.$$

The 'snowplough' velocity, v_s, for constant voltage can be written

$$v_s = \frac{6.95\ V_3^{\frac{1}{2}}}{(A\ p_\tau)^{\frac{1}{4}}} \quad ,$$

where V_3 is the voltage in kilovolts, A is the atomic number of the molecule of the gas filling and p_τ is the filling pressure in torr. If $V_3 = 8$ (Figure 7(b)), A = 4, and $p_\tau = 14.8$, then $v_s \sim 7.1$ cm μsec^{-1} which is in good agreement with the velocity derived from $\frac{dL_D}{dt}$.

It can be seen from Figure 7(e) that just after the collapse time the stored magnetic energy, E_1, decreases. This energy appears in the mechanical energy of the collapsing plasma.

2.4 Magnetic Probe Measurements

A magnetic probe measures the magnetic field distribution and hence the current distribution between the electrodes. Probe measurements in a coaxial system [Mather 1965] give somewhat more complicated distributions than a system having the centre electrode only.

From a typical set of results given in Figure 9(a) and (b) (the collapse time, t_c, is greater than 2.4 μsec), it can be seen that the B_θ field does not fall off as the inverse of the radius r, even in the case where the front has passed the measurement point and after the collapse over the end, *e.g.* at t = 3.3 μsec (Figure 9(a) at z = 20 cm). This implies that some of the current is returning through the volume behind the front rather than the outer electrode.

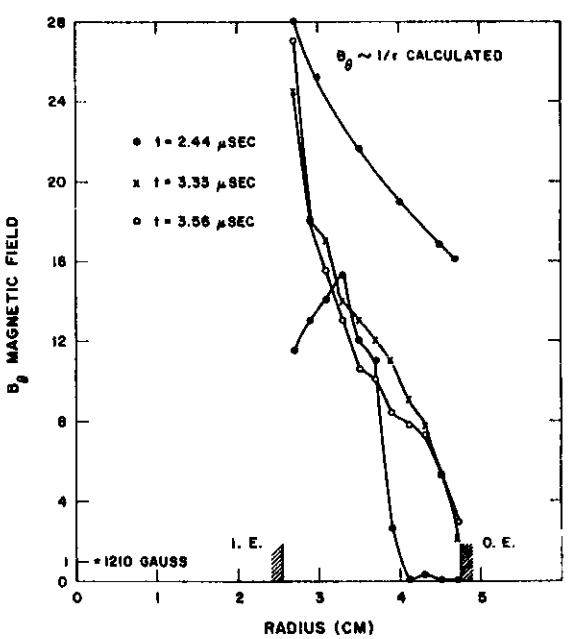

FIGURE 9(a)
B_θ vs r for several times. z = 20 cm
(Source: Mather 1965)

Further measurements with a double probe, taken simultaneously at two axial positions (18.7 and 20 cm from the breech), allow the two components of the current density to be computed from

$$j_z \sim 1/r\ \frac{\Delta(rB_\theta)}{\Delta r}$$

and $$j_r \sim \frac{\Delta B_\theta}{\Delta z}$$

Typical results are shown in Figure 9(b). Positive values of j_z represent flow back to the breech and positive values of j_r represent flows from the centre to the outer electrode.

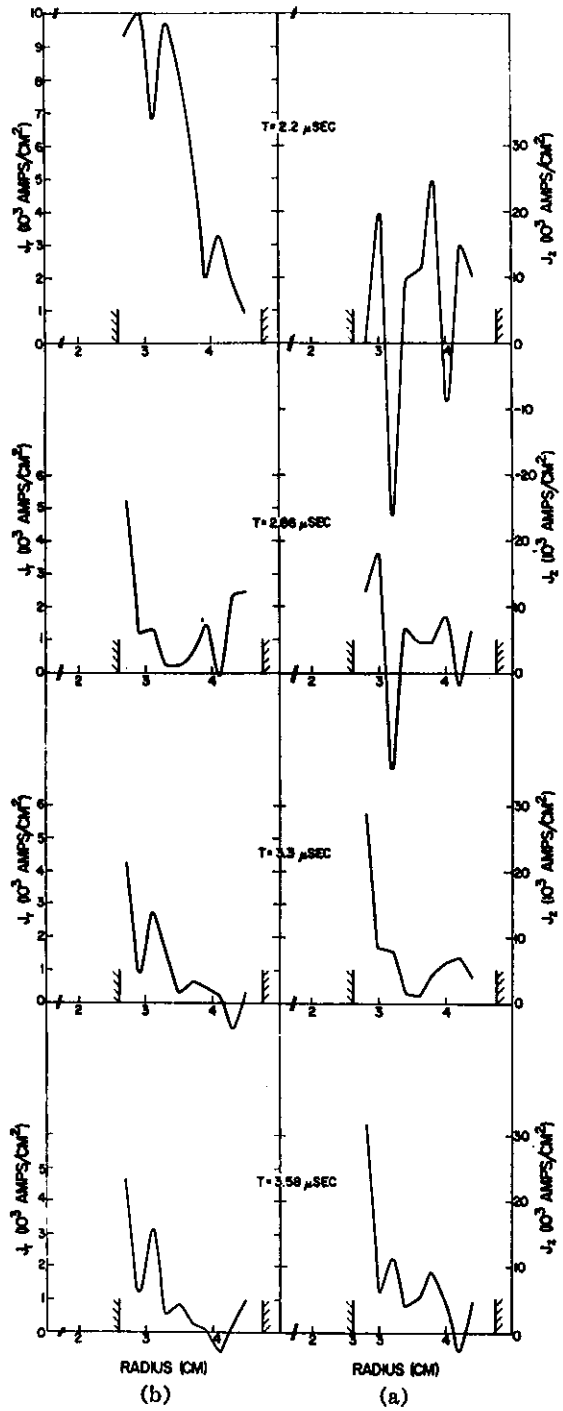

FIGURE 9(b)

Current densities j_z curve "a," and j_r curve "b," as function of radius and time at $z \sim 19$ cm.
(Source: Mather 1965)

After the front collapses over the end of the electrode, most of the current is in the z-direction (*i.e.* axially), and is maximum near the centre electrode. A graphical integration of the current through the annulus at $z \sim 19$ cm gives that approximately 3×10^5 A flows through a plasma, *i.e.* approximately half the total current. Quite a complicated pattern occurs when the front is at the measurement plane ($t \sim 2.2$ μsec) with both positive and negative j_z values.

These results cannot be explained even by the two-fluid computer models; they are probably due to structures in the aximuthal direction, *e.g.* vortices.

Probe measurements of the fields at the focus have not been possible so far, owing to the small size of the focus (of the order of millimetres) and the high temperatures and currents which destroy the probe.

3. COLLAPSE STAGE

Framing pictures of the collapse stage indicate the non-cylindrical nature of the collapse - the gas near the electrode reaches the axis first with progressively later times for the gas further from the electrode. After the pinch, it is also possible to observe the breakup caused by instabilities in the pinched plasma. Detailed observations are not yet possible owing to the difficulties in interpreting visible light pictures.

3.1 Shape and Velocity of Shock

Radial velocities of the collapsing front can be measured from streak photographs of the region in front of the electrode, looking at right angles to the axis, with the slit also perpendicular to the axis. For operation at 3.5 torr D_2 and 18 kV, radial velocities of 10 to 40 cm μsec^{-1} have been recorded [Toepfer, Smith & Beckner 1971]. A diagram of a typical streak photograph taken 1 cm from the end of the electrode is shown in Figure 10(a). Four main features are easily observed:

- the initial collapse;
- a bounce;
- a dark period; and
- the final bright jet on the axis.

More quantitative evidence for the non-cylindrical nature of the collapse is given in Figure 10(b), where the time that the luminous front reaches the axis is plotted against the axial position. Over an axial distance of about 2 cm (the approximate total length of the neutron-producing part of the focus) the time lag is 50 to 60 nsec. This time lag is important in one of the acceleration models for neutron production; it is discussed in Section 6.5 [Bernstein 1970]. The acceleration mechanism operates for 10 to 20 nsec after the front arrives at the axis and over a distance of a few millimetres. Hence the time lag permits the possibility of tandem acceleration as the particle enters successive acceleration regions.

The radius of the luminous front as a function of time at various axial positions can be seen in Figure 10(c). This also indicates the non-cylindrical nature of the front and gives the radial velocity at each axial position. The radial velocity is seen to increase with distance from the electrode; this

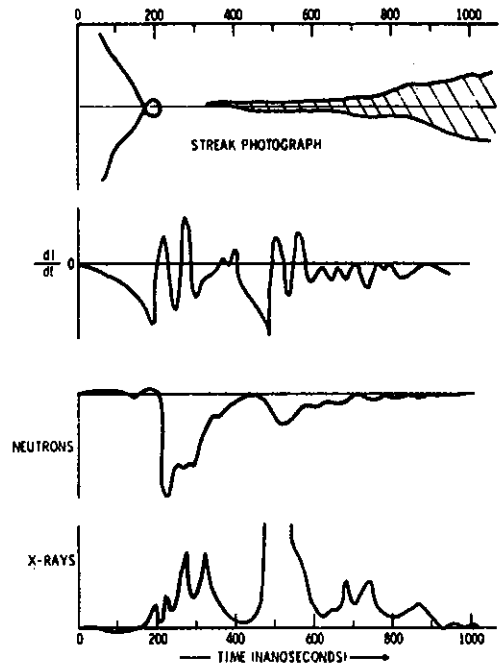

(a) Luminous front, dI/dt, neutron and X-ray signal for a typical shot referred to a common time scale. (Source: Toepfer et al. (1971)

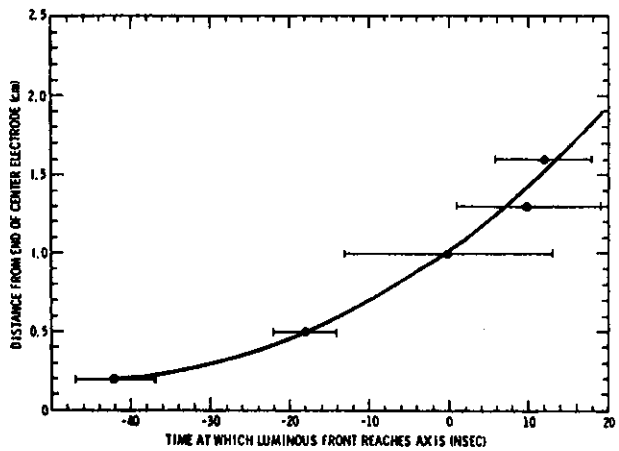

(b) Axial distance z from the end of the centre electrode vs time at which the luminous front reaches the axis at that axial position. t = 0 corresponds to the start of the first X-ray pulse. (Source: Toepfer et al. 1971)

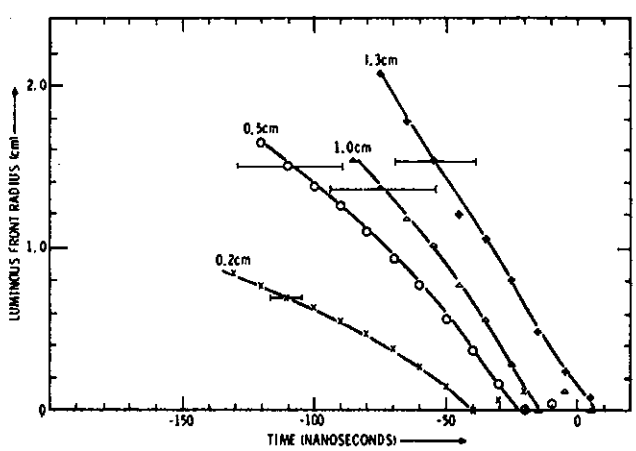

(c) Luminous front radius vs time at four different axial positions. t = 0 corresponds to the start of the first X-ray pulse. (Source: Toepfer et al. 1971)

FIGURE 10(a) – (c)

result is at variance with shadowgraph measurements of the velocity. A typical measurement is seen in Figure 11(a) which shows that the velocity decreases with increase of axial distance from the centre electrode [Peacock, Hobby & Morgan 1971]. (With this technique, axial velocities can also be measured and are seen to be relatively small compared to the radial velocities.)

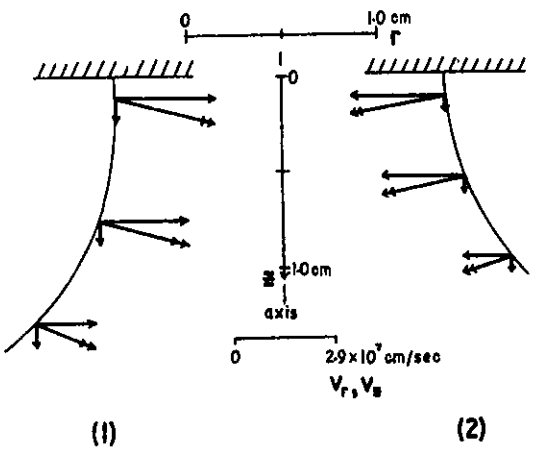

FIGURE 11(a)

Variation of radial and axial velocity of the imploding sheath with distance from electrode surface;
(1) V = 28.3 kV
(2) V = 24.3 kV; P_o = 2.5 torr (D_2 + 4% Ar).
(Source: Peacock et al. 1971)

From the time correlation of various other measurements with streak photographs, the following points can be made:

(a) The initial sudden fall in dI/dt is indeed correlated with the collapse stage.

(b) The main neutron pulse occurs at the fading of the streak (at ~ 200 nsec in Figure 10(a)). This fading is also a feature of the main neutron pulse when a longitudinal magnetic field is applied at the end of the electrode. In this case, the fading is postponed and occurs some 50 nsec later, but this applies also to the neutron pulse [Bernstein & Hai 1971]. The sequence of events just before fading is more easily seen when a magnetic field is applied. After the visible plasma starts to repinch, the boundary stops contracting and expands slowly outwards, becoming indistinct. Without a magnetic field, the last stages are often not clear enough to be visible. The fading can be interpreted as a reduction in the

density of the plasma owing to the magnetic field diffusing through the plasma. Because of the non-cylindrical geometry of the pinch, the luminosity does not fade simultaneously at all points along the axis.

3.2 Density of Pinch

Before discussing the resistivity required for the diffusion of the magnetic field in such a short time, the data of Peacock, Hobby & Morgan [1971], derived from shadowgraph and interferometric measurements are considered. Shadowgrams with 1 nsec exposures give structural detail of the collapsing front, together with the front velocity. The boundary in which the refractive index changes is quite sharp - $\delta(dn_e/dr) < 1$ mm where n_e is the electron density. The boundary becomes fluted owing to the Rayleigh-Taylor instability, but does not disrupt before the maximum compression. The breakup of the pinch proceeds *via* the m = 0, and occasionally the m = 1, instability. Over the 38 mm x 27 mm field of observation (z x 2r) of the total duration of the non-cylindrical implosion, the formation of the dense pinch and its breakup is less than 100 nsec. After this, there are no features of electron density greater than 8 x 10^{18} cm^{-3}. In fact, during the late stages of the breakup, an interferogram gives a density distribution

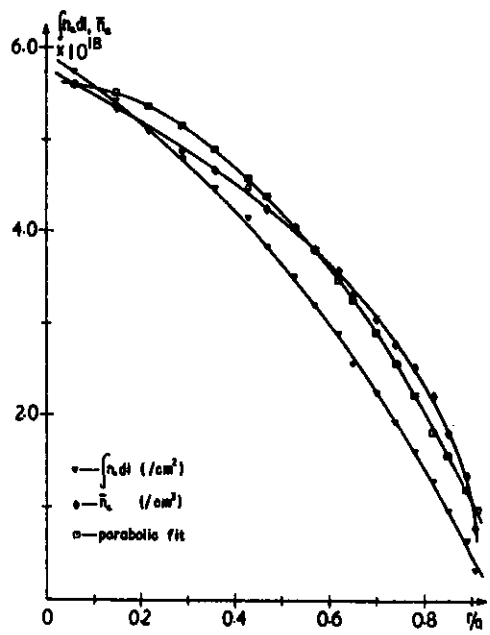

FIGURE 11(b)

Variation of $\int_o^\ell n_e \, d\ell$ and $\bar{n}_e(r/a)$.

Analysis has been made along section AA.
A parabolic function $\bar{n}_{em}(1-(r/a)^2)$ is also shown.
V = 30 kV; p_o = 2.5 torr (D_2 + 4% Ar).
(Source: Peacock et al. 1971)

as in Figure 11(b). The mean density $\bar{n}_e$ as a function of radius is obtained from $\bar{n}_e = \int_o^{\ell} n_e d\ell/(\text{length of the chord})$ and can be written in the form

$$\bar{n}_e = \bar{n}_{em} [1 - (r/a)^2] \quad ,$$

where $\bar{n}_{em}$ is the maximum value of $\bar{n}_e$. It is proposed that the actual density $\bar{n}_e$ is also parabolic, and hence an estimate can be obtained of the peak density n_{em} on the axis. A value of 8×10^{18} cm^{-3} is obtained for the case shown in Figure 11(b). In other cases, values as high as 4×10^{19} cm^{-3} were obtained closer to the anode. The section AA referred to in the caption of Figure 11(b) is perpendicular to the axis about 2 cm from the electrode.

For the relaxation of the sharp density front to a parabolic distribution, there must be a rapid diffusion of the magnetic field to the axis. The $1/e$ - folding time τ for the diffusion of the magnetic field through the sheath [Glasstone & Lovberg 1960] can be taken as

$$\tau \sim \frac{200 r \delta}{\eta} \text{ nsec} \quad ,$$

where r is the plasma radius in m, δ is the sheath thickness in m and η is the resistivity in Ωm. The classical expression for the resistivity is

$$\eta \sim 5 \times 10^{-4} T_e^{-3/2} \ \Omega m \quad ,$$

where T_e is the electron temperature in eV.

For $\delta \sim 0.05$ cm, $r \sim 0.1$ cm and $T_e \sim 30$ eV, the value of τ is 30 nsec. Hence for temperatures less than 30 eV significant diffusion could occur, but not for temperatures usual at the pinch stage (several hundred eV), and so an anomalous resistivity appears to exist. One suggestion [Bernstein & Hai 1971] is that as soon as a small amount of current (and hence magnetic field) has diffused to the axis, there is a great reduction of the mobility of the electrons, *i.e.* the resistivity rises. Another suggestion is that the instability which disrupts the ordered pinch causes a turbulent region to be formed which would have a high resistivity.

If reference is made to the two-fluid computer model, it is found that a rapid (30 nsec) diffusion of the current to the axis occurs, at least in a region near the electrode, owing to the presence of low electron temperatures. The electron temperature is kept low by heat conduction to the electrode. The focus then appears to be formed by axial flow of this cold magnetised plasma away from the electrode. It is rapidly heated to more than 1 keV by Joule heating for the electrons and viscous heating for the ions. The ions are raised to several hundred eV initially by adiabatic heating during the initial compression. Later, it will be shown that the ions and electrons

can have different temperatures owing to their long equipartition times.

The existence of a very fine structure in the pinch region is indicated by shadowgram and Schlieren photography [Peacock, Hobby & Morgan 1971]. Singularities appear in the density gradient with dimensions less than 100 μm. This fine structure occurs on the axis within an envelope of 1 mm diameter. The same region is also a source of very intense line emission in the X-ray region. Deliberate mismatching of the source and crystal of the spectrometer restricts the bandwidth very severely for a very narrow source. This allows such emitting regions - in this case around 100 μm - to be observed in the structure of the line (Ar XVII at 3.949 Å in this case). These regions appear to be mobile filaments.

The lower limit of the density in the filaments can be derived as 7.5×10^{19} cm^{-3}. The only scale length of the plasma small enough is the collisionless skin depth c/w_{pe} (where c is the light speed and w_{pe} is the electron plasma frequency). A possible interpretation of the high density lines is the damping of a collisionless shock arriving on the axis of symmetry.

3.3 Temperature of Pinch

Thomson and Rayleigh scattering techniques can be applied to the measurement of the ion and electron temperatures and the electron density. These methods have many desirable features, especially when used with a pulsed laser system. In this case, high temporal and spatial resolution is possible with small perturbation of the plasma. Practical problems have so far limited the results obtained.

The scattered spectrum for Thomson scattering depends on two parameters β and α, defined by

$$\beta = \left(\frac{T_e}{T_i} \frac{\alpha^2}{1+\alpha^2} \right)^{\frac{1}{2}}$$

and

$$\alpha = \frac{\lambda_o}{4\pi \lambda_D \sin(\theta/2)}$$

where T_e and T_i are the electron and ion temperatures;
λ_o is the laser light wavelength;
λ_D is the Debye length in the plasma; and
θ is the angle of observation relative to the incident beam
[Salpeter 1960].

The parameters β and α for a measured profile are obtained by fitting it to

theoretical profiles.

Since Rayleigh scattering depends on the electron density, this parameter can be computed from reasonable assumptions about the scattering volume.

Reported results [Baconnet *et al.* 1969] for measurements 10 nsec before the start of the neutron emission are

$$T_i = 370 \pm 50 \text{ eV}, \quad \text{and}$$
$$\beta \sim 0.7.$$

This gives a range of $180 < T_e < 300$ eV for the electron temperature and, from Rayleigh scattering, $n_e > 4 \times 10^{18}$ cm^{-3}. There is also a drift velocity of the plasma away from the electrode of 17 cm μsec^{-1}.

For later times and higher temperatures, the angle θ must be decreased from the 90° used in the example to about 7°, otherwise α will become less than one and make the profile too broad to interpret. From the expression for α, it can be seen that this increases α by a factor of ten.

At 40 nsec after the start of the neutron emission, preliminary results [Bernard *et al.* 1971(a)] indicate that for the assumption $\beta = 1$, $T_i = T_e = 580$ eV, or if $\beta = 0.5$, $T_i = 4T_e = 1100$ eV. At both times, it is seen that $T_i > T_e$ as shown by the computer model.

3.4 Shock Heating

The collapsing front can be considered in more detail to see the effects of shock heating but, since the final ion and electron temperatures appear to depend on a complex interplay of the dissipation coefficients, this will only be an indication of the phenomenon. The experimental data is obtained from streak photographs of the type shown in Figure 10. Figure 12(a) [Toepfer, Smith & Beckner 1971] gives a typical time history of the collapse at 5 mm from the end of the electrode, up to the time of fading of the plasma light. The stages of the collapse - the incident shock, the reflected shock (or bounce) and the final magnetic compression - are indicated. Figure 12(b) [Bernstein & Hai 1971] shows the variation of the luminous plasma radius as a function of time with the type of centre electrode end and the strength of the longitudinal magnetic field for various distances from the

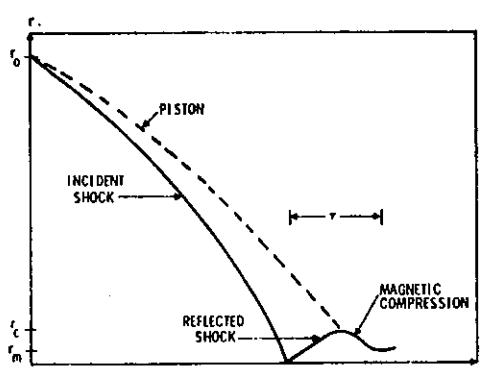

FIGURE 12(a)

Radial collapse of ionising shock, followed by a magnetic piston. The average time interval τ for the final compression of the shock heated plasma was about 12 nsec. (Source: Toepfer et al. 1971)

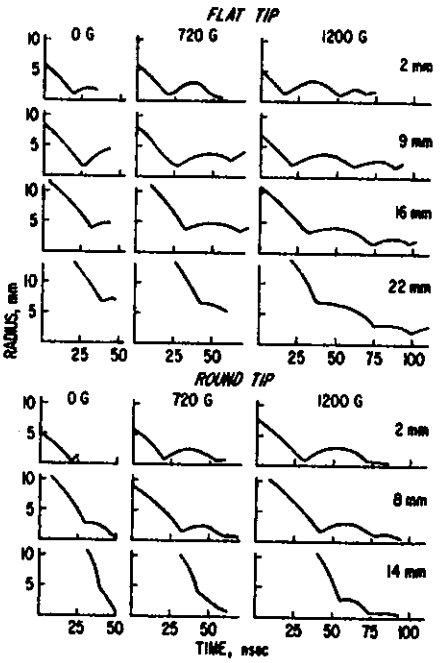

FIGURE 12(b)

Time dependence of luminous plasma radius as a function of applied field and height above anode at 18 kV. Pressures were 5 and 8 torr for flat and round anode tips, respectively. (Source: Bernstein & Hai 1971)

electrode.

The gas is swept up by the shock, heated and ionised, and then driven by the magnetic piston. Since the collapse is non-simultaneous along the axis occurring earliest near the electrode, there will be a pressure gradient along the axis. This will cause the gas to be ejected axially from the pinching region. This conclusion is supported by calculating the pressure balance during the pinch phase.

At 1200 gauss initial field, the average visible radius was 2 mm at the first bounce, giving an axial field at this radius of 450 kilogauss compared with 650 kilogauss for the azimuthal field. The difference can be attributed to the plasma pressure and can be calculated from the bounce frequency ω for a pinch with an entrapped field. The frequency ω is given by

$$\omega^2 = \frac{B^2}{4\pi\rho_s r}$$

where B is the magnetic field at equilibrium,

r is the radius at equilibrium, and

ρ_s is the areal density of the oscillating slab.

Values for ρ_s of 7.5×10^{-6} g cm^{-2} and 2.8×10^{-6} g cm^{-2} for bounce periods of 42 nsec and 26 nsec respectively are found. These values represent 23 per cent and 9 per cent of the gas encountered by the shock for 5 torr initial pressure, and so gas is ejected axially from the compression region by the pressure gradient.

Since, with a pressure of 3.5 torr D_2 at 300 K as the initial state, a velocity of 43 cm μsec^{-1} corresponds to a Mach number M of 460, the density ρ_2 and temperature T_2 behind the shock can be calculated from strong shock theory to be 1.76×10^{18} cm^{-3} and 360 eV respectively. Since the ion-ion energy equipartition time is less than 10 nsec under these conditions, a shock will form in front of the current sheath, even at the greatest collapse velocities.

If the shock reflects at the axis, the density n_3 and temperature T_3 behind the shock can be calculated to be 4.4×10^{18} cm^{-3} and 800 eV respectively. The corresponding equipartition times are then given by

t_{ii} (ion-ion) $\sim$ 9 nsec,
t_{ee} (electron-electron) $\sim$ 0.2 nsec, and
t_{ie} (ion-electron) $\sim$ 50 nsec.

It is apparent that both the ions and the electrons will thermalise, but the electrons will not have enough time to thermalise with the ions before the reflected shock meets the magnetic piston. Since the electrons have negligible directed energy, they will be at a lower temperature than the ions, *i.e.* near T_2.

After the bounce, there will be a compression by the magnetic piston. This will cause a further rise in temperature, but the amount will depend on the amount of matter lost axially from the compression region. Viscous heating of the ions due to the axial flow is shown by the computer model to be an important factor (Appendix A), but realistic estimates of the amount of heating are impossible. Even the computer results are qualitative since the mesh size introduces errors at the small scale lengths involved.

The ordered pinch formation breaks up owing to the growth of the m = 0 (or occasionally the m = 1) instability [Peacock, Hobby & Morgan 1971]. This corresponds to the loss of the sharp, visible boundary on the streak photographs. The computer simulation shows that the long life of the pinch under these conditions (theory normally indicates a life of less than 10 nsec) is due to the stabilising action of the ion viscosity. This is also consistent with the shadowgraph results which show that the time for the collapse through the last 20 mm and the complete breakup of the pinch is no more than 100 nsec.

4. X-RAY EMISSION

4.1 Phenomenology

The X-ray emission from the plasma focus consists of a series of bursts starting near the dI/dt minimum. There are typically two or three bursts of about 100 to 300 nsec duration (Figure 10(a)).

A pinhole camera can be used to image the X-rays from the focus on to photographic film to give a time-integrated picture of the emission. Visible light is excluded by a thin foil of aluminium or beryllium across the pinhole. The main features observed are:

(a) The X-ray emission occurs at the electrode and from a column 10 to

20 mm long and 1 to 2 mm diameter, with a larger low intensity region around this [Mather 1966, Bernstein, Meskan & Van Paassen 1969, Gratreau *et al.* 1971].

Further investigation of the light column reveals fine structuring which can be used to classify the foci into four groups in descending order of neutron yield [Agofonov *et al.* 1970].

(i) A fairly straight band - sometimes with additional illumination of an irregular shape and shorter length located further from the anode - lies not quite on the axis. This is accompanied by the largest neutron yield.

(ii) Images in the form of two fine bands can be observed; stereoscopic pair analysis shows that these are not parts of a tube. The bands give average neutron yields.

(iii) Images similar to those in (i) and (ii) but with a chain of beads superimposed.

(iv) Complex images with minimal neutron yield.

(b) The column appears to be turbulent, but the application of a longitudinal magnetic field of several hundred gauss at the end of the centre electrode increases the column stability (though with a reduction of neutron and X-ray output). The X-ray output at the electrode face is also decreased [Mather *et al.* 1969].

(c) There is a shot to shot variation in the position of the filamentary region of up to 10 mm [Gratreau *et al.* 1971]. This makes spatial distribution studies, which require a large number of shots to scan the focus, difficult to interpret.

(d) The radiation from the column is mostly less than 5 keV [Mather *et al.* 1969] as observed by the differences in blackening of film when air replaces the helium in the pinhole camera. If the film is replaced by a plastic scintillator and observed with an image-converter camera, short exposures are possible to obtain time-resolved pictures [Bernstein & Hai 1970(a)]; this determines that soft X-rays less than 4 keV originate in the plasma column and start with the collapse of the current front. The X-rays in the 4-20 keV range are delayed by 10 to 40 nsec and initially originate from the anode, but some 100 to 500 nsec later they are emitted also from the plasma column. This late emission is attributed to a cloud of heavy metal ions leaving the anode and drifting along the axis. The time delay becomes larger as the observation point

moves further from the anode and is found to be consistent with a velocity of around 10 cm μsec^{-1} [Bernstein, Lee & Hai 1971].

The spatial resolution was only about 1 to 2 mm because a large pinhole (2 mm) was required to obtain enough intensity; for better spatial resolution a smaller pinhole is required. The image intensity can be boosted by the use of a channel electron multiplier plate [Gratreau *et al.* 1971] in front of the scintillator. The 2 mm diameter of the plasma was confirmed with a 200 μm pinhole; also it was confirmed that the second strong burst of X-rays comes from a diffuse cloud having no discernible structure. This is further evidence that the second burst emanates from a moving cloud of ions.

The energy resolution described above is obtained by covering the scintillator with absorber foils so that, by a suitable choice of thicknesses of the foils, a difference in the X-ray transmission occurs only between the K-edges of the foils. For example, magnesium, aluminium, chlorine (in the form of Saran) and titanium cover the energy range 1.31 keV to 4.98 keV [Bernstein 1972].

If the scintillator is followed by a photomultiplier, the X-ray output as a function of time can be obtained. Earlier in this section it was shown that different energy bands and spatial positions have different time histories. The neutron output [Bernstein, Lee & Hai 1971] is correlated in time (*i.e.* starting time and peaks) with the X-ray output in the 30 to 60 keV range, and also correlated with the fading of the visible light.

There are some measurements made at isolated energies with an X-ray spectrometer [Patou 1970] which correlates with the dI/dt trace; in this case, the field of observation excludes the end of the centre electrode (Figure 13(a) to (c)). The emission in the copper Kα line increases dramatically around 500 nsec after t_m (the first minimum of dI/dt), although a very small amount of emission is present from t_m (Figure 13(b)). The traces at 12.4 keV and 24.8 keV start just after t_m, with the latter about 10 nsec after the former (Figure 13(c)). If the emission at 8.85 keV is observed with a more sensitive spectrometer setting than in Figure 13(b), the emission starts just before t_m (Figure 13(a)).

Hence there is radiation up to at least 25 keV from the plasma column within 15 nsec of t_m, although it is too weak above 4 keV to be observed by the experimental arrangement of Bernstein, Lee & Hai [1971]. They observed the considerable rise in the 4 to 25 keV radiation some 500 nsec later, in agreement with Figure 13(b) which shows enhancement in the output of the copper Kα (8.0 keV) line and at 8.85 keV.

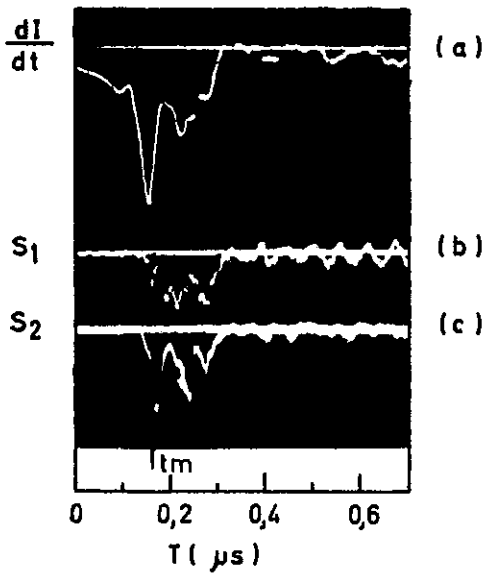

(a) Signals from spectrometers S_1 and S_2 observing the energy emitted at $\lambda = 1.4$ Å
(Source: Patou 1970)

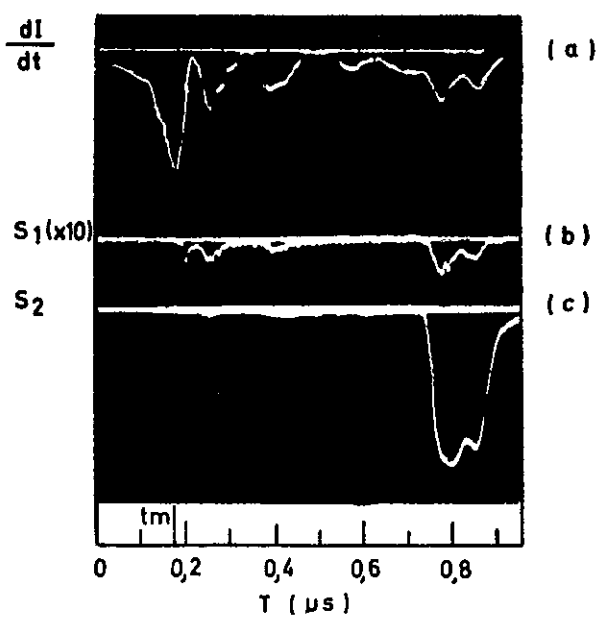

(b) Spectrometer S_2 shows the $K\alpha$ ray for copper ($\lambda_o = 1.55$ Å). S_1 observes the energy emitted at $\lambda = 1.4$ Å.
(Source: Patou 1970)

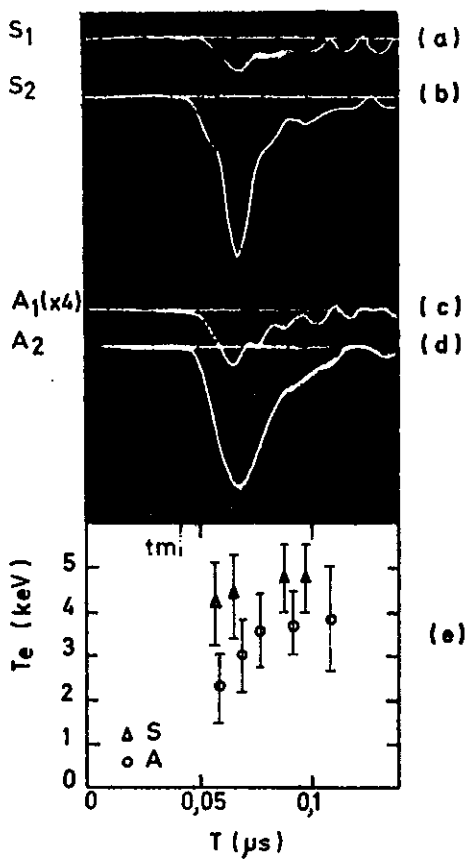

(c) Comparison of the measurement of the electron temperature by the absorber method (A) and by spectrometry (B).
(Source: Patou 1970)

FIGURE 13 (a – c)

Other measurements in the 5 to 29 keV range indicate that the shape of the continuum spectrum remains constant with time and varies only in intensity [Bernstein, Meskan & Van Paassen 1969; Van Paassen, Vandre & White 1970]. The X-rays observed originate essentially from the anode, since the plasma emission is much weaker until the copper cloud is emitted from the anode giving à line spectrum and an enhanced continuum.

4.2 X-ray Spectrum

The X-ray spectrum has been measured in the range 1 to 350 keV. Time-resolved data are available only for energies less than 30 keV, since nuclear emulsions must be used above this energy. The low energy end (1 to 30 keV) is measured with scintillators followed by photomultipliers having various filter combinations in front of the scintillator. By a suitable choice of materials for the filters, bands of energy can be defined between the K-edges of the foils. The thickness of each foil is so chosen that the transmission is approximately the same except between the K-edges. (Pairs of filters chosen in this way are known as Ross filters. If the spectrum is known to be thermal, the measurement of intensity behind each foil of the pair is enough to give the electron temperature of the source.) Alternatively, it is possible to use K-edge diodes preceded by filters. This system is similar except that the high transmission energy band is defined between the K-edge of the cathode and that of the filter.

The spectrum from 1.5 to 30 keV has been measured with the following K-edge diode material - filter combinations:

Al + no filter	Fe + Zn
Ca + Ti	Cu + Zr
Ti + Fe	Zr + Mo
Cr + Ni	Ag + Sn

with the filter thickness, in each case, of one mean free path for the energy at the filter K-absorption edge [Mather *et al.* 1971]. This provides fairly fine resolution over the 1.6 to 8 keV band and coarser resolution over the other bands. The charge Q measured by each detector is given by

$$Q = \int_{E1}^{E2} K(E)\, R(E)\, \frac{dP(E)}{dE}\, dE ,$$

where K(E) is the transmission function for the filters, windows, *etc.*;

R(E) is the response function of the K-edge diode; and

dP(E)/dE is the differential power spectrum per unit energy interval.

The spectrum was derived with a computer code by an iteration technique

to match the measured values of Q and is shown in Figure 14. The low energy region up to 7 keV is exponential and confirms the existence of a Maxwellian electron population. The temperature for the example shown in Figure 14 is 3 keV, with a range of 2 to 7 keV for other shots. The copper Kα and the tungsten Lα, Lβ, and Lγ lines are also seen.

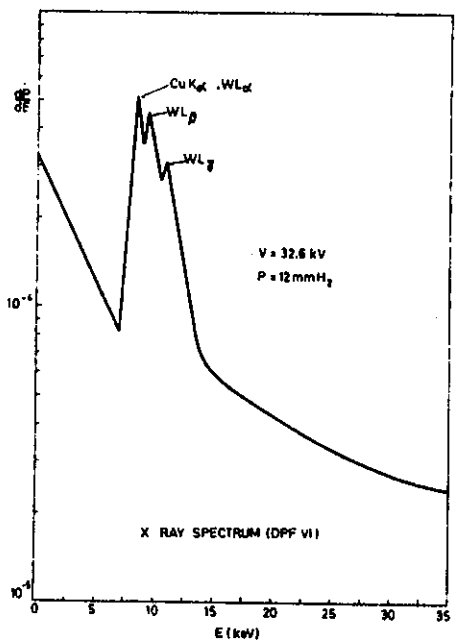

FIGURE 14
A typical X–ray spectral distribution, dP(E)/dE versus E
(Source: Mather et al. 1971)

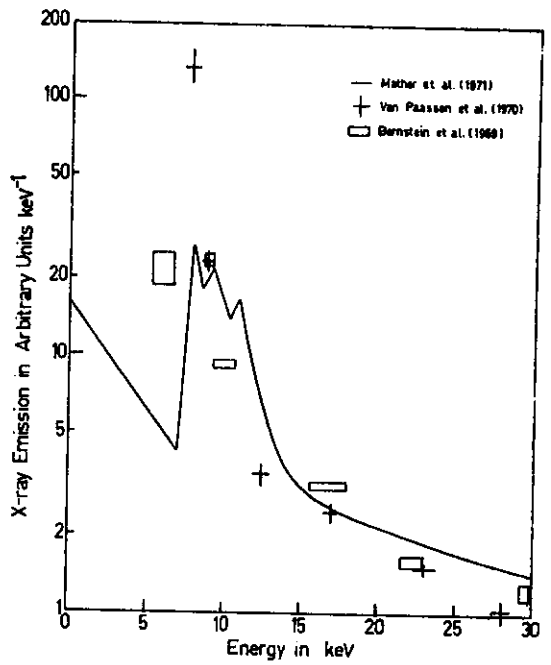

FIGURE 15
Earlier measurements of the X–ray spectrum superimposed on the results of Mather et al. (1971)

In Figure 15, earlier measurements of the spectrum are superimposed on the results of Mather *et al.* [1971]. The graph scales have been normalised and are intended to compare the shapes only. The correspondence is quite good. Van Paassen, Vandre & White [1970] made absolute measurements of the X-ray output in the 7 to 30 keV range with Ross filters and in the range 50 to 350 keV with nuclear emulsions. This allowed the comparison of the two parts of the spectrum (Figure 16(a)). The high energy region of the spectrum can be represented by

$$\left(E \frac{dN}{dE}\right) \sim E^{-2 \cdot 5}$$

where N is the X-ray photon flux per square centimetre. The lower energy X-rays are not correlated with the neutron yield, whereas the high energy intensity depends on the neutron yield; hence it is not surprising that the two regions of the spectrum do not fit smoothly (Figure 16(a)). The spectral shape appears to be machine-independent and only the total X-ray output seems to vary with the machine.

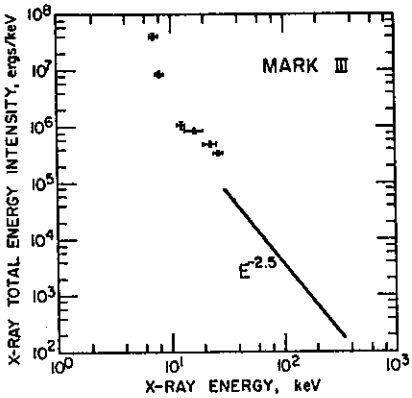

FIGURE 16(a)

The experimental X-ray total energy intensity (dN/dE) on axis from Mark III. The Ross filter data are given by the plotted points with error bars. The best fit X-ray spectrum to the emulsion data is given by the solid line.
(Source: Van Paassen et al. 1970)

The high energy region of the spectrum can be produced by the thick target bremsstrahlung from an electron distribution as given by

$$\left(\frac{dN_1}{dE}\ E\right)_{brems} = a\ E^{-3.3}\ ,$$

where N_1 is the electron flux striking the anode (the main X-rays in this

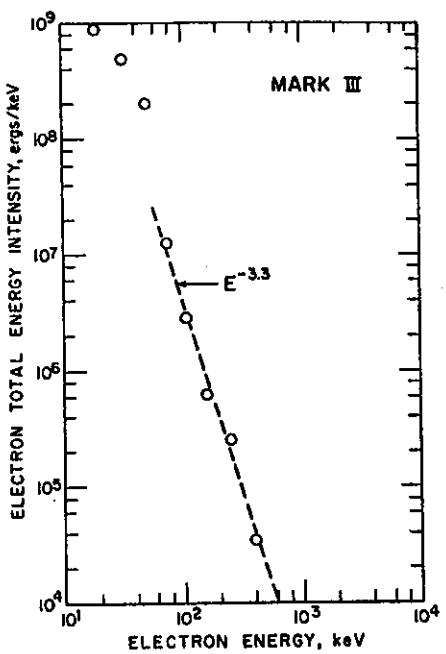

FIGURE 16(b)

The calculated electron energy spectrum required to produce the X-ray energy spectrum (see ref.) by bremsstrahlung. The calculated points are plotted as circles. The dashed line is a power fit to the points. (Source: Van Paassen et al. 1970)

measurement come from the anode since the viewing direction is along the axis). Figure 16(b) shows the points calculated to give the X-ray spectrum compared with a power law. The spectra showed no significant dependence on the filling gas.

The peak in the spectrum at 8 to 9 keV, relates to copper and tungsten fluorescence lines. It appears that the bulk of the atoms producing this emission comes from erosion of the end of the electrode. If the material at the end of the electrode is changed, the fluorescence lines are changed also [Mather *et al.* 1971]. The lines of silver were found specifically when a silver insert was used [Bernstein, Meskan & Van Paassen 1969].

Besides these detailed spectral measurements, there are many measurements of transmissions through foils for calculating the temperature of the electrodes. From the above spectra, it seems that only those measurements in the 1 to 5 keV band will give useful results, since the high energy emissions are probably from non-Maxwellian distributions. Furthermore, it seems doubtful whether the temperature thus obtained will have much bearing on the neutron emission, since it is these low energy X-rays which do not seem to be correlated with the neutron output.

4.3 Electron Distribution

If the continuum X-rays are bremsstrahlung (*i.e.* from free-free transitions) and the distribution of the electrons are Maxwellian, then the emission per unit frequency interval and unit volume is

$$P\nu = C\, N_e N_i\, Z^2\, (\chi_H/kT_e)^{\frac{1}{2}}\, \bar{g}\, \exp(h\nu/kT_e) \ ,$$

where $C = 1.7 \times 10^{-40}$ erg cm^3

$\nu = E/h$ is the frequency;

E is the energy of the photon;

h is Planck's constant

N_e, N_i are the electron and ion number density respectively;

Z is the ion charge;

χ_H is the hydrogen ionisation potential;

T_e is the electron temperature; and

$\bar{g}$ is the Gaunt factor, averaged over the Maxwellian distribution, and also a function of T_e [Elwert 1954].

If $n(E)$ denotes the number of photons of energy E reaching a foil of thickness d, the number n' of photons transmitted is

$$n'(E) = n(E) \exp(-\mu(E)d) \ ,$$

where $\mu(E)$ is the linear absorption coefficient for the foil material. From these expressions, it can be seen that the total intensity transmitted through a foil will be a function of T_e, n_e and d. If the continuum contains recombination (*i.e.* free-bound) radiation, then this can be allowed for by a change in $\bar{g}$, since the energy dependence contains the same exponential factor.

If the intensity is measured behind two foils (differing either in thickness, material, or both), then T_e can be calculated from relative intensity measurements only. Tables can be constructed by integrating the emitted power, multiplied by the response of the filter-detector system, over the energy to obtain the total relative transmitted intensity for different materials, thicknesses and electron temperatures (*e.g.* Jahoda *et al.* [1960]). The electron temperatures thus derived will be accurate if there is no line radiation and the transmitted energy is on the same continuum. Since the absorption coefficient increases rapidly with decrease in energy and the line radiation must be of lower energy than the recombination radiation, the line radiation will be very strongly attenuated if the thickness of the foil is such that appreciable transmission occurs only in the high energy part of the continuum. The specific values for 'low' and 'high' energy depends on the Z-value of the gas or of the impurities; for example, argon has lines around 3 to 11 keV. Since the bremsstrahlung contribution goes as Z^2 and the recombination radiation as Z^4, even a small percentage of high Z impurities can contribute most of the continuum. A bremsstrahlung assumption in the presence of recombination radiation caused by impurities will give an apparent temperature rather than the real one, but the error is only $\sim$ 10 per cent [Brussard & van de Hulst 1962].

For a deuterium plasma, the line radiation greater than 1 keV is caused by fluorescence lines from the insert of the centre electrode and from copper, *e.g.* for copper there are Kα and Kβ lines at 8.04 keV and 8.9 keV respectively; for tungsten, the Lα, Lβ and Lγ lines are at 8.4 keV, 9.7 keV and 10.0 keV respectively.

By a suitable choice of scintillator thickness, a foil can act as a bandpass filter of radiation in a band located just below the K-edge. For radiation in the 1 to 5 keV range, suitable choices for filter materials are magnesium (K-edge at 1.31 keV), aluminium (1.56 keV), chlorine (in the form of Saran, 2.82 keV), and titanium (4.98 keV) [Bernstein, Lee and Hai 1971]. The results obtained for a typical shot at the peak of the plasma emission are given in Table 1, from which a value for T_e of 0.4 keV is obtained. This

result is consistent with the Rayleigh scattering result and also with T_i values of 0.7 to 1.0 keV as obtained from collapse velocity calculations (Section 3.4). The result is very low compared with all other measurements and, specifically, is inconsistent with the 2 to 7 keV electron temperatures obtained from the spectral shape by Mather *et al.* [1971].

TABLE 1

TYPICAL BANDPASS FILTER RESULTS AT PEAK PLASMA EMISSION WITH THE SIGNALS OF Al, Cl AND Ti DETECTOR UNITS NORMALISED TO THAT OF Mg. (Source: Bernstein, Lee & Hai [1971])

Experimental error includes uncertainty in calculated bandpass responses. Computed values of signals are for T_e = 0.3, 0.4, 0.5 and 0.6 keV

	Measured	Computed for T_e of			
		0.3 keV	0.4 keV	0.5 keV	0.6 keV
Mg	1.00	1.000	1.000	1.000	1.000
Al	0.70 ± 0.12	0.618	0.732	0.812	0.870
Cl	0.15 ± 0.04	0.071	0.156	0.260	0.370
Ti	0.03 ± 0.01	0.003	0.015	0.039	0.080

Figure 13(b) shows that during the first X-ray pulse (lasting about 200 nsec) at t_m, the fluorescence line of copper is of very low intensity, so pairs of aluminium filters absorbing over a range greater than 4 keV can be used for temperature determinations. The filters selected were A_1 (45.4 mg cm^{-2}), A_2 (11.4 mg cm^{-2}) and A_3 (92.4 mg cm^{-2}), all made of aluminium; the ratios A_2/A_3 and A_2/A_1 were used [Patou 1970]. The results gave a change of T_e from 2 keV at the beginning to 6 keV at the end of the pulse (Figure 17(a)).

From the expression for the power emission at a given frequency, it can be seen that a measurement of the relative intensities at two frequencies is sufficient to give the temperature. The measurements were made at 1 A and 0.5 A (*i.e.* 12.4 keV and 24.8 keV) with a spectrometer and the results compared with the filter pair A_2/A_1 for a given shot. Figure 13(c) shows that the results are similar, although the spectrometer results appear to be a little higher. Patou [1970] considered that this was caused by the much higher sensitivity, and associated fluctuations, required for the spectrometer photomultipliers.

A further measurement of the temperature with a series of aluminium foils of thicknesses ranging from 2 to 7 mg cm^{-2} for a deuterium filling

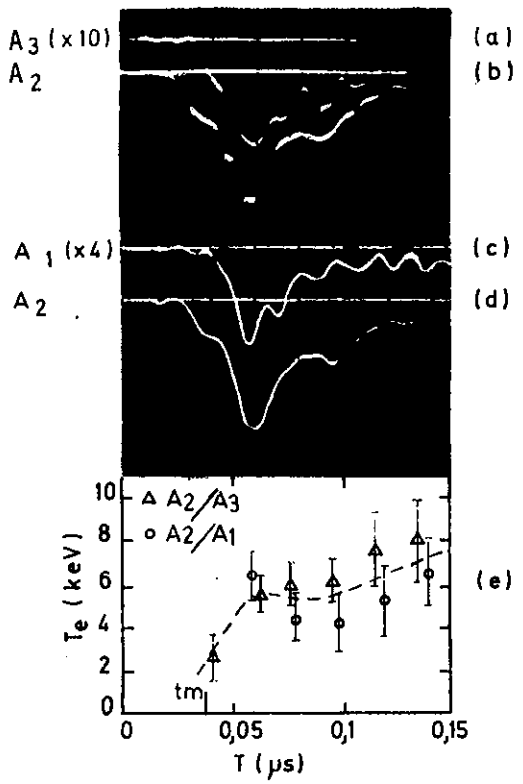

FIGURE 17(a)

Measurement of the electron temperature of the plasma using aluminium foils A_1, A_2, A_3.
(Source: Patou 1970)

$n_e \sim 1.5 \times 10^{19}$ cm^{-3}, τ is 70 nsec which is a similar period to the emission pulse. This effect is probably more significant in cases where the main X-rays come from a higher Z impurity, *e.g.* argon.

4.4 Copper Contamination

An attempt has been made to determine the level of copper contamination, together with the electron and ion temperatures and densities, by absolute measurements of X-ray intensities and the neutron emission [Beckner 1966]. From the spectroscopic study in Figure 13(b), it is seen that the copper contamination rises to appreciable levels at the time of the second and subsequent X-ray pulses. During the first pulse, the level is very low. This is consistent with the above results (Figure 17(b). It is noted that, for all the foil measurements quoted, the apparent temperature increases with increasing thickness (*i.e.* as higher energy bands are sampled). In the results of Peacock *et al.* [1968] the temperatures range from 500 eV to 2 keV whereas in the results of Patou, attained with much thicker foils, the temperatures range up to 6 keV. The reason for this phenomenon is not clear; possibly the ion populations may not have had time to reach a steady state with all levels of excitation. A measure of this time τ is given by McWhirter [1965] as

$$n_e \tau \sim 1 \times 10^{12} ,$$

where n_e is the electron density. At

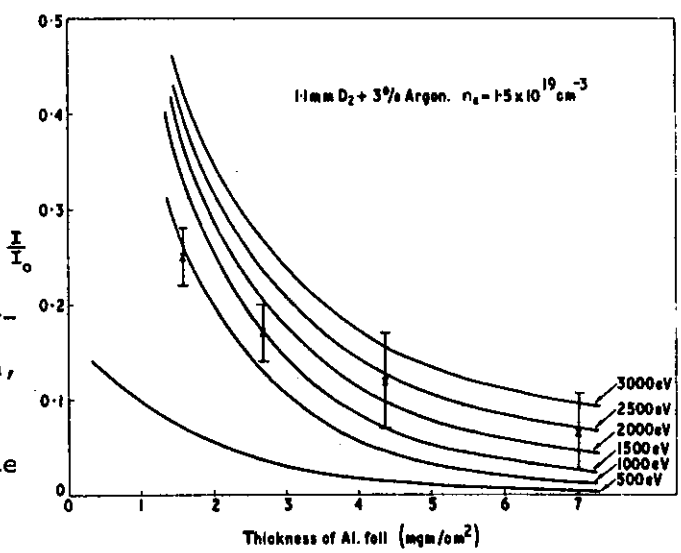

FIGURE 17(b)

Calculated transmission through Al foil for varying plasma temperatures compared with experimental values (initial gas pressure p_o = 1.1 torr + 3% A).
(Source: Peacock et al. 1968)

firmed by the results shown in Figure 18(a) and (b) where the copper level is less than 0.1 per cent during the first pulse, and rises to 1 per cent during the second.

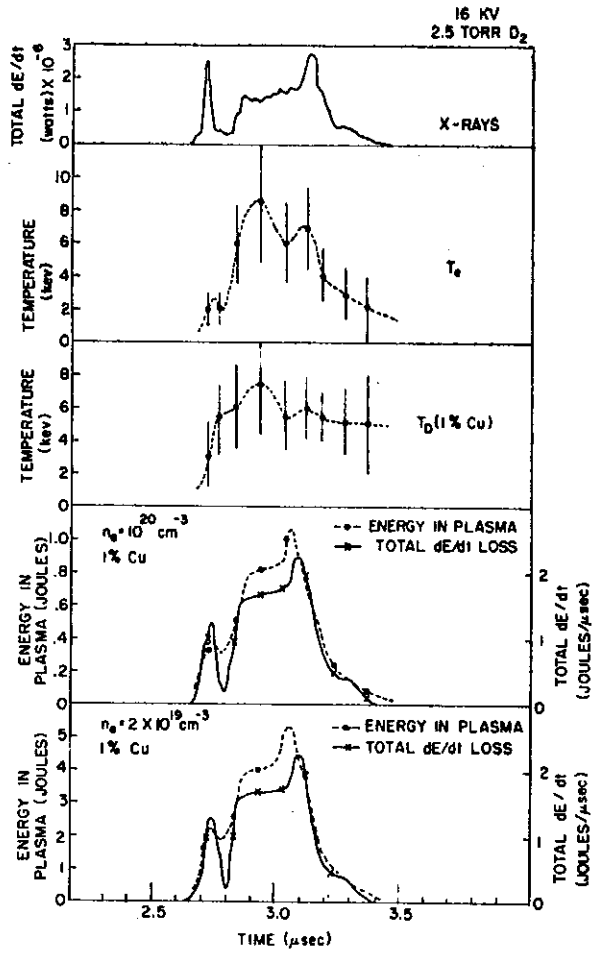

FIGURE 18(a)

Results of analysis of the data of Beckner. The electron temperatures were obtained from the X–ray data. The quantity $n_e^2 V$ was obtained from the measurements of X–ray emission rate and determination of the copper contamination level (see Fig. 18(b)); the plasma internal energy was then computed from $n_e^2 V$, T_e and T_i for the values of electron density shown. (Source: Beckner 1966)

The X-ray measurements were made through iron, beryllium, nickel and copper filters, chosen so that the K-edges occurred to separate the H-, He- and Li-like lines of copper. The major assumptions made in the calculations were

(i) the ion distribution was steady state and could be found from the corona model;

(ii) each species of particle had a Maxwellian distribution; and

(iii) the neutron emission had a thermonuclear origin and hence could be used to determine the ion temperature.

The measurements and equations were not sufficient to define all quantities uniquely, but a self-consistent set of values that was consistent with

the measurements could be obtained, and these were critically examined in the light of other knowledge of the plasma focus. The electron and ion temperatures thus found appear to be somewhat high compared to the previous measurements. The weakest assumption is (iii) although the results should not be very sensitive to this; also (ii) might not hold for the electrons. The evidence of the X-ray emissions leaves open the question as to whether or not the electrons are Maxwellian in the 5 to 30 keV range.

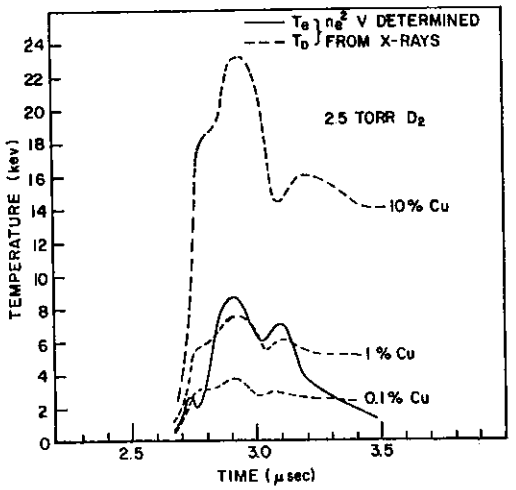

FIGURE 18(b)

Ion temperature determinations as a function of the level of copper contamination, obtained from the X-ray and neutron emission rate measurements.
(Source: Beckner 1966)

TABLE 2

(Source: Peacock, Hobby & Morgan 1971)

Ion	Transition	λ (Å)	Order n	$\Delta\lambda_{1/2}$ (Gaussian)	T_i (equiv)	Z	M
Ar XVII	$1s^2\ {}^1S_o$ - $1s2p\ {}^1P_1$	3.9492	1st	0.0046	9 ± 3 keV	16	40
Ar XVII	$1s^2\ {}^1S_o$ - $1s2p\ {}^1P_1$	3.9492	3rd	0.0048	10 ± 1 keV	16	40
Ar XVII	${}^1S_o$ - ${}^3P_1$	3.9689	1st	0.0047	9.4 ± 1 keV	16	40
Ne X	1s - 2p	12.1340	1st	0.0203	9 ± 1 keV	10	20
DII					~1° → 2 keV*	1	2
					< 5 keV+		

4.5 Ion Temperatures

The ion temperature of a heavier gas used as a seed in the deuterium can also be measured by studying the profiles of the emission lines. Argon is a convenient material having lines around 3.9 Å [Peacock, Hobby & Morgan 1971]. When the instrumental effects are eliminated, the remaining profile is a Maxwellian distribution from which temperature can be obtained. From Table 2 it can be seen that very high temperatures are obtained up to 9 to 10 keV. The time correlation of this argon line with dI/dt indicates the presence of the line throughout the focus (Figure 19(a)), but the profile is a time-averaged one and so indicates the maximum temperature.

These measurements were taken viewing the focus perpendicularly to the axis and so do not give the velocity distribution along the axis. Hence

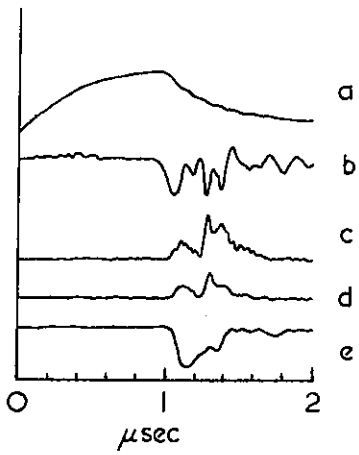

FIGURE 19(a)

Electrical, soft X-ray and neutron diagnostic time sequences of a Plasma Focus discharge; V = 28 kV, p_o = 2.5 torr (D_2 + 4% Ar). (a) I, (b) dI/dt, (c) soft X-rays, Ar XVII He-like wavelength, (d) soft X-rays, Ar XVI Li-like wavelength and continuum, (e) neutrons (corrected for time of flight). (Source: Peacock et al. 1971)

there may be a non-thermal component of the distribution along the axis (*i.e.* the possibility of axially accelerated ions is not eliminated).

As the temperature measurement is consistent with the assumption that all the ion components are at the same temperature, a neutron output much greater than that observed would be implied, and therefore it is more reasonable to suppose that only the measured component has that temperature. The deuterium ions are assumed to have a temperature of 1 to 2 keV as measured by Thomson scattering [Bernard *et al.* 1971(a)] and from shock wave calculations [Toepfer, Smith & Beckner 1971]. A scaling with Z^2/M gives the best fit and the component temperature T(Z,M) could be written

$$T(Z,M) = T_o(1 + Z^2/M) ,$$

where Z is the ionic charge, M is the atomic mass and T_o is the true thermal component. For the results given, T_o is 1.4 keV. There seems to be no plausible theoretical basis for this expression and, since the ion-ion collision times are of the order 1 to 10 nsec, the existence of different temperatures for each ionic component is difficult to understand.

Mention has been made of the correlation of the neutron emission with the presence of X-ray radiation in the 30 to 60 keV range. There is also a correlation of the neutron yield with the maximum amplitude of the second X-ray burst [Gratreau *et al.* 1971] (Figure 19(b)). Since this burst appears to be largely the radiation from a cloud of copper ions and starts after the beginning of the neutron pulse, the two events have a common underlying cause.

The ion temperature may be estimated also from the total neutron yield, the emitting volume, the density as measured (for example, by interferometry) and the assumption of a thermal origin for the neutrons. This temperature comes to ~ 2 keV [Bernstein, Meskan & Van Paassen 1969], and is consistent with some of the X-ray measurements of the electron temperature. However,

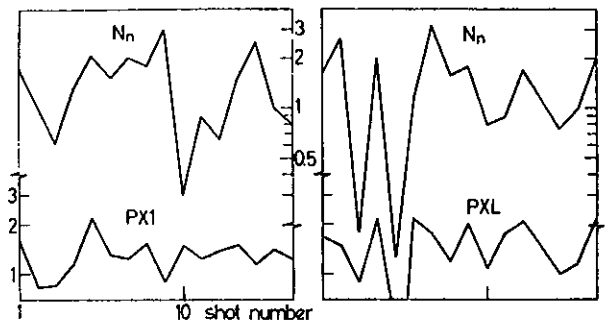

FIGURE 19(b)

Correlation between the total neutron yield (N_n) and the intensity of the first (PX1) and last (PXL) X-ray peaks (arbitrary units). (Source: Grateau et al. 1971)

there is some evidence which is against a thermal origin for the neutrons and this will be considered in Section 5.

Finally, the electron and ion temperatures can differ because of the long equipartition time t_{ie} for the energy of the electrons and ions, given by

$$t_{ie}\, n_e \sim 1.1 \times 10^{12}\, T_i^{3/2} \quad ,$$

for cold electrons to gain energy from hot ions. As seen earlier, the initial collapse will heat the ions more effectively (for $n_e = 10^{19}$ cm^{-3} and $T_i = 1.5$ keV, $t_{ie} \simeq 300$ nsec).

5. NEUTRONS

5.1 Total Neutron Output

When deuterium is used as a filling gas, one or more pulses of neutrons may be emitted. The neutrons are caused by the neutron branch of the D-D reaction,

$$D + D \rightarrow He^3 + n,$$

where the emitted neutron has an energy of 2.45 MeV. The length of the burst is about 150 nsec, with a full width at the half-maximum amplitude (FWHM) of about 70 nsec (Figure 10(a)); it starts within 20 nsec of the beginning of the X-ray emission. The burst is also coincident with a fading of the visible light. If there is no applied axial magnetic field at the electrode end, the neutron pulse exhibits a sharp rise to a peak and then a somewhat slower fall-off. With the application of an axial magnetic field of several hundred gauss, there is a rapid onset to a slowly rising (or plateau) level, followed by a sharp rise to the peak some 20 to 100 nsec later. The plateau feature becomes more prominent with increased magnetic field and decreased pressure (Figure 20(a) [Bernstein & Hai 1971].

The total number of neutrons for each focus event ranges from 10^9 to 10^{11} (usually measured by activation counters). For a given system and initial conditions, the neutron output is not reproducible. An example of a histogram for the neutron output for a series of shots in two situations, (a) deuterium at 3 torr and (b) deuterium at 3 torr with 2×10^{-2} torr xenon, is given in Figure 20(b) [Patou, Simonnet & Watteau 1968]. Attempts

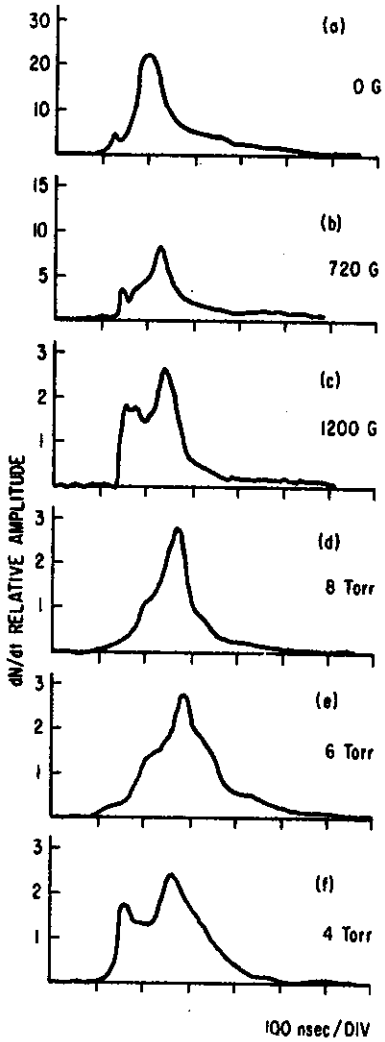

FIGURE 20(a)

(a) Intensity of neutron emission: (a)–(c) variation with B_z at 18 kV and 5 torr; (d)–(f) variation with pressure at 18 kV and 1200 G. All measurements at 90 deg with round tip. (Source: Bernstein & Hai 1971)

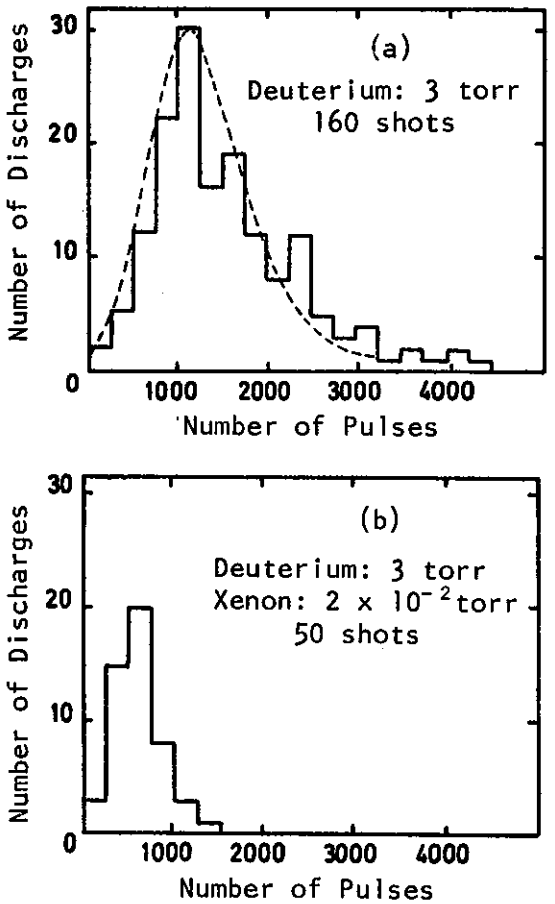

(1 pulse is equivalent to 1.3×10^6 emitted neutrons)

FIGURE 20(b)

(b) Neutron emission data for fixed initial conditions: C = 90 μF, V = 18 kV, p = 3 torr deuterium
(a) Deuterium
(b) Deuterium to which is added 0.6% xenon (Source: Patou et al. 1968)

have been made to correlate this fluctuation in yield with other parameters and the only correlation found so far is with the peak intensity of the last X-ray burst (Figure 19(b)).

The neutron yield N_o (averaged over many shots) has been found to scale with the various input parameters such as the applied voltage, the energy bank capacitance and the current. The results are

$$N_0 \sim I^4 \quad \text{up to 50 keV [Mather } et\ al. \text{ 1971]}$$

$$N_0 \sim V^{4-4.5} \text{ and } N_0 \sim C^{2.5} \text{ [Maisonnier } et\ al. \text{ 1971].}$$

The histogram shows that an appreciable number of shots produce no neutrons at all (see also Peacock *et al.* [1968]). This phenomenon becomes more frequent as the applied voltage is raised, although by altering the physical parameters of the gun, operation has been obtained up to 50 keV (see Section

2.1).

If the gas filling used is a mixture of equal parts of D_2 and T_2, a D-T reaction occurs giving 14.1 MeV neutrons, according to

$$D + T \rightarrow He^4 + n \ .$$

For a system emitting an average of 4×10^9 neutrons per burst for a D_2 filling, the neutron yield is increased to 3.3×10^{11} for a D-T filling [Mather 1966]. There is some question as to the exact value of this neutron yield of 14 MeV neutrons, since the values measured with an activation counter (see above) differ from those measured with an ionisation chamber (8×10^{11}) by a factor of two. If a Maxwellian distribution of the ions is assumed, the ratio of yields is given by

$$\frac{N_D \, N_T \langle \sigma v \rangle_{DT}}{1/2 (2N_D)^2 \langle \sigma v \rangle_{DD}} \ ,$$

where N_D,N_T are the deuterium and tritium number densities and $\langle \sigma v \rangle$ is the velocity weighted cross section averaged over the Maxwellian for the two reactions. This ratio is approximately 100 in the temperature range 2 to 10 keV, which corresponds to the measurements.

5.2 Neutron Flux

A scintillation detector, contained in 1.5 cm lead to shield it against X-ray emission, can be used to obtain the neutron flux as a function of time. Average energies of the neutrons can be obtained from the times of flight of the neutrons. Long flight paths, or nuclear emulsions, allow measurements of time averaged spectra.

Comparison between the time-integrated fluxes F_0, F_{90}, F_{180} at 0°. 90° and 180° respectively (angles to the axis in the direction away from the centre electrode) reveals anisotropies in the neutron flux. The F_0/F_{90} ratio measured with two activation counters, ranges in value from 1.18 [Maisonnier *et al.* 1971] to 2.0 [Patou 1970] depending on variables such as the filling pressure, the magnitude of the applied static magnetic field, the geometry at the centre electrode tip and the neutron yield. The only systematic studies published so far are for the variation of F_0/F_{90} with pressure and neutron yield. The following trends are observed:

(a) There is an increase of F_0/F_{90} with the neutron yield ranging from 1.28 at 2.4×10^9 neutrons to 1.48 at 1.0×10^{10} neutrons. The flux ratios in this case are measured with silver activation counters and hence are time-integrated [Lee *et al.* 1971]. A similar

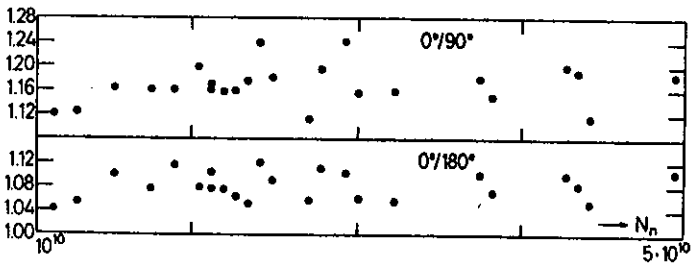

(a) Calibration corrected ratios of the neutron fluxes in the different directions as a function of the total DPF neutron yield, N_n. (32 kV; 1.3 torr D_2 ; Fast valve; 9-15 bar). (Source: Maisonnier et al. 1971)

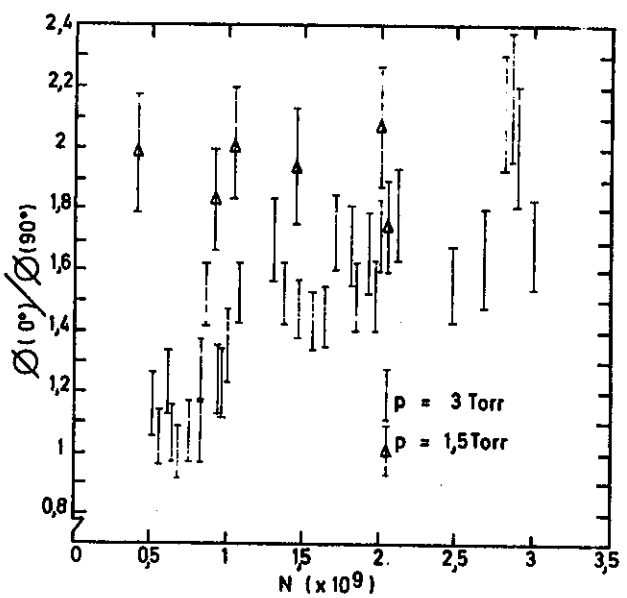

(b) Ratio $\phi(0^\circ)/\phi(90^\circ)$ for the number of neutrons emitted at 0° and 90° with respect to the discharge axis as a function of N, the number of neutrons emitted, for two pressures of the discharge chamber. (Source: Patou 1970)

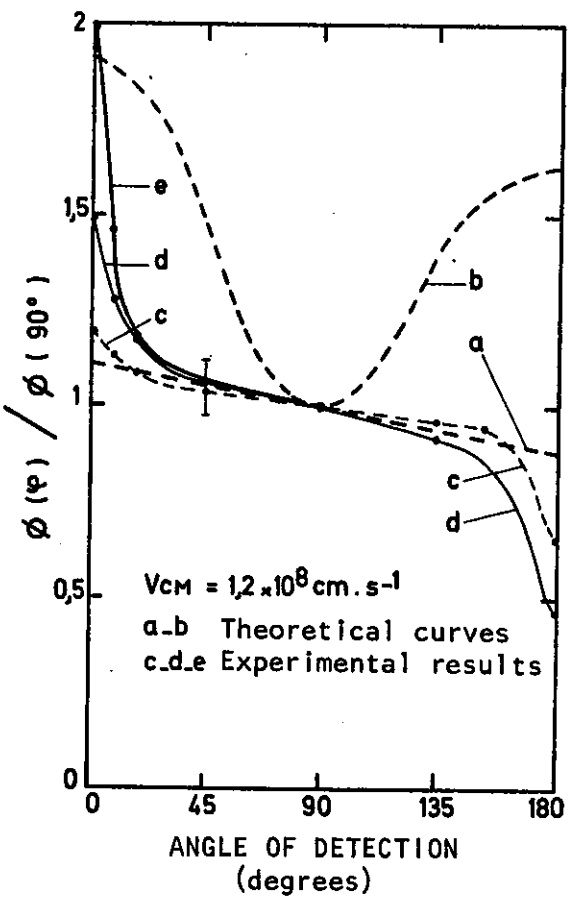

(c) Number of neutrons emitted per unit solid angle as a function of the angle of emission with respect to the discharge axis.

Theoretical curves:
- (a) M.T.P. model
- (b) m = 0 instability

Experimental curves:
- (c) p = 3 torr, N ≈ 1 x 10^9
- (d) p = 3 torr, N ≈ 2.5 x 10^9
- (e) p = 1.5 torr, whatever the value of N.

(Source: Patou 1970)

FIGURE 21(a) – (c)

measurement with a pair of activation counters, calibrated *in situ* with a Po/Be source, having a neutron energy spectrum similar to that of a D-D plasma focus, gives F_0/F_{180} and F_0/F_{90} values of 1.08 and 1.18 respectively. The values do not depend on bank voltage and their variation with neutron yield gives no systematic change and a large scatter (Figure 21(a)).

(b) An increase in F_0/F_{90} has been reported with a decrease in filling pressure [Patou 1970]. The variation of F_0/F_{90} with neutron yield for pressures of 1.5 and 3 torr can be seen (Figure 21(b)). Values as high as 2 are obtained at 1.5 torr. Figure 21(c) gives measurements at the same pressures for neutron yields of 1×10^9 and 2.5×10^9 for various angles Q from 0° to 180° (in the figure, $\Phi(\phi)$ is the time-integrated flux in the direction ϕ measured from the axis). These measurements are compared to the expected anisotropies for the moving boiler model and the target model and found to differ very significantly near 0° and 180° (see Section 6).

A study by Bernard *et al.* [1971(a)] at higher applied voltages (40 keV) and pressures (up to 25 torr) indicates a rapid increase of F_0/F_{90} with neutron output and a decrease with increase in pressure (Figure 22). The 25 torr data are especially interesting since they appear to show no anisotropy up to a yield of 1.5×10^{10}, and a rise after this point. One interpretation could be the existence of two mechanisms for the neutron production, one having only a slight anisotropy and the other a marked anisotropy. If the former mechanism is dominant at low yields and high pressures and the latter prevails at sufficiently high yields, then the above results will fit such a model. Such a model will be discussed in Section 6.

These results do not seem to be consistent with those given in Figure 21(a) taken at 32 keV and 1.3 torr. For large neutron yields at such a low pressure, Figure 22 implies a much higher anisotropy, unless the exact geometry of the different guns influences the result.

(c) At a pressure of 5 torr, the ratio G_0/G_{90} of the axial flux G_0 to the radial flux G_{90} at the peak of the neutron pulse (obtained by use of time-resolved detectors) is 1.28 for a flat-tipped centre electrode, whereas the value for a round tip is 1.45. A value for the round tip of 1.28 is found at 10 torr for the same neutron

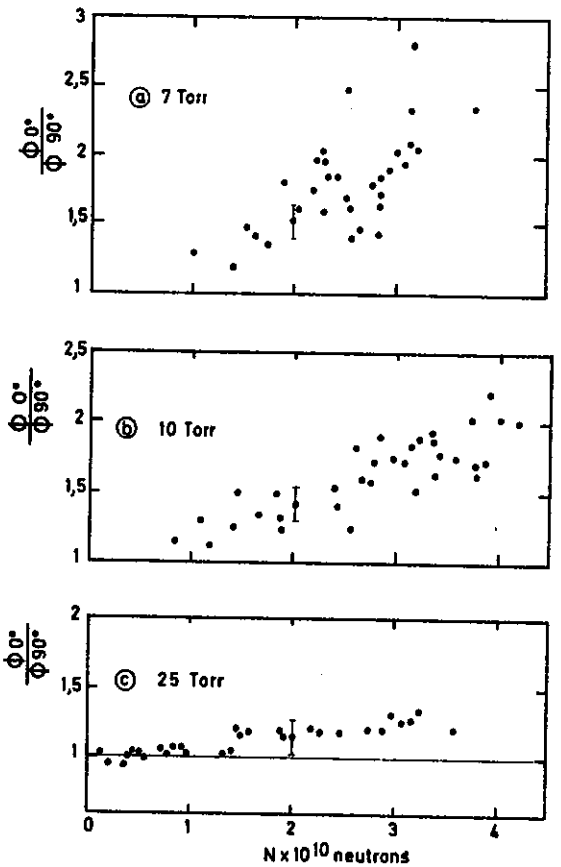

FIGURE 22
Neutron emission anisotropy

(a) Filling pressure 7 torr
(b) Filling pressure 10 torr
(c) Filling pressure 25 torr
(Source: Bernard et al. 1971)

yield [Bernstein & Hai 1971]. (These authors point out that the values will be high by 6 to 16 per cent for energy shifts of 200 keV to 500 keV between the average neutron energies in the radial and axial directions. This brings the values more into line with those quoted in (b) above.)

(d) With an applied axial magnetic field, measurements of G_0/G_{90} can be made at the time of the plateau and the peak; the results are as given in Table 3.

These values are for a round-tipped electrode and have not been corrected for the energy shift between the radial and axial spectra. It is to be noted that the anisotropy increases during the neutron burst.

The anisotropy measurements taken with the activation counters are only slightly dependent on the neutron spectrum while the scintillator measurements

TABLE 3

NEUTRON FLUX RATIO G_0/G_{90}

B gauss	G_0/G_{90} at plateau	G_0/G_{90} at peak	Pressure (torr)
0		1.45 ± 0.04	5
0		1.28	10
720	1.08 ± 0.06	1.53 ± 0.16	5
1200	1.20	1.57	5

can be in error up to 16 per cent for the spectrum differences encountered between the radial and axial directions. Corrections of the measurements are difficult and not normally done. The time-averaged measurements are less useful from a theoretical point of view; since the ratio varies with time, an average will be much less sensitive to the details of the model.

The average energy in the axial and radial directions obtained from flight tubes over short distances are typically 2.8 MeV and 2.5 MeV respectively. This implies a velocity of the centre of mass of the reacting ions in the axial direction.

5.3 Neutron Source Shape

Neutron collimators can be used to obtain the spatial distribution of the source, although the mapping must be done using a large number of shots. This makes it uncertain whether some of the spread is caused by the variability of the position of the source, or by its intrinsic spatial spread. If the detectors are placed at a given distance (*e.g.* 4 m) from the source, the scattered neutrons (which can be as much as 30 per cent of the signal) will be discriminated against by their late arrival. Since optical pictures give a radial dimension of less than a few millimetres, only the axial distribution has been investigated.

If the measurements are interpreted as representing the spatial spread of the source, the following results are obtained:

(a) A uniform source about 30 mm long starting within 5 mm of a flat-tipped anode (Figure 23(a)).

(b) The shape of the source does not appear to vary with applied voltage or filling pressure.

(c) From traces of the time-variation of intensity at each axial position, it is also possible to obtain the average intensity distribution at different times as a function of distance from the anode (Figure 23(c)). This indicates that the peak of the neutron

emission moves away from the anode during the event.

(d) With a round-tipped centre electrode, the major part of the source is shorter (~ 20 mm) and also is located 5 mm from the anode

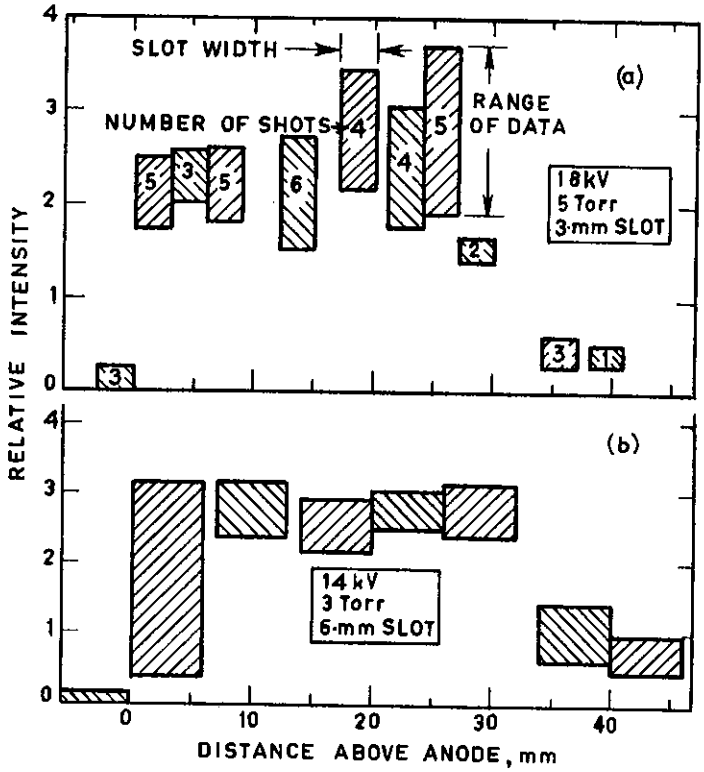

(a) Axial distribution of neutron intensity. Peak intensity of collimated pulse normalised to total pulse. (a) Operation at 18 kV with 5 torr D_2. (b) Operation at 14 kV with 3 torr D_2. (Source: Bernstein et al. 1969)

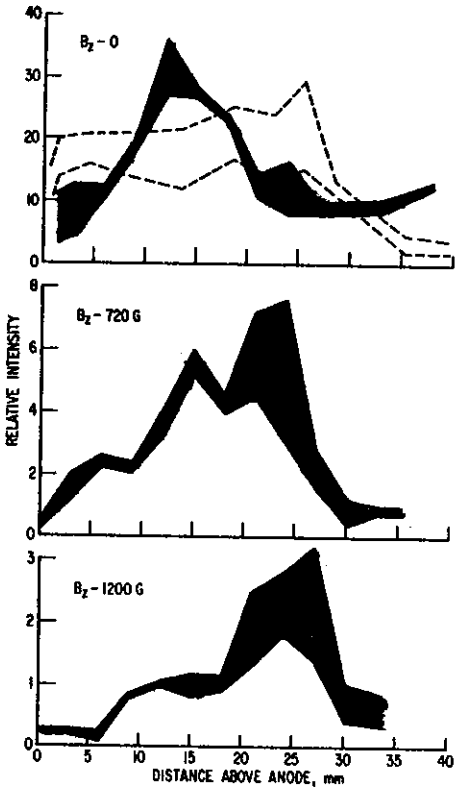

(b) Axial distribution of neutron intensity with round anode tip at 18 kV and 8 torr. For $B_z = 0$, dotted lines indicate previous measurements with a flat tip. Vertical width of bands represent range of several shots at each height; error on each shot equal to minimum width of band. (Source: Bernstein & Hai 1971)

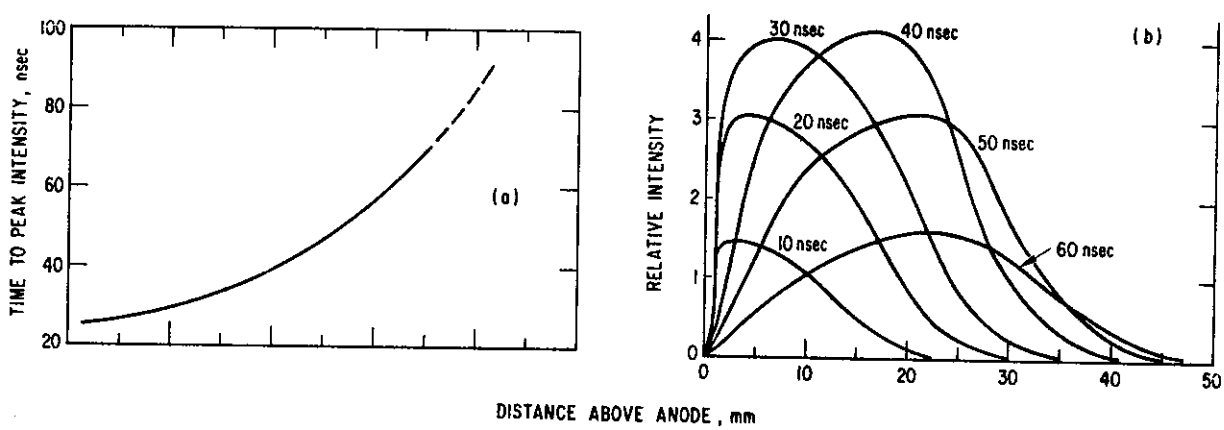

(c) Time history of neutron source as a function of axial position. (a) Average time to peak intensity of collimated pulse measured from beginning of neutron production. (b) Average intensity distribution at different times. (Source: Bernstein et al. 1969)

FIGURE 23(a) – (c)

(Figure 23(b)). The source is more concentrated and forms a peak between 10 and 15 mm from the anode, with a low intensity region extending beyond 35 mm.

(e) The position of the peak moves away from the electrode with an increase of the applied axial magnetic field and the long tail tends to disappear.

(f) The early plateau emission occurs mainly within 15 mm of the anode, while the later peak occurs predominantly in the region 15 to 30 mm from the anode [Bernstein & Hai 1971].

5.4 Neutron Spectrum

Time-integrated spectra can be obtained with nuclear emulsions. Care must be taken in the interpretation when converting from the proton spectrum in the emulsion to the incident neutron spectrum. Uncertainties arise in the angle of incidence of the neutron on the emulsion owing to the presence of scattered neutrons and to the finite size of the source. The effect of source size can be reduced by increasing the distance from the source, but this increases the number of the scattered neutrons. The usual technique is to limit track measurements to recoil protons scattered less than 30° from the presumed direction of the incident neutrons. By reducing this angle the proportion of scattered neutrons can be reduced further, but there will be fewer tracks. It is found that the shape of the spectrum is not greatly altered for angles less than 30°, except on the low energy side. The FWHM of the spectrum is measured by doubling the width of the high energy half; this reduces the effect of the scattered neutrons, which then will contribute mainly to the low energy side of the peak.

A typical spectrum is shown in Figure 24(a) [Maisonnier *et al.* 1971]. The histograms have been produced from scanning track angles less than 30° and less than 10°. The shapes of the spectra produced by different workers are very similar on the high energy side. Within experimental error, the FWHM is 500 keV for spectra measured axially (0°) and radially (90°). The peak of the radial spectrum is at 2.45 MeV and the peak at 0° is displaced towards the high energy side to 2.8 to 2.9 MeV. These results seem to be independent of the applied voltage and filling pressure, although most results obtained are for 18 keV and 3 to 8 torr. (The example in Figure 24(a) is exceptional and is for 36 keV and 1.2 torr.)

A considerably narrower spectrum of width 300 to 400 keV and centred at 2.7 MeV for 0° and around 2.2 MeV for 180° has been measured also [Patou 1970]. The conditions were 18 keV, 3 torr and 1.2×10^9 neutrons (Figure

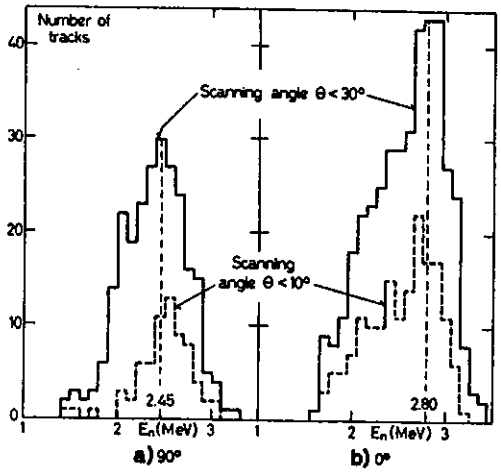

FIGURE 24(a)

(a) Neutron energy spectrum, E_n, as from nuclear emulsions exposed to a single shot (36 kV; 1.2 torr D_2; Fast valve ; 14 bar). Directions: (a) 90° ; (b) 0°. (Source: Maisonnier et al. 1971)

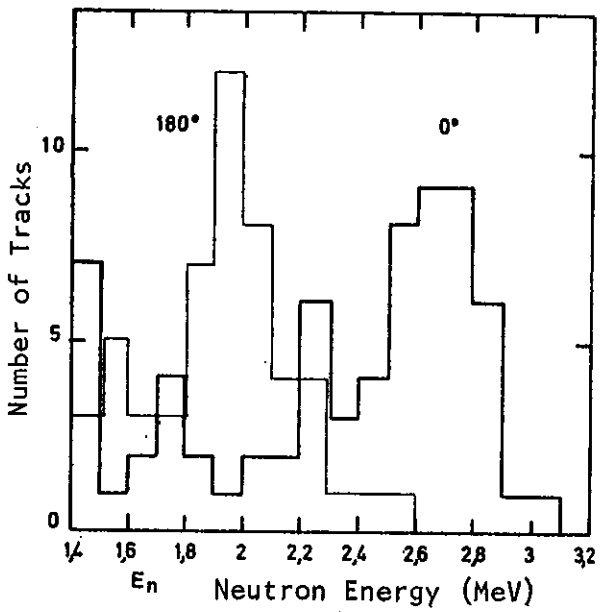

FIGURE 24(b)

(b) Result of the analysis of the tracks of two nuclear films irradiated during a single discharge, having produced a number of neutrons $N = 1.2 \times 10^9$. (Source: Patou 1970)

24(b)). The measurement at 180° is probably not very good because of the large component of scattered neutrons from the electrode.

The application of the axial magnetic field and changes to the shape of the tip of the electrode do not seem to affect the neutron spectrum. Another feature of the spectrum which is important is the maximum energy. In each direction (0° and 90°) the maximum energies are 700 to 900 keV greater than the average.

A further set of measurements of the time-integrated spectrum has been made using the time-of-flight method [Lee *et al.*1971]. An 80 m flight tube was used to obtain an energy resolution of 10 per cent. The advantage of this method over nuclear emulsions is the speed with which the velocity distribution can be obtained for each shot. The results are shown in Table 4, where

$\bar{E}$ indicates the averaging of the neutron energy over many spectra;

r,z indicate the radial and axial directions respectively;

ΔE is the FWHM of the spectrum; and

E_{max} and E_{gr} are the energies of the onset and the peak of the neutron time-of-flight signal respectively, *e.g.* $\overline{\Delta E}_r$ is the FWHM of the spectrum of neutrons emitted radially and averaged over many spectra.

The peak centre is 2.7 MeV at 0° and the width is ~ 270 keV, with a maximum energy of 450 keV above the peak. These values are smaller than the

typical emulsion values given above but, considering the errors in the emulsion values and the shot to shot scatter indicated in Table 4, there is no real inconsistency. The extreme values and the large scatter will have to be explained, as well as the averages.

TABLE 4

ENERGIES IN MEGAELECTRON VOLTS

(Source: Lee *et al.* 1971)

Axial	Radial	Anisotropy
$\bar{E}_{z,max} = 3.16$	$\bar{E}_{r,max} = 2.77$	$\bar{E}_{z,max} - \bar{E}_{r,max}$
$E_{z,max} - \bar{E}_{z,max}$:	$E_{r,max} - \bar{E}_{r,max}$	$= 0.39$ (14%)
$+ 0.42, - 0.52$	$+ 0.37, - 0.25$	
$\bar{E}_{z,gr} = 2.72$	$\bar{E}_{r,gr} = 2.50$	$\bar{E}_{z,gr} - \bar{E}_{r,gr}$
$E_{z,gr} - \bar{E}_{z,gr}$:	$E_{r,gr} - \bar{E}_{r,gr}$:	$= 0.22$ (9%)
$+ 0.36, - 0.23$	$+ 0.34, - 0.24$	
$\overline{\Delta E_z} = 0.27$	$\overline{\Delta E_r} = 0.27$	$\overline{\Delta E_z} = \overline{\Delta E_r}$
$\Delta E_z - \overline{\Delta E_z}$:	$\Delta E_r - \overline{\Delta E_r}$:	
$+ 0.23, - 0.13$	$+ 0.13, - 0.13$	

So far no time-resolved neutron spectra have been obtained, hence it is not known if the spectrum is constant during the event and only varies in intensity, or if the whole spectrum changes. The latter seems at least possible in view of some of the anisotropy results given above, so for all models a spectrum similar to the measured one is generally assumed.

5.5 Discussion

By making assumptions about the neutron-producing region, some deductions can be made from the measurements.

Firstly, some theoretical expressions are needed for the energy and energy spread of the emitted neutrons in simple models.

(a) For an axial beam of deuterons hitting a stationary target, the neutron energy E_n measured in the axial direction is given by Bernstein & Comisar [1972]:

$$E_n \approx W_n (1 + 2\gamma) ,$$

where $W_n = 2.45 + 3/8E_D$;

$\gamma = (E_D/8W_n)^{\frac{1}{2}} \ll 1$ for all approximations; and

E_D = deuteron energy in the laboratory frame.

(All energies are in MeV.)

Since a monoenergetic deuteron beam gives no spread of neutron energy in the axial direction, a range of deuteron energies are required for a finite width of the neutron line. In the radial direction, there is no shift of the neutron energy from W_n (*i.e.* 2.45 MeV to within the accuracy of measurement) nor is there any spread of the neutron line if the beam is axial. To obtain a spread in energies in the radial direction, one could consider a conical beam (the cone axis lying along the system axis) such that the deuterons approach the axis at an angle θ_D to the axis. Then the neutron energy in the radial direction will be

$$E_n = W_n (1 + 2\gamma \sin \theta_D \cos \phi) ,$$

where ϕ is the azimuthal angle between the plane containing the deuteron direction and the axis and the plane containing the neutron direction and the axis. Hence the energy spread ΔE_n about W_n will be

$$\Delta E_n = 4\gamma W_n \sin \theta_D .$$

The total number N of neutrons emitted at a given beam energy is given by Glasstone & Lovberg [1960] as

$$N = n_D n_T V t \sigma_{DD} v$$

for a beam of density n_D, striking a target of density n_T, with an interaction volume V for a time t. The cross section σ_{DD} is for the neutron branch of the reaction and v is the velocity of the beam deuterons.

(b) For a Maxwellian distribution of reacting deuterons, the number N of neutrons emitted in time t is given by

$$N = \tfrac{1}{2} n^2 V t \langle \sigma_{DD} v \rangle ,$$

where n is the density and $\langle \sigma_{DD} v \rangle$ is the average over the Maxwellian distribution.

The energy spread ΔE_n of the neutron line for a temperature T_D is

$$\Delta E_n = 82.5 \, T_D^{\frac{1}{2}} ,$$

where ΔE_n, T_D are in keV [Bernstein & Hai 1971].

If the centre of mass has an axial velocity, v_{cm}, the peak line

energy of the axially emitted neutrons is displaced from 2.45 keV. The neutron energy E_n of the peak is

$$E_n \simeq 2.45\ (1 + 2\gamma)\ \text{MeV}\ ,$$

where $\gamma = \dfrac{v_{cm}}{2.16 \times 10^9}$ for $\gamma < 0.1$.

(c) In the laboratory system, the differential cross section is defined by Bernstein & Comisar [1972]

$$\frac{d\sigma}{d\Omega_{lab}} = \sigma_T \frac{1 + A \cos^2\psi_n}{1 + 1/3\ A} \frac{(1 + 2\gamma \cos\psi_n + \gamma^2)^{3/2}}{1 + \gamma \cos\psi_n}\ ,$$

where $\cos\psi_n = -\gamma \sin^2\psi_e + \cos\psi_e\ (1 - \gamma^2 \sin^2\psi_e)^{1/2}$;

$\cos\psi_e = \cos\theta_n \cos\theta_d + \sin\theta_n \sin\theta_d \cos\phi$;

θ_n = angle of emitted neutron to the axis;

θ_d = angle of incident deuteron to the axis;

ϕ = azimuthal angle between axial planes of the incident deuteron and emitted neutron;

A = anisotropy of neutron emission;

$\sigma_T = 1.79 \times 10^{-23} \exp(-14.58/g)/g^2\ \text{cm}^2$; and

g = relative speed of the initial deuterons, for energies less than 80 keV.

For small γ, this can be shown to lead to flux anisotropies, measured by the ratio R of axially to radially emitted fluxes, as

(i) for a Maxwellian distribution of deuteron ions moving with a centre of mass velocity v_{cm}

$$R = \frac{(1 + \gamma)^{3/2}}{(1 - \gamma)^{1/2}}\ ,\ \text{and}$$

(ii) for a beam target system

$$R = (1 + A)\ (1 + 2\gamma).$$

(R refers to the quantities F_0/F_{90} or G_0/G_{90} above, depending on whether the flux is time-integrated or time-dependent.)

There is a controversy [Lehner & Pohl 1969] about the values of A for incident energies E less than 100 keV. Booth, Preston & Shaw [1956] suggest that from their measurements,

$$A = 0.31 + 0.0058\ E_D\ ,$$

where E_D (keV) = $1/2\ mg^2$, and m is the deuteron mass, while Theus, McGarry & Beach [1966] suggest a form corresponding to

$$A = 0.83 \arctan (0.02 E_D) .$$

As E_D approaches zero energy, the difference between the two forms becomes marked with the latter value for A approaching zero anisotropy at zero energy, while the former has an anisotropy even at zero energy.

Until this controversy is resolved, it is difficult to interpret anisotropies of the flux for non-isotropic distributions (*e.g.* the beam-target system) as real anisotropies of the distribution. We will give a sample calculation, but these should not be considered other than an indication. Table 5 gives the interpretation of the various neutron measurements of Table 4 in terms of two models, *i.e.* a moving thermal plasma and a beam-target

TABLE 5

MEASURED QUANTITIES INTERPRETED WITH THREE MODELS

(Source: Lee *et al.* 1971)

Measured Quantities	Moving Thermal-Plasma Model Ion Density = 5×10^{19} cm^{-3} Volume = 1×10^{-3} cm^3	Axial Beam-Target Model Ion Density = 5×10^{19} cm^{-3} Volume = 1×10^{-3} cm^3
Neutron Yield, Y_n		
$Y_n = 1.0 \times 10^{10}$	kT = 5 keV	E_d = 64 keV
$Y_n = 2.4 \times 10^{9}$	kT = 3 keV	E_d = 41 keV
Axial-to-radial neutron fluence ratio		
1.48 (at $Y_n = 1.0 \times 10^{10}$)	$V_{cm} = 4.4 \times 10^{8}$ cm/sec	E_d = 29 keV
1.28 (at $Y_n = 2.4 \times 10^{9}$)	$V_{cm} = 2.7 \times 10^{8}$ cm/sec	E_d = 16 keV
Neutron energy		
$\bar{E}_{z,gr}$ = 2.72 MeV	$V_{cm} = 1.1 \times 10^{8}$ cm/sec	E_d = 60 keV
$\bar{E}_{r,gr}$ = 2.50 MeV		
$\bar{E}_{z,max}$ = 3.16 MeV		E_d = 417 keV
$\bar{E}_{r,max}$ = 2.77 MeV		
Neutron energy spectra half-width		
$\overline{\Delta E}_z = \overline{\Delta E}_r$		(Axial only $\overline{\Delta E}_r = 0$)
Average 270 keV	kT = 11 keV	E_d = 15 - 136 keV
Maximum 400 keV	kT = 24 keV	E_d = 4 - 183 keV
Minimum 140 keV	kT = 3 keV	E_d = 33 - 96 keV

system [Lee *et al.* 1971]. To obtain values for the neutron yield, values are needed for the reaction volume V, the ion density n_D (or target density n_T and beam density n_B) and the emission time t. Reasonable values for these can be obtained from visible light and X-ray photographs. The values used are

$$V = 1 \times 10^{-3} \text{ cm}^3 ;$$
$$t = 100 \text{ nsec} ;$$
$$n_D = 5 \times 10^{19} \text{ cm}^3 ;$$
$$n_B = 5 \times 10^{19} \text{ cm}^3 ; \text{ and}$$
$$n_T = 3.5 \times 10^{17} \text{ cm}^3.$$

It can be seen that for neither model can a set of consistent plasma parameters be obtained to match the measured values, *e.g.* the temperature obtained from the neutron spectral width is much higher than that needed to give the neutron yield. A similar discrepancy arises for the velocity of the centre of mass. Some earlier measurements indicated that the moving thermal plasma model could describe the results but, since more neutron spectra have been measured, this appears now to be unlikely.

A simple model has been proposed [Patou 1971] correlating the X-ray results with the rate of neutron output, although no attempt is made to explain the detailed neutron spectrum. This model makes the following assumptions:

(i) the ion and electron temperatures T_i and T_e are equal;

(ii) the ion and electron number densities n_i and n_e are equal; and

(iii) the ion distribution is Maxwellian.

The electron temperature can be obtained as a function of time from relative filter measurements of the X-ray output as in Figure 17(a). Then a particular X-ray detector output w(t) can be corrected for the transmission factor G of the filters (assuming a bremsstrahlung source) as a function of T_e and hence as a function of time. This corrected output w'(t) is proportional to the X-ray power output P and

$$P = A\, n_i\, n_e\, V\, T_e^{\frac{1}{2}} = B\, w'(t),$$

where V is the volume of the emitting region and A and B are constants. From the above assumptions, the neutron output rate dN/dt is given by

$$\frac{dN}{dt} = \tfrac{1}{2}\, n_i^2\, f(T_i) ,$$

where $f(T_i)$ is the known reaction rate for a Maxwellian distribution of temperature T_i. These two expressions can be combined to eliminate n_i and

n_e, giving

$$\frac{dN}{dt} = \frac{B}{2AV} \frac{f[T_e(t)]w'(t)}{T_e(t)^{\frac{1}{2}}} \quad .$$

The constants are found by assuming they are the same for every shot and using the neutron output from a few shots.

Firstly, N can be obtained by integrating dN/dt and compared to the total neutron yield. Such a comparison is shown in Figure 25(a) and gives a good correspondence between the measured and calculated values. A comparison can then be made of the measured neutron rate with the calculated dN/dt from the above equation; two examples of this are given in Figure 25(b) and (c). Again, the correspondence is remarkably good considering that the assumptions are unlikely to be correct.

The results of this model give weight to the belief that a considerable portion of the neutron output must be due to a thermal ion distribution. Perhaps, more importantly, it indicates the general insensitivity of the calculated neutron output to the assumptions made.

5.6 Protons

The magnetic field inside the plasma focus can be probed by observing the emission of protons produced in the proton branch of the D-D reaction, *i.e.*

$$D + D \rightarrow T + H \quad .$$

An attempt at this has been made for the Filippov gun, but only very limited results have been obtained so far [Filippov *et al.* 1971]. The protons were observed mainly on the axis with nuclear emulsions, and histograms for the angular distribution of protons at the emulsion were found by measuring the tracks.

To interpret this data, angular distributions are calculated from a model. The magnetic field is computed from the assumption of a current sheath in the form of a surface of revolution with the equation

$$Z^2 = \alpha(r - r_o) \quad ,$$

where α, r_o are adjustable parameters. A point source of protons is assumed. Most protons are found to travel away eventually from the anode, except in a very narrow cone on the axis, this was confirmed experimentally.

At large distances from the anode, quite narrow distributions around the axis (half-angle up to 4°) are deduced from the model. This does not agree with the experimental data, which shows distributions with half-angle up to

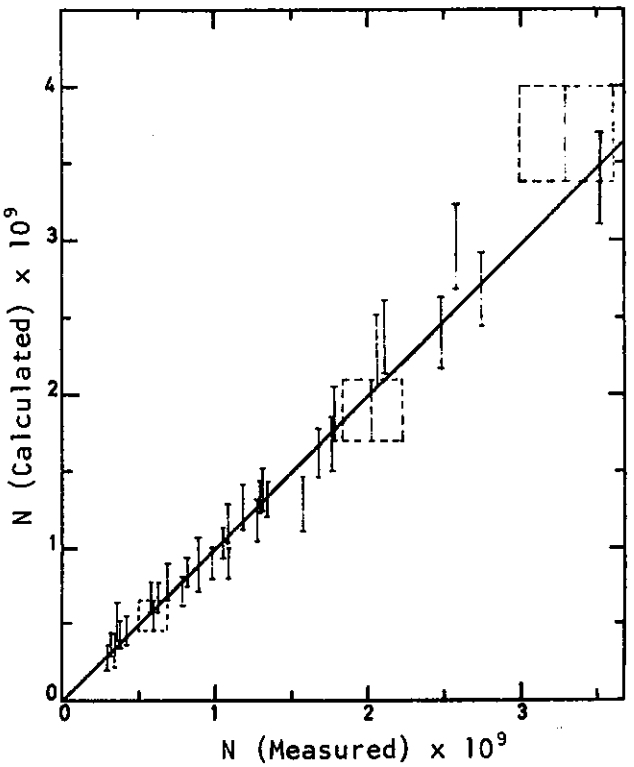

(a) Comparison between the number of neutrons measured and the calculated number of neutrons. (Source: Patou 1970)

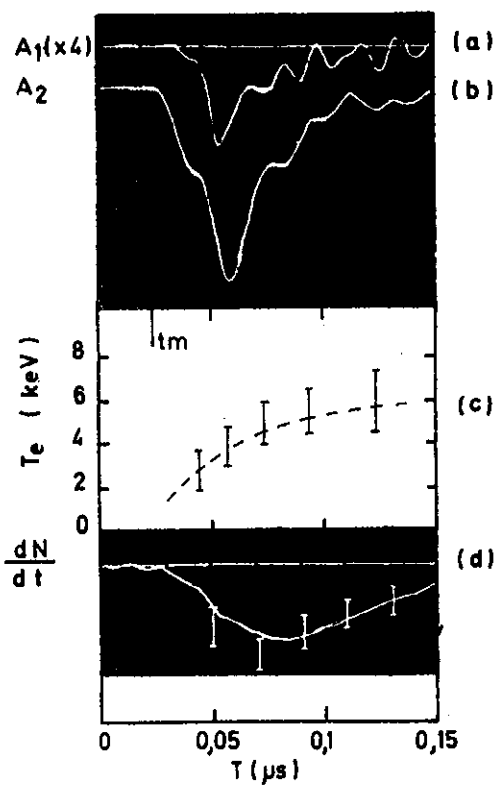

(b) Comparison of the measured and calculated values of dN /dt. (Source: Patou 1970)

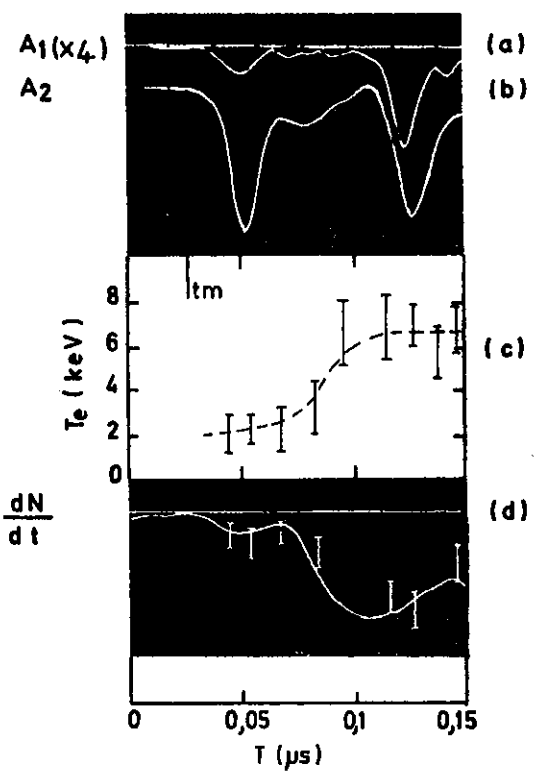

(c) Comparison of the measured and calculated values of dN/dt for a discharge which produced a very unusual neutron emission. (Source: Patou 1970)

FIGURE 25(a) – (c)

12°. The reason for this is not clear, but it implies protons moving at large angles to the axis far from the anode. No combination of α, r_o and movement of the source by 2 to 3 cm along the axis (the most that X-ray and neutron spatial distribution studies allow) will reproduce such proton distributions in the model.

If the experimental data are matched as closely as possible for the first 4° of the distribution, values of α and r_o are found which imply radii of the focus ranging from 0.5 to 2 mm and pinch magnetic fields of $1 - 4 \times 10^2$ Tesla.

6. NEUTRON PRODUCTION MODELS

Two basic methods of neutron production can be invoked:

- A thermonuclear model in which the reacting ions have a Maxwellian distribution in the centre of mass frame; or
- a beam-target model in which a beam of deuterons collides and reacts with a deuteron gas target.

6.1 The 'Moving Boiler' Model

The first model gave rise to the so-called 'moving boiler' model [Filoppov & Filippova 1966]. The essential feature of this model was a hot, thermal plasma moving along the axis away from the electrodes. This explained the shift of the spectrum for the neutrons from 2.45 MeV to higher energies, and the earlier result [Mather 1966] that there was very little anisotropy in the neutron emission. The width of the spectrum, together with the estimates of densities from X-ray emissions, gave plausible values for the temperature and density for the total neutron yield values (*e.g.* $n \sim 5 \times 10^{19}$ cm^{-3}, $T_i \sim 5$ keV with axial velocities $v \sim 2 \times 10^8$ cm sec^{-1}).

Further experiments (*e.g.* Bernstein & Hai 1970; Patou 1970; Lee *et al.* 1971) found much greater spectral widths and anisotropies. It was impossible to find consistent values for the parameters with this model, especially taking into account the low temperatures obtained by the laser scattering techniques. A typical set of values was shown in Table 5.

6.2 Simple Beam-Target Model

A simple beam-target model consisting of an axial beam colliding with the ambient gas is also very difficult to fit to the experimental results. The basic difficulty is to obtain the same FWHM value in the axial and radial directions. In the axial direction a spread of the spectrum can be obtained by a spread of the ion energies, but in the radial direction this model gives no such spread.

To obtain a spread in the neutron energy in the radial direction, the

model can be elaborated to the conical beam-target model. The beam is defined by a cone about the axis and there will be a spread in the radial direction related to the angle of the cone. This model was checked by Samuelli, Luzzi & Maisonnier [1971] and found to be incompatible with the experimental results. Specifically, it was found impossible to match the centre of mass velocity for the ions calculated from the flux anisotropy with that claculated from the time-of-flight and the nuclear emulsion data for the displacement of the peak from 2.45 MeV.

6.3 Two-component Model

A model has been suggested by Maisonnier *et al.* [1971] which consists of a mixture of the beam-target and the boiler models.

If the following quantities are defined

α = fraction of neutrons from the beam-target component,

a_2 = 4.55×10^{-10} x centre of mass velocity in cm sec^{-1} of the hot gas for the boiler component,

a_1 = 4.55×10^{-10} x centre of mass velocity in cm sec^{-1} of the beam-target component, and

A = coefficient of anisotropy of the $d(d,He^3)n$ cross section,

there are relations connecting those quantities with F_0/F_{90} and F_0/F_{180}, the values of 'a' as determined experimentally from nuclear emulsions or time-of-flight data as the apparent energy shift and the relation from cross section data between A and 'a'. If the measured quantities F_0/F_{90}, F_0/F_{180} and 'a' are put into these four relations, α_1, a_1 and a_2 can be solved.

In a typical case

$\alpha = 0.1$, $a_1 = 0.07$ and $a_2 = 0.008$

are obtained. These values imply that 20 per cent of the neutrons are from a beam of 105 keV and 80 per cent from a thermal plasma moving at 15×10^6 cm sec^{-1}. These results can also be verified from the nuclear emulsion histogram for the same event (Figure 26) measured axially and very close to the source (so that a minimum number of scattered neutrons are recorded). To break up the histogram into the two components, it is assumed that the number of scattered neutrons are negligible and hence the thermal component is a symmetrical distribution about 2.5 MeV (*i.e.* $a_2 = 0.008$) whose right-half is equal to the measured histogram for $E < 2.5$ MeV. The beam component is then the remainder after the thermal component has been subtracted. The result is that 20 per cent of the neutrons are due to a beam centred at 2.85 MeV; this is equivalent to a beam energy about 100 keV.

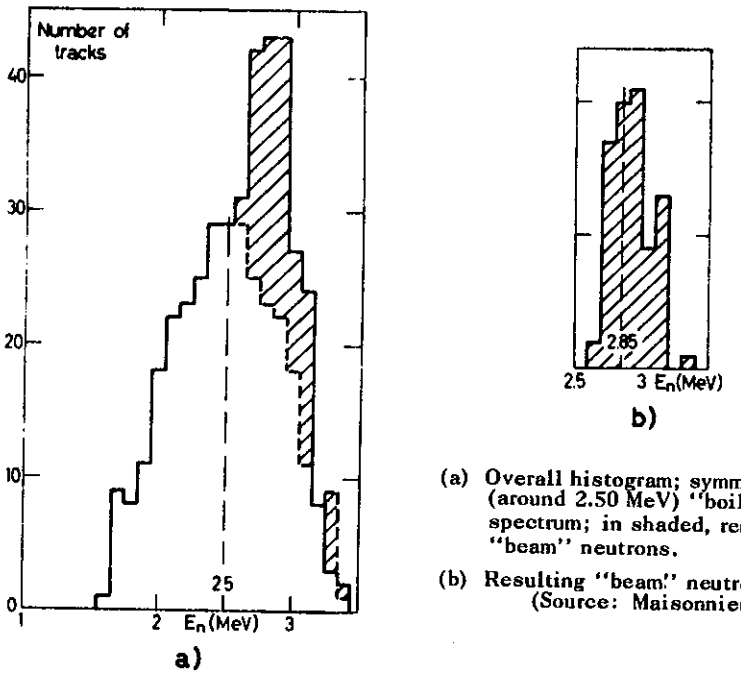

(a) Overall histogram; symmetric (around 2.50 MeV) "boiler" spectrum; in shaded, remaining "beam" neutrons.

(b) Resulting "beam" neutron histograms. (Source: Maisonnier et al. 1971)

FIGURE 26
Retrieval of the histogram of the 'beam' neutrons

The drift velocity of 15 x 10^6 cm sec^{-1} of the thermal component is consistent with the velocities measured from streak photographs of the focus. This model does not give an origin for the beam deuterons.

6.4 The Potter Computer Model

Support for a model consisting of a mixture of thermal and beam-target models comes also from computer calculations with the FOCUS code (Appendix A) and modifications allowing a calculation of the orbits of a large number of non-adiabatic ions [Potter & Haines 1971]. The FOCUS code is a two-fluid, two-dimensional model for the plasma focus gun. The fluid calculations have provided good agreement with experiment for the formation stages of the focus, the heating and the density, electron temperature and dimensions of the hot pinch region. The parameters produced by the calculations are consistent with a thermal source for the neutrons if only the total neutron yield is considered. However, the discrepancy arises in the flux ratios and the velocity of the plasma. Some experiments give effective plasma velocities up to 2 x 10^8 cm sec^{-1}. Such velocities are almost an order of magnitude greater than the velocities obtained from the calculations ($\sim$ 3 x 10^7 cm sec^{-1}).

Two points can be noted from the computer results. Firstly, the Dreicer condition [Dreicer 1958] for runaway electrons is violated in the pinch region (consistent with the experimental observation of hard X-rays up to several hundred keV). Secondly, the ion temperature can become high enough for ion-ion collision time to become larger than the ion cyclotron time, and at small radii, where the magnetic field falls to zero, the ions become non-adiabatic.

This allows the existence of a singular class of ions which could have an important effect on the plasma properties.

Since the variables in the pinch stage are strong functions of the radius, but only vary slowly in the axial (z) direction, the ion plasma is described by the three variables - r, w_z, w_r. The ion plasma consists of K ions (K ~ 10^3 to 2 x 10^4), each of which moves in the r-z plane.

Since interest is directed to conditions in which the ion Larmor radius is larger than the Debye length and the ion cyclotron period is larger than the electron-electron collision time, quasineutrality is assumed and the electrons are described as a fluid.

The calculations are initiated by applying a step-function magnetic field, B_θ (only an azimuthal magnetic field is possible with a cylindrical symmetry) at large radii, and the particles are initially distributed uniformly over all the radii with a Maxwellian distribution of velocities. A shock develops with the implosion and produces a steady pinch at small radii. The resistivity is taken as constant and the magnetic Reynolds number is around one.

Two cases are distinguished. If the ion Larmor radius, a_i, is equal to the collisionless skin depth, λ_s, where

$$\lambda_s = \frac{C}{\omega_{pi}} ,$$

with C = velocity of light,

ω_{pi} = ion plasma frequency,

and both are of the order of the pinch radius R, the electric field E_r produced by the electron drift current j_z is dominantly large and given by

$$E_r = -\frac{j_z B_\theta}{m_e} ,$$

where m_e is the electron mass, giving large axial drifts to the ions. For this case, typical ion orbits are shown in Figure 27(a) and the distribution of particles in w_z-r at two different times are shown in Figure 27(b). The ions do not exhibit a singular component.

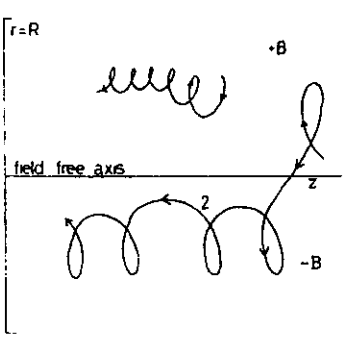

FIGURE 27(a)

Characteristic particle orbits for the case where runaway ions do not occur. The collisionless skin depth $\lambda_s = c/w_{pi}$ is of the order of the radius of pinch, and particles are electrostatically confined by a large negative radial electric field. Particles drift in the negative axial direction with a large E/B drift. The orbit (2) illustrates a particle which crosses the field-free axis of the pinch. (Source: Potter & Haines 1971)

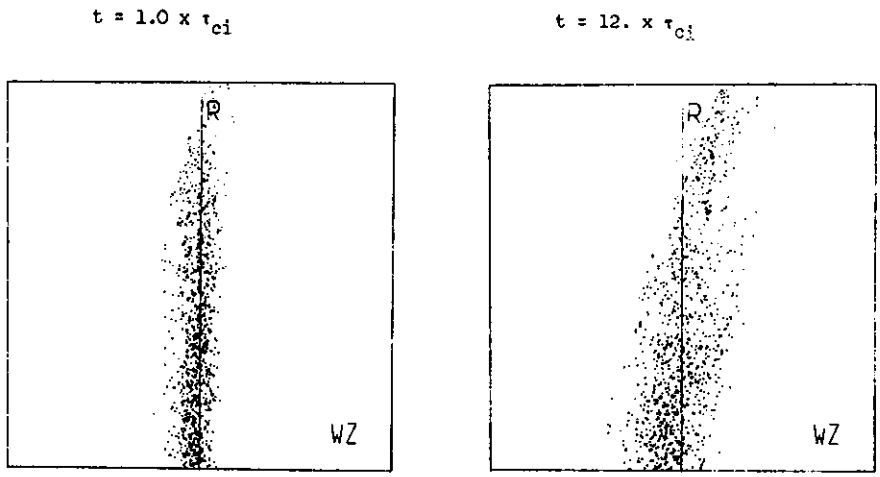

FIGURE 27(b)

The distribution of a representative set (1000) of particles in (r–w_z) phase space for the case where singular ions do not occur (the collisionless skin depth is of the order of the radius). A large negative radial electric field induces particle drifts particularly at small radii in the negative axial direction. A shear of the particles in phase space results.
(Source: Potter & Haines 1971)

The other case has $a_i = \lambda_s$ but is smaller than the pinch radius. Then it is found that if a small axial electric field is applied, the ion distribution rapidly acquires a singular component near the axis. The orbits and distribution of particles are seen in Figures 28(a) and (b). The singular particles are those crossing the axis more than once, since they effectively become trapped around the neutral line in the magnetic field. In Figure 28 a_i = 0.15 R and the magnitude of the applied electric field is

$$E_o = 0.05 \times \bar{w}\, B(R) \quad ,$$

where $\bar{w}$ is the average thermal velocity, and

$B(R)$ is the value of B_θ at r = R.

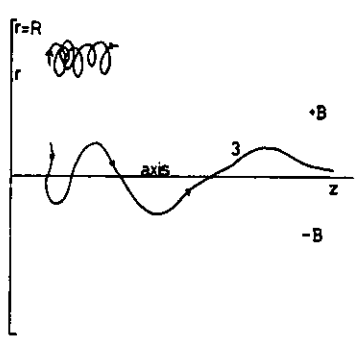

FIGURE 28(a)

Characteristic computed particle orbits for the case where runaway ions do occur. The collisionless skin depth is smaller than the radius of the pinch. The trajectory (3) illustrates the computed motion of a singular ion which is not trapped by the magnetic field and is rapidly accelerated to high energies as it crosses and recrosses the field free axis of the pinch.
(Source: Potter & Haines 1971)

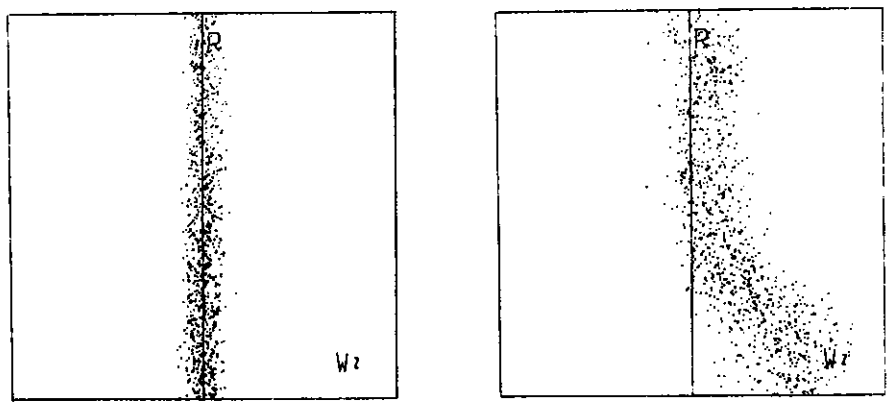

FIGURE 28(b)

The distribution of a representative set (1000) of particles in ($r-w_z$) phase space for the case where singular ions do occur (see Fig. 28(a)). Non-adiabatic particles near the axis of the pinch are not trapped and are freely accelerated to high energies by a positive axial electric field.
(Source: Potter & Haines 1971)

This applied electric field is not consistent with the model above since the variables are independent of the axial dimension, *i.e.* the electrons are adiabatic in the model and, in this case, no enhanced tail in the distribution can arise. Potter & Haines [1971] give the justifications for adding this field:

(i) the electrons violate the Dreicer condition and hence there will be runaway electrons; and

(ii) the X-ray emissions indicate large axial fields along the pinch during the focus stage.

The model itself does not give an origin for this field.

Assuming the production of a high energy tail to the distribution, neutrons will be produced because of the thermal component and the high velocity accelerated ions reacting with the background plasma. If typical values are used for the density and volume, and velocities corresponding to 100 keV deuterons (*i.e.* $\sim 3 \times 10^8$ cm sec^{-1}), a neutron yield around 5×10^9 is obtained; this is comparable to the yield from the thermal component. From Section 6.3 it can be seen that a typical neutron spectrum can be matched by a suitable combination of these two components. Strictly speaking, in both the models in Sections 6.3 and 6.4, the radial spectral width must be somewhat less than the axial width since radially, only the thermal component contributes.

6.5 The Bernstein Computer Model

Another beam-target model has been proposed by Bernstein [1970]. As

in the previous model, this depends on the acceleration of the ions to high energies in the magnetic field configuration of the pinch. However, no thermal component is required to obtain the spread of the radial neutron spectrum since this model gives a random distribution of direction for the accelerated ions.

The basic model assumes an axisymmetric, cylindrical current distribution, $j(r,t)$, which is finite in thickness and initially annular in shape. The distribution is then assumed to contract rapidly to the axis. This time variation in the current density gives rise to time-varying axial electric $E_Z(r,t)$, and azimuthal magnetic $B_\theta(r,t)$ fields whose values may be derived from Maxwell's equations. Since the actual current distribution is unknown, a reasonable analytic approximation is used for $j(r,t)$ to give E_Z and B_θ. These are used to obtain the trajectories of the deuterons for various initial conditions. If the ion-ion collisions are neglected, the motion is two-dimensional in the r-z plane. The current density is assumed to drop to zero at an outer boundary and the ion trajectories are confined to the region within the boundary.

A number of necessary major assumptions are now examined. The ion-ion collision time is assumed long enough to allow some ions to be accelerated to high energies. Owing to the decrease in the cross section with increase in energy, there will always be some ions with a sufficiently low collision rate. For the model an acceleration time up to 20 nsec is assumed, and for a density of 10^{20} cm^{-3} the collision time of ions with energies much higher than the random energy of the background is

$$t \sim 10^7 E_D^{3/2} (n \ell n \Lambda)^{-1} \text{ sec} ;$$

for 1 and 10 keV ions this is 0.6 and 10 nsec respectively. Thus at a temperature of 1 keV, a significant number of ions can be accelerated.

The current distribution was assumed to change from a distribution peaked on the boundary to a distribution peaked on the axis, but with the boundary moving inwards to the axis. This can be expressed by

$$j(r,R,t) = j_a + (j_b - j_a) (r/R)^\alpha ,$$

where r is the radial position and R is the radius of the boundary which depends on time through

$$\frac{dR}{dt} = - V_b \quad ,$$

where V_b is the velocity of the boundary and assumed to be constant (Figure 29(a)). The factors j_a and j_b are varied in time to obtain the desired change of distribution in a way consistent with the total discharge current; in this case, the total current has been assumed constant. The results for the model are fairly insensitive to values of α about 1, and $\alpha = 1$ was mostly used.

Such a change of the current distribution must occur at some time during the discharge, but this model requires the change to take about 20 nsec and occur just at the fading of the visible light on the streak photographs. (As seen in Figure 10(a), the fading is found to be the start of the neutron and hard X-ray emission.) This change in current distribution is equivalent to an assumption of a large increase of the plasma resistivity.

The usual Spitzer expression for the resistivity, η, for the electron cyclotron frequency, ω_{ce}, much smaller than the electron-ion collision frequency, ν_{ei}, is given by

$$\eta = \frac{5 \times 10^{-3} \ \ell n \ \Lambda}{T_e^{3/2}} \ \Omega \text{ cm} \quad ,$$

where T_e is the electron temperature, and

Λ is the usual Debye cut-off factor, a function of the density.

Hence it is seen that η is very insensitive to the density, but will rise with a reduction in the temperature.

For $\omega_{ce} \gg \nu_{ei}$, the above resistivity is increased by a factor $[1 + (\omega_{ce}/\nu_{ei})^{1/2}]$. For a density of 10^{20} cm^{-3} and a temperature of 100 eV, $(\omega_{ce}/\nu_{ei}) > 1$ for a magnetic field greater than 10^5 gauss. This will be achieved when the discharge current contracts to a radius of less than 1 cm. It is possible, therefore, that the necessary increase in η can be obtained in this way.

From shadowgraph pictures [Peacock, Hobby & Morgan 1971] it is seen that the compressed focus column which forms when the front reaches the axis, breaks up owing to various instabilities (chiefly m = 0) just before the neutron emission. The resistivity of the column would be expected to rise at this time owing to the turbulence generated by the instability.

The orbits of two typical trajectories starting at the same position

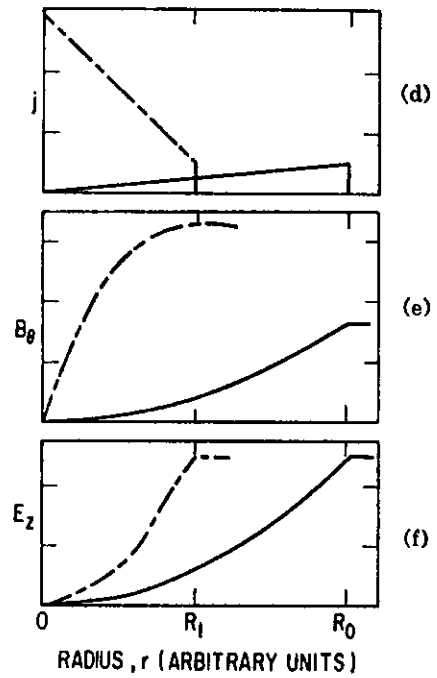

(a) Assumed current distributions j(r, R, t); (d) contracting with transition to axial concentration. Solid curves show initial distributions and broken curves show distributions at later times. All scales arbitrary and linear. Curves (e) and (f) give radial dependences of magnetic and electric fields for distribution (d). (Source: Bernstein 1970)

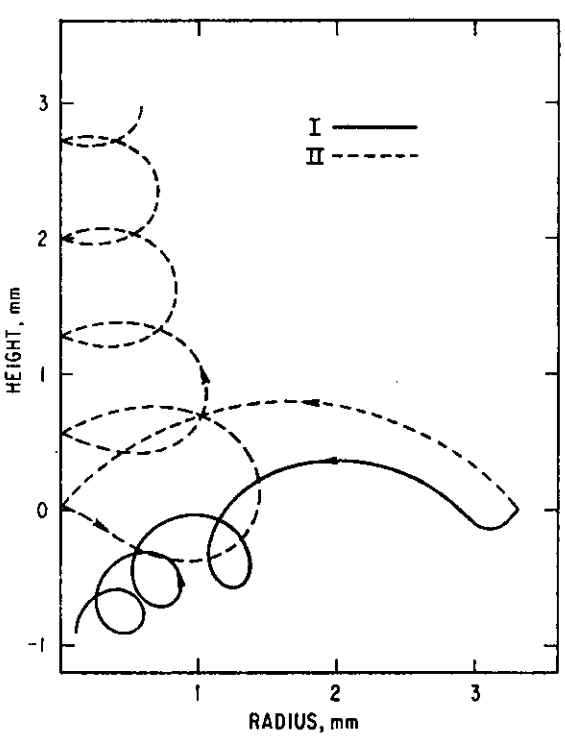

(b) Deuteron trajectories for two types of ion acceleration. Reflections from r = 0 in type II represent passage through the axis. (Source: Bernstein 1970)

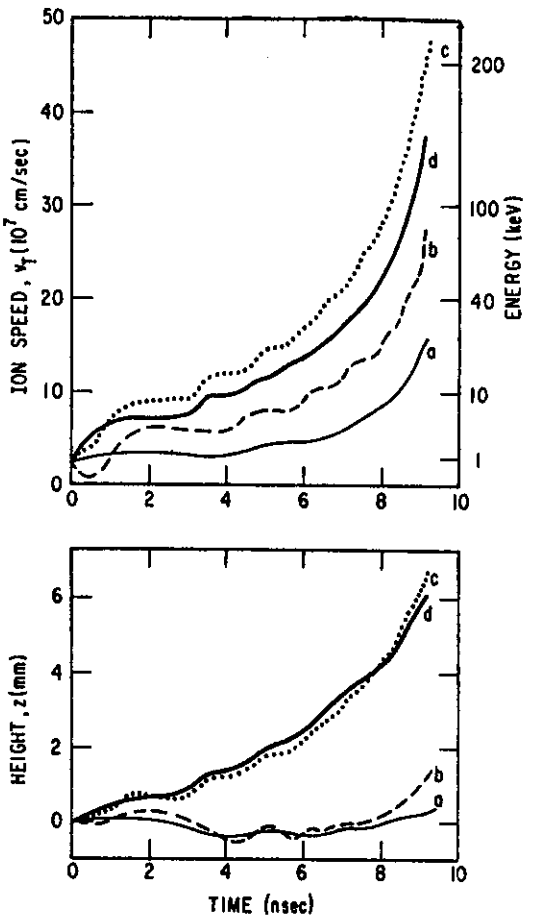

(c) Time dependences of deuteron speeds v_T and axial displacements z for ions having initially the same energy and radial position but starting with different velocity orientations. Initially $v = 2.5 \times 10^7$ cm/sec, r = 1 mm, and R = 2 mm with $V_b = 2 \times 10^7$ cm/sec and I = 700 kA. (Source: Bernstein 1970)

FIGURE 29(a) – (c)

and with the same v_r, but an opposite v_z, are shown in Figure 29(b). As in the previous model, there are two classes of trajectories. The ions of class I (with v_z towards the anode) never reach the axis, but drift against the electric field in the $\underset{\sim}{B} \times \nabla \underset{\sim}{B}$ direction. The ions of class II (with v_z away from the anode) oscillate through the axis and have a pronounced movement in the direction of the electric field. These are the ions which have large gains in energy.

The final energy is only weakly dependent on the initial energy, or on the magnitude of the discharge current. In Figure 29(c) it can be seen that gains in energy are dependent on the different initial velocity orientations, starting at the same position. The trajectories a and b having the lower energy gains can be seen to be class I, while c and d are class II trajectories.

On the basis of extensive calculations for different ions, it is estimated that up to 25 per cent of all ions could be accelerated in type II trajectories. The final number of ions accelerated to high energies will depend on the collisions and, for a random energy distribution averaging about 1 keV, this could be at least 1 per cent of the ions. Owing to the spiralling motion of the ions, it is clear that the angle of the velocity vector at a collision will be random in the plane perpendicular to the axis. Also the acceleration generates a large axial component of the velocity.

The energy attained is almost wholly dependent on the ratio of the final to initial radii of the current distribution. Theoretically, the minimum radius can be 0.1 mm for an average electron velocity of 10^9 cm sec^{-1} and density of 10^{19} cm^{-3}, and still carry a current of 1 MA.

Acceleration to high energies occurs within a few millimetres (Figure 29(c)) and hence the assumption that the collapse region relevant to the acceleration process is cylindrical is reasonable. Since over large scale lengths the collapse is non-cylindrical (being later at larger z, there is a possibility of a tandem mechanism for accelerating ions to very high energies. Computations also show that the large radial electric field does not significantly alter the general features of the ion orbits or the energy gains.

The ion distribution is required to obtain the neutron production and spectrum [Bernstein & Comisar 1972]. An examination of the ion trajectories for a wide range of initial parameters indicates an ion energy distribution decreasing rapidly with energy, resembling the $E^{-3.3}$ power law for the high energy electrons inferred from the hard X-ray measurements. Bernstein &

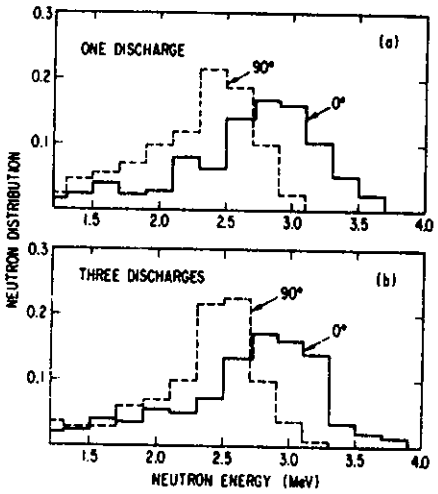

FIGURE 30(a)

(a) Neutron energy spectra obtained from Aerospace Corporation 33-kJ plasma focus device using a hemispherical anode tip and 8 torr D_2 ; (a) single discharge with emulsions 10 cm from centre of neutron source, (b) three discharges with emulsions 20 cm from source. (Source: Bernstein & Comisar 1972)

spectrum obtained from a 38 kJ device with a hemispherical anode tip is shown in Figure 30(a), with F_{90}/F_0 = 0.73 ± 0.05. (The low energy tails are caused by scattering, and no fluxes in the backward direction could be measured owing to scattering.) The ion spectra used to match these results are constructed to be consistent with the acceleration model (Figure 30(b)). The minimum energy is chosen to be 50 keV, since ions of lower energy are more likely to lose their energy by elastic scattering rather than in a fusion reaction. The distribution as a function of energy and angle was specified at 50 keV intervals. Also, it is to be noted that the lower energy ions are peaked in the radial direction, while the higher energy ions are peaked axially. The last graph of Figure 30(b) gives the theoretical neutron spectrum and flux ratios and Comisar [1972] feel that it is not unreasonable to choose the same power law for the ion energy, especially since the hard X-ray and neutron emissions start simultaneously. It is to be noted that no mechanism for accelerating the electrons has been proposed.

The neutron fluxes and spectra were calculated to match various experimental results. The important features are the general character of the ion spectra required. A typical

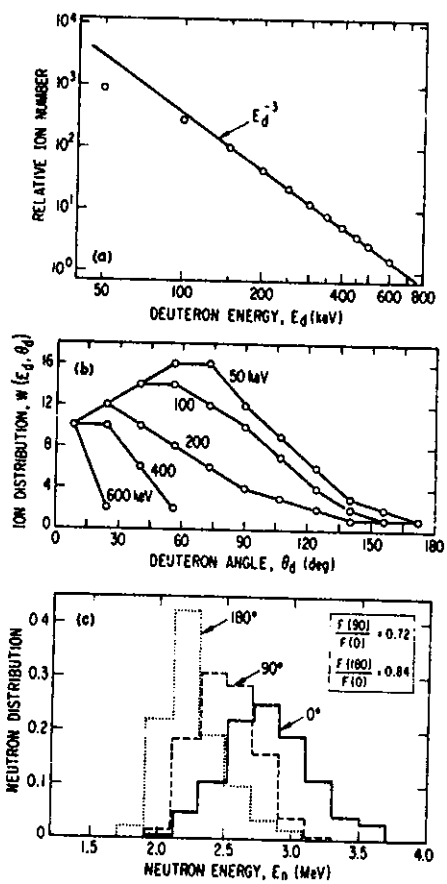

FIGURE 30(b)

Time averaged deuteron distributions giving results matching Fig. 30(a); (a) ion number distribution with values chosen at equal energy intervals of 50 keV, (b) angular distributions $W(E_d, \theta_d)$ for fusion collisions (distributions at other energies lie between the values shown), (c) resulting neutron energies and relative fluences.

(Source: Bernstein & Comisar 1972)

is a very reasonable fit to the experimental data.

A further example is given by matching some results reported by Bernstein & Comisar [1972] (Figure 31(a)). The relative flux ratios are $F_0:F_{90}:F_{180}$ = 1.00 : 0.80 : 0.90. These flux ratios and the spectrum could be quite closely matched with the ion distribution in Figure 31(b) (except for the low energy end which contains large numbers of scattered neutrons). The angular distribution for the ions is similar to that in Figure 30(a) and (b), but the deuteron energy spectrum (*i.e.* E^{-2}) is flatter.

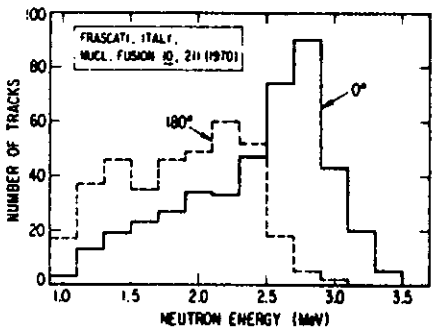

FIGURE 31(a)

Neutron energy spectra reported (Samuelli, Luzzi, Maisonnier) for plasma focus device at Frascati, Italy. (Source: Bernstein & Comisar 1972)

Similar results are found by matching other experimental results. Results which cannot be accommodated by this model are those having a flux at 180° less than the flux at 90°, *e.g.* $F_0:F_{90}:F_{180}$ = 1.00 : 0.90 : 0.80 [Mather 1966] and the results of Patou, Simonnet & Watteau [1969]. Attempts were made to have an axially moving target to try to accommodate these measurements. It is possible, in this way, to obtain the backward flux which, although smaller than the radial flux, is not sufficiently small.

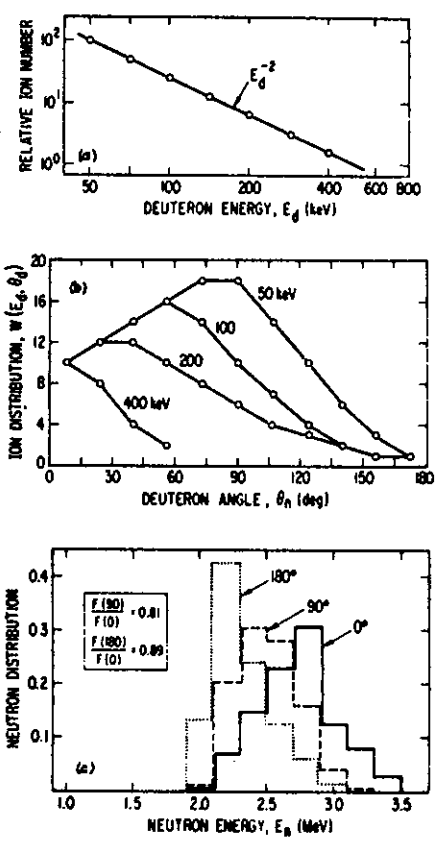

FIGURE 31(b)

Time-averaged deuteron distributions giving results matching Fig. 31(a); (a) ion number distribution with values chosen at energy intervals proportional to E_d, (b) angular distributions $W(E_d, \theta_d)$ for fusion collisions, (c) resulting neutron energies and relative fluences. (Source: Bernstein & Comisar 1972)

Hence it appears possible to match the spread and the position of the peak of the neutron spectra and the flux ratios for a large number of experimental results. It is clear that this mechanism contributes at least some of the emitted neutrons.

The above acceleration mechanism cannot operate for the electrons because of their much higher collision rate. Hence, the origin of the electron distribution and the reason for its

similarity to the ion distribution, at least as far as the energy spectrum is concerned, is left open to speculation.

7. CONCLUSIONS

The picture that emerges from the preceding discussion is of a current sheath produced by the breakdown across the insulator and driven along the electrodes to the muzzle of the gun by the $j \times \underset{\sim}{B}$ force. A shock which ionises and heats the gas to a few electron volts, while driving most of the gas to the wall, is set up in front of the sheath. It is the shock which is luminous. The luminous front appears to have radial striations, at least at the early stages of the discharge, so that the front is not azimuthally symmetric.

At the muzzle, a part of the ionised gas collapses to the axis to form a 1 to 2 mm diameter plasma line having a density and temperature greater than 10^{19} cm^{-3} and 1 keV respectively. Only 5 to 10 per cent of the gas swept up by the shock front during the collapse reaches the axis; the rest is driven axially away from the electrode out of the focus region. The shock ahead of the collapsing front can cause heating to several hundred electron volts, while the reflected shock at the axis, together with the magnetic compression, can raise this temperature to around 2 keV. Some tens of nanoseconds after the collapse, the line focus starts to break up due to $m = 0$ and $m = 1$ instabilities.

At this time, the plasma column appears to diffuse outward, a pulse of high energy X-rays (up to several hundred keV) is emitted and the neutron pulse starts. The X-ray spectrum is approximately thermal for energies less than 5 keV and has the form $E^{-3.5}$ at energies greater than 25 keV. The thermal portion of the emission corresponds to temperatures in the range 0.4 keV to greater than 4 keV. The temperature of the ions is around 1 keV and often is higher than the electron temperature. During the neutron emission, the density falls to less than 6×10^{18} cm^{-3}. The magnetic field is compressed to values greater than 100 Tesla.

The neutron emission is most likely made up to two components - one from a thermal ion population and the other from a high velocity ion beam accelerated in a magnetic neutral line configuration.

At each stage of the discharge there are still gaps in the experimental data and their theoretical understanding. A number of these have been pointed out in the text, but some of the more important points are reiterated.

It is important for scaling to higher energies that a more thorough understanding be gained of the breakdown process at the insulator, so that

it may be designed to eliminate secondary breakdown. While the scaling law found has the neutron output increasing as I^4, this obscures the fact that many shots have no neutron output at all because of secondary breakdown. Although a good focus has a very high neutron output, the average output over a period of time (an important factor in experiments using the focus as a neutron source) is low. This is caused by two factors: firstly, the low repetition rate, typically once every minute; secondly, the number of shots with a low output. Research is required into both these factors, particularly the second. A better understanding of the neutron output mechanism might indicate why many shots have a much lower output than average.

Hence a theory for the scaling laws requires an understanding of the electron and ion heating and acceleration mechanisms. Detailed time-resolved, and probably space-resolved, spectra will be required to find out what the differences are between a good focus and a poor one. A study of line spectra of high-Z impurities could also shed light on the heating mechanisms, but so far they have only complicated the picture. If it is verified that the ion temperature scales as Z^2/M, it may be possible to transfer some of the directed energy of collapse into thermal energy by the addition of a small percentage of heavy gas (but less than that required to cause radiative cooling [Peacock, Hobby & Morgan 1971]). Detailed studies of spectral lines help to relate the X-ray spectra to the electron distributions by shedding light on the ionisation and recombination mechanisms.

The spatial resolution data for the neutrons show that the maximum emission point moves away from the electrode during the emission, but there are no time-resolved spectral data. It will probably be a long time before time-resolved spectra are available for the neutrons, since there does not appear to exist an experimental technique for resolving neutron spectra on a nanosecond time scale.

Computer studies have helped to understand the focus, especially the high density and temperature phase where probe measurements are not possible. But two features of present codes limit their usefulness:

- their fluid dynamic character, since during the focus stage the conditions under which the fluid description holds are violated, possibly grossly for some classes of particles; and
- their limitation to azimuthal symmetry.

Since the existence of an asymmetry is known to exist, it is possible that this may play a very important role during the collapse. The first is partly overcome by an extension of one of the codes to include particles [Potter &

Haines 1971] which, as was indicated, gives a set of very important singular particles. The second limitation awaits larger computers to cope with three-dimensional problems.

Although some progress has been achieved in understanding the plasma focus gun, much still remains to be done before the main mechanism of the neutron emission can be fully understood.

8. REFERENCES

Agafonov, V.I., Moiseeva, M.P., Filippova, T.I. & Filippov, N.V. [1970] - LA-TR-70-25.

Amsden, A.A. [1966] - LA-3466.

Baconnet, J.P., Cesari, G., Coudeville, A. & Watteau, J.P. [1969] - Ninth Inter. Conf. on Phenomena in Ionised Gases, Bucharest, September 1-6, p.642.

Beckner, E.H. [1966] - J. Appl. Phys. 37 : 4944.

Bernard, A., Coudeville, A. & Watteau, J.P. [1970] - Phys. Lett., A33 : 477.

Bernard, A., Cesari, G., Coudeville, A., Jolas, A., de Mascureau, J. & Watteau, J.P. [1971(a)] - Proc. 4th Conf. on Plasma Physics and Controlled Nuclear Fusion Research, Madison, N.J. June 17-23 CN-28/D-4 IAEA, Vienna.

Bernard, J., Boussinesq, J., Morin, J., Nazet, C., Patou, C. & Vedel, J. [1971(b)] - Phys. Lett., A35 : 288.

Bernstein, M.J. [1970] - Phys. Fluids, 13 : 2858.

Bernstein, M.J. [1972] - Rev. Sci. Instrum., 43 : 1323.

Bernstein, M.J. [1972] - Bull. Am. Phys. Soc. 17 : 1022.

Bernstein, M.J. & Comisar, G.G. [1972] - Phys. Fluids, 15 : 700.

Bernstein, M.J. & Hai, F. [1970(a)] - Rev. Sci. Instrum., 41 : 1843.

Bernstein, M.J. & Hai, F. [1970(b)] - Phys. Lett., A31 : 317.

Bernstein, M.J. & Hai, F. [1971] - Phys. Fluids, 14 : 1010.

Bernstein, M.J., Lee, C.M. & Hai, F. [1971] - Phys. Rev. Lett., 27 : 844.

Bernstein, M.J., Meskan, D.A. & Van Paassen, H.L.L. [1969] - Phys. Fluids, 12 : 2193.

Booth, D.L., Preston, G. & Shaw, P.F.D. [1956] - Proc. Phys. Soc. (London) A69 : 265.

Bostick, W.H., Prior, W., Grumberger, L. & Emment, G. [1966] - Phys. Fluids, 9 : 2078.

Brussard, P.J. & van de Hulst, H.C. [1962] - Rev. Mod. Phys., 34 : 507.

Butler, T.D., Cook, J.L. & Morse, R.L. [1968] - Proc. APS Topical Conf. on Numerical Simulation of Plasmas, Los Alamos, Nev. September 18-20, LA-3990.

Butler, T.D., Henins, I., Jahoda, F.C., Marshall, J. & Morse, R.L. [1969] - Phys. Fluids, 12 : 1904.

Conrads, H., Cloth, P., Demmeler, M. & Hecker, R. [1972] - Phys. Fluids, 15 : 209.

Dreicer, H. [1958] - Proc. 2nd Inter. Conf. on the Peaceful Uses of Atomic Energy, United Nations, Geneva. September, Vol.31 p.57.

Dyachenko, V.F. & Imshemmik, V.S. [1969] - Soc. Phys. - JETP. 29 : 479.

Elwert, G. [1954] - Z. Naturforsch. A9 : 637.

Filippov, N.V., Filippova, T.I. & Vinogradov, V.P.. [1962] - Nucl. Fusion Suppl. Pt. 2 : 577.

Filippov, N.V. & Filippova, T.I. [1966] - Plasma Physics and Controlled Nuclear Fusion Research. Culham, U.K. September 1965. IAEA Vienna Vol.II, p.405.

Filippov, N.V., Agafonov, V.I., Belyaeva, I.F., Vikhrev, V.V., Gribkov, V.A., Golubchikov, L.G., Dyachenko, V.F., Imshemmik, V.S., Ivanov, V.D., Krokhin, O.N., Moiseeva, M.P., Sklizkov, G.V. & Filippova, T.I. [1971] - Proc. of 4th Conf. on Plasma Physics and Controlled Nuclear Fusion Research, Madison, N.J. June 17-23, CN-28/D-6. IAEA, Vienna.

Fishman, F.J. & Petscheck, H. [1962] - Phys. Fluids, 11 : 632.

Freiwald, D.A., Prestwich, K.R., Kuswa, G.A. & Beckner, E.H. [1971] - Phys. Lett., 4 : 297.

Gary, S.P. & Hohl, F. [1973] - Phys. Fluids, 16 : 997.

Glasstone, S., & Lovberg, R.H. [1960] - 'Controlled Thermonuclear Reactions' Van Nostrand, Princeton, N.J., p.243.

Gratreau, P., Luzzi, G., Maisonnier, C., Pecorella, F., Rager, J.P., Robouch, B.V. & Samuelli, M. [1971] - Proc. of 4th Conf. on Plasma Physics and Controlled Nuclear Fusion Research, Madison, N.J. June 17-23, CN-28/D-1. IAEA, Vienna.

Henins, L., Marshall, J. & Newton, A.A. [1968] - LA-4075.

Jahoda, F.C., Little, E.M., Quinn, W.E., Sawyer, G.A. & Stratton, T.F. [1960] - Phys. Rev. 119 : 843.

Jalufka, N.W. & Lee, J.H. [1972] - Phys. Fluids,15 : 1954.

Keck, J.C. [1962] - Phys. Fluids, 5 : 630.

Lee, J.H. & McFarland, D.R. [1972] - Bull. Am. Phys. Soc., 17 : 1023.

Lee, J.H., Shomo, L.P., Williams, M.D. & Hermansdorfer, H. [1971] - Phys. Fluids, 14 : 2217.

Lehner, G. & Pohl, F. [1969] - Institut für Plasmaphysik, IPP1/103.

Lie, T.N., Ali, A.W., Maclean, E.A. & Kolb, A.C. [1967] - Phys. Fluids, 10 : 1545.

Maclean, E.A. & Ramsden, S.A. [1965] - Phys. Rev., 140 : A1122.

McWhirter, R.W.P. [1965] - 'Plasma Diagnostic Techniques', Academic Press, N.Y. Chap.5.

Maisonnier, C., Gourlan, C. Luzzi, G., Papagno, L., Pecorella, F., Rager, J.P. Robouch, B.V. & Samuelli, M. [1971] - Proc. of 4th Conf. on Plasma Physics and Controlled Nuclear Fusion Research, Madison, N.J. June 17-23. CN-28/D2. IAEA, Vienna.

Maisonnier, C., Pecorella, F., Rager, J.P. & Samuelli, M. [1972] - Paper presented to 5th European Conf. on Controlled Fusion and Plasma Physics, Grenoble, August. European Physical Soc.

Marshall, J. [1960] - Phys. Fluids, 3 : 134.

Mather, J.W. [1963] - Bull. Am. Phys. Soc., 8 : 117.

Mather, J.W. [1964] - Phys. Fluids Suppl., 7 : 528.

Mather, J.W. [1965] - Phys. Fluids, 8 : 366.

Mather, J.W. [1966] - Plasma Physics and Controlled Nuclear Fusion Research, Culham, U.K. September 1965, Vol.II, p.389. IAEA, Vienna.

Mather, J.W. & Williams, A.H. [1966] - Phys. Fluids, 9 : 2080.

Mather, J.W. & Bottoms, P.J. [1968] - Phys. Fluids, 11 : 611.

Mather, J.W., Bottoms, P.J., Carpenter, J.P., Williams, A.H. & Ware, K.D. [1969] - Phys. Fluids, 12 : 2343.

Mather, J.W., Bottoms, P.J., Carpenter, J.P., Ware, K.D. & Williams, A.H. [1971] - Proc. of 4th Conf. on Plasma Physics and Controlled Nuclear Fusion Research, Madison, N.J. June 17-23. CN-28/D-5. IAEA, Vienna.

Morozov, A.I. [1968] - Sov. Phys. -Tech. Phys., 12 : 1580.

Morozov, A.I. [1969] - Proc. of 3rd Conf. on Plasma Physics and Nuclear Fusion, Nuclear Fusion Special Supplement. Novosibirsk, August 1968. p.111 (Translation). IAEA, Vienna.

Newton, A.A. [1968] - LA-4075.

Patou, C. [1970] - *J. de Phys.* 31 : 339.

Patou, C., Simonnet, A. & Watteau, J.P. [1968] - *J. de Phys.* 29 : 973.

Patou, C., Simonnet, A. & Watteau, J.P. [1969] - Phys. Lett. A29 : 1.

Patrick, R.M. [1959] - Phys. Fluids, 2 : 589.

Peacock, N.J., Forest, M.J., Hobby, M.G. & Morgan P.D. [1972] - Proc. 5th European Conf. on Controlled Fusion and Plasma Physics, Grenoble, August. p.66. IAEA, Vienna.

Peacock, N.J., Wilcock, P.D., Speer, R.J. & Morgan, P.D. [1968] - Proc. of 3rd Conf. on Plasma Physics and Nuclear Fusion, Novosibirsk, August. CN-24/G-4. IAEA, Vienna.

Peacock, N.J., Speer, R.J. & Hobby, M.G. [1969] - J. Phys. B (Atom Molecular Phys.) Ser.2, Vol.2 : 798.

Peacock, N.J., Hobby, M.G. & Morgan, P.D. [1971] - Proc. of 4th Conf. on Plasma Physics and Controlled Nuclear Fusion Research, Madison, N.J. June 17-23. CN-28/D-3. IAEA, Vienna.

Petrov, D.P., Filippov, N.V., Filippova, T.I. & Khrabrob, V.A. [1960] - 'Plasma Physics and the Problems of Controlled Thermonuclear Reactions' Vol.IV. Pergamon Inc., London.

Post, R.S. [1973] - Columbia Univ., N.Y. Plasma Laboratory Report No.59.

Potter, D.E. [1970] - Thesis, Imperial College of Science and Technology, London.

Potter, D.E. [1971] - Phys. Fluids, 14 : 1911.

Potter, D.E. & Haines, M.G. [1971] - Proc. of 4th Conf. on Plasma Physics and Controlled Nuclear Fusion Research, Madison, N.J. June 17-23. CN-28/D-8. IAEA, Vienna.

Salpeter, E.E. [1960] - Phys. Rev., 120 : 1528.

Samuelli, M., Luzzi, G. & Maisonnier, C. [1971] - Bull. Am. Phys. Soc., 15 : 1463.

Spitzer Jr., L. [1956] - 'Physics of Fully Ionised Gases' p.83. Interscience Publishers Inc., N.Y.

Theus, R.B., McGarry, W.I. & Beach, L.A. [1966] - Nucl. Phys., 80 : 273.

Toepfer, A.J., Smith, D.R. & Beckner, E.H. [1971] - Phys. Fluids, 11 : 52.

USAEC-LASL [1966] - Seminar on Intense Neutron Sources. Conf-660925.

Van Paassen, H.L.L., Vandre, R.H. & White, R.S. [1970] - Phys. Fluids, 13 : 2606.

Vasileva, R.P., Pergament, M.I. & Yaroslavsky, A.I. [1969] - Proc. of 3rd Conf. on Plasma Physics and Nuclear Fusion. Nuclear Fusion Special Suppl. Novosibirsk, August 1968. p.129 (Translation) IAEA, Vienna.

9. SOURCES OF FIGURES AND TABLES

Most of the figures used in this review are taken from other sources. In each case acknowledgements are made to authors, journals and publications, and the figure and table numbers used in the original texts are cited.

Table 1 Bernstein, M.J., Lee, C.M. & Hai, F. [1971] - *Phys. Rev. Lett.*, 27 : 844. *Table I.*

Table 2 — Peacock, N.J., Hobby, M.G. & Morgan, P.D. [1971] - Proc. of 4th Conf. on Plasma Physics and Controlled Nuclear Fusion Research, Madison, N.J. June 17-23. CN-28/D-3. IAEA, Vienna. *Table 2.*

Table 3 — Author of this report. *(Based on Bernstein & Hai 1971)*

Table 4 — Lee, J.H., Shomo, L.P., Williams, M.D. & Hermansdorfer, H. [1971] - *Phys. Fluids,* 14 : 2217. *Table 1.*

Table 5. — Lee, J.H., Shomo, L.P., Williams, M.D. & Hermansdorfer, H. [1971] - *Phys. Fluids,* 14 : 2217. *Table 2 (omitting the last column).*

Figure 1 — Mather, J.W. & Bottoms, P.J. [1968] - *Phys. Fluids,* 11 : 611. *Figure 1.*

Figure 2 — Butler, T.D., Henins, I., Jahoda, F.C., Marshall, J. & Morse, R.L. [1969] - *Phys. Fluids,* 12 : 1904. *Figure 1.*

Figure 3 — Author of this report.

Figure 4(a) — Mather, J.W. [1965] - *Phys. Fluids,* 8 : 366. *Figure 4.*

Figure 4(b) — Lie, T.N., Ali, A.W., Maclean, E.A. & Kolb, A.C. [1967] - *Phys. Fluids,* 10 : 1545. *Figure 8.*

Figure 4(c) — Fishman, F.J. & Petscheck, H. [1962] - *Phys. Fluids,* 5 : 632. *Figure 3.*

Figure 4(d) — Butler, T.D., Henins, I., Jahoda, F.C., Marshall, J. & Morse, R.L. [1969] - *Phys. Fluids,* 12 : 1904. *Figure 5.*

Figure 5(a) — Keck, J.C. [1962] - *Phys. Fluids,* 5 : 630. *Figure 3.*

Figure 5(b) — Lie, T.N., Ali, A.W., Maclean, E.A. & Kolb, A.C. [1967] - *Phys. Fluids,* 10 : 1545. *Figure 7.*

Figure 5(c) — Fishman, F.J. & Petscheck, H. [1962] - *Phys. Fluids,* 5 : 632. *Figure 2.*

Figure 5(d) — Butler, T.D., Henins, I., Jahoda, F.C., Marshall, J. & Morse, R.L. [1969] - *Phys. Fluids,* 12 : 1904. *Figure 6.*

Figure 6(a) — Butler, T.D., Henins, I., Jahoda, F.C., Marshall, J. & Morse, R.L. [1969] - *Phys. Fluids,* 12 : 1904. *Figure 11.*

Figure 6(b) — Butler, T.D., Henins, I., Jahoda, F.C., Marshall, J. & Morse, R.L. [1969] - *Phys. Fluids,* 12 : 1904. *Figure 7.*

Figure 7 — Mather, J.W. & Bottoms, P.J. [1968] - *Phys. Fluids,* 11 : 611. *Figure 3.*

Figure 8 — Mather, J.W. & Bottoms, R.J. [1968] - *Phys. Fluids,* 11 : 611. *Figure 4.*

Figure 9(a) Mather, J.W. [1965] - *Phys. Fluids,* 8 : 366. *Figure 9.*

Figure 9(b) Mather, J.W. [1965] - *Phys. Fluids,* 8 : 366. *Figure 10.*

Figure 10(a) Toepfer, A.J., Smith, D.R. & Beckner, E.H. [1971] - *Phys. Fluids,* 14 : 52. *Figure 6.*

Figure 10(b) Toepfer, A.J., Smith, D.R. & Beckner, E.H. [1971] - *Phys. Fluids,* 14 : 52. *Figure 4.*

Figure 10(c) Toepfer, A.J., Smith, D.R. & Beckner, E.H. [1971] - *Phys. Fluids,* 14 : 52. *Figure 3.*

Figure 11(a) Peacock, N.J., Hobby, M.G. & Morgan, P.D. [1971] - Proc. of 4th Conf. on Plasma Physics and Controlled Nuclear Fusion Research. Madison, N.J. June 17-23. CN-28/D-3. IAEA, Vienna. *Figure 3.*

Figure 11(b) Peacock, N.J., Hobby, M.G. & Morgan, P.D. [1971] - Proc. of 4th Conf. on Plasma Physics and Controlled Nuclear Fusion Research, Madison, N.J. June 17-23. CN-28/D-3. IAEA, Vienna. *Figure 7.*

Figure 12(a) Toepfer, A.J., Smith, D.R. & Beckner, E.H. [1971] - *Phys. Fluids,* 14 : 52. *Figure 8.*

Figure 12(b) Bernstein, M.J. & Hai, F. [1971] - *Phys. Fluids,* 14 : 1010. *Figure 8.*

Figure 13(a) Patou, C. [1970] - *J. de Phys.,* 31 : 339. *Figure 9.*

Figure 13(b) Patou, C. [1970] - *J. de Phys.,* 31 : 339. *Figure 10.*

Figure 13(c) Patou, C. [1970] - *J. de Phys.,* 31 : 339. *Figure 11.*

Figure 14 Mather, J.W., Bottoms, P.J., Carpenter, J.P., Williams, A.H. & Ware, K.D. [1971] - Proc. of 4th Conf. on Plasma Physics and Controlled Nuclear Fusion Research, Madison, N.J. June 17-23. CN-28/D-5. IAEA, Vienna. *Figure 6.*

Figure 15 Author of this report.

Figure 16(a) Van Paassen, H.L.L., Vandre, R.H. & White, R.S. [1970] - *Phys. Fluids,* 13 : 2606. *Figure 8.*

Figure 16(b) Van Paassen, H.L.L., Vandre, R.H. & White, R.S. [1970] - *Phys. Fluids,* 13 : 2606. *Figure 9.*

Figure 17(a) Patou, C. [1970] - *J. de Phys.,* 31 : 339. *Figure 7.*

Figure 17(b) Peacock, N.J., Wilcock, P.D., Speer, R.J. & Morgan, P.D. [1968] - Proc. of 3rd Conf. on Plasma Physics and Controlled Nuclear Fusion Research. Novosibirsk, August 1968. CN-24/G-4. IAEA, Vienna. *Figure 8.*

Figure 18 Beckner, E.H. [1966] - *Appl. Phys.*, 37 : 4944. *Figures 10 & 11.*

Figure 19(a) Peacock, N.J., Hobby, M.G. & Morgan, P.D. [1971] - Proc. of 4th Conf. on Plasma Physics and Controlled Nuclear Fusion Research. Madison, N.J. June 17-23. CN-28/D-3. IAEA, Vienna. *Figure 12.*

Figure 19(b) Grateau, P., Luzzi, G., Maisonnier, C., Pecorella, F., Rager, J.P., Robouch, B.V. & Samuelli, M. [1971] - Proc. of 4th Conf. on Plasma Physics and Controlled Nuclear Fusion Research. Madison, N.J. June 17-23. CN-28/D-1. IAEA, Vienna. *Figure 8.*

Figure 20(a) Bernstein, M.J. & Hai, F. [1971] - *Phys. Fluids,* 14 : 1010. *Figure 3.*

Figure 20(b) Patou, C., Simonnet, A. & Watteau, J.P. [1968] - *J. de Phys.*, 29 : 973. *Figure 10.*

Figure 21(a) Maisonnier, C., Gourlan, C., Luzzi, G., Papagno, L., Pecorella, F., Rager, J.P., Robouch, B.V. & Samuelli, M. [1971] - Proc. of 4th Conf. on Plasma Physics and Controlled Nuclear Fusion Research. Madison, N.J. June 17-23. CN-28/D-2. IAEA, Vienna. *Figure 1.*

Figure 21(b) Patou, C. [1970] - *J. de Phys.*, 31 : 339. *Figure 14.*

Figure 21(c) Patou, C. [1970] - *J. de Phys.*, 31 : 339. *Figure 12.*

Figure 22 Bernard, A., Cesari, G., Coudeville, A., Jolas, A., de Mascureau, J. & Watteau, J.P. [1971] - Proc. of 4th Conf. on Plasma Physics and Controlled Nuclear Fusion Research. Madison, N.J. June 17-23. CN-28/D-4. IAEA, Vienna. *Figure 3.*

Figure 23(a) Bernstein, M.J., Meskan, D.A. & Van Paassen, H.L.L. [1969] - *Phys. Fluids,* 12 : 2193. *Figure 7.*

Figure 23(b) Bernstein, M.J. & Hai, F. [1971] - *Phys. Fluids,* 14 : 1010. *Figure 6.*

Figure 23(c) Bernstein, M.J., Meskan, D.A. & Van Paassen, H.L.L. [1969] - *Phys. Fluids,* 12 : 2193. *Figure 8.*

Figure 24(a) Maisonnier, C., Gourlan, C., Luzzi, G., Papagno, L., Pecorella, F., Rager, J.P., Robouch, B.V. & Samuelli, M. [1971] - Proc. of 4th Conf. on Plasma Physics and Controlled Nuclear Fusion Research. Madison, N.J. June 17-23. CN-28/D-2. IAEA, Vienna. *Figure 4.*

Figure 24(b) Patou, C. [1970] - *J. de Phys.*, 31 : 339. *Figure 13.*

Figure 25(a) Patou, C. [1970] - *J. de Phys.*, 31 : 339. *Figure 15.*

Figure 25(b) Patou, C. [1970] - *J. de Phys.*, 31 : 339. *Figure 16.*

Figure 25(c) Patou, C. [1970] - *J. de Phys.*, 31 : 339. *Figure 17.*

Figure 26 Maisonnier, C., Gourlan, C., Luzzi, G., Papagno, L., Pecorella, F., Rager, J.P., Robouch, B.V. & Samuelli, M. [1971] - Proc. of 4th Conf. on Plasma Physics and Controlled Nuclear Fusion Research. Madison, N.J. June 17-23. CN-28/D-2. IAEA, Vienna. *Figure 8.*

Figure 27(a) Potter, D.E. & Haines, M.G. [1971] - Proc. of 4th Conf. on Plasma Physics and Controlled Nuclear Fusion Research. Madison, N.J. June 17-23. CN-28/D-8. IAEA, Vienna. *Figure 1.*

Figure 27(b) Potter, D.E. & Haines, M.G. [1971] - Proc. of 4th Conf. on Plasma Physics and Controlled Nuclear Fusion Research. Madison, N.J. June 17-23. CN-28/D-8. IAEA, Vienna. *Figure 3.*

Figure 28(a) Potter, D.E. & Haines, M.G. [1971] - Proc. of 4th Conf. on Plasma Physics and Controlled Nuclear Fusion Research. Madison, N.J. June 17-23. CN-28/D-8. IAEA, Vienna. *Figure 2.*

Figure 28(b) Potter, D.E. & Haines, M.G. [1971] - Proc. of 4th Conf. on Plasma Physics and Controlled Nuclear Fusion Research. Madison, N.J. June 17-23. CN-28/D-8. IAEA, Vienna. *Figure 4.*

Figure 29(a) Bernstein, M.J. [1970] - *Phys. Fluids,* 13 : 2858. *Figure 1(d), (e), (f).*

Figure 29(b) Bernstein, M.J. [1970] - *Phys. Fluids,* 13 : 2858. *Figure 2.*

Figure 29(c) Bernstein, M.J. [1970] - *Phys. Fluids,* 13 : 2858. *Figure 4.*

Figure 30(a) Bernstein, M.J. & Comisar, G.G. [1972] - *Phys. Fluids,* 15 : 700. *Figure 6.*

Figure 30(b) Bernstein, M.J. & Comisar, G.G. [1972] - *Phys. Fluids,* 15 : 700. *Figure 7.*

Figure 31(a) Bernstein, M.J. & Comisar, G.G. [1972] - *Phys. Fluids,* 15 : 700. *Figure 8.*

Figure 31(b) Bernstein, M.J. & Comisar, G.G. [1972] - *Phys. Fluids,* 15 : 700. *Figure 9.*

Figure A1 Potter, D.E. [1971] - *Phys. Fluids,* 14 : 1911. *Figure 1.*

Figure A2 Potter, D.E. [1971] - *Phys. Fluids,* 14 : 1911. *Figure 5.*

Figure A3 Potter, D.E. [1971] - *Phys. Fluids,* 14 : 1911. *Figure 6.*

Figure A4 Potter, D.E. [1971] - *Phys. Fluids,* 14 : 1911. *Figure 9.*

Figure A5 Potter, D.E. [1971] - *Phys. Fluids,* 14 : 1911. *Figure 10.*

Figure A6 Potter, D.E. [1971] - *Phys. Fluids,* 14 : 1911. *Figure 11.*

APPENDIX A

A TWO-FLUID MODEL OF THE PLASMA FOCUS GUN

A more detailed description of the model for the plasma focus that has been constructed by D.E. Potter of The Imperial College of Science and Technology, London, is given here [Potter 1970, 1971]. Only the assumptions and the results will be given here, without justification for the assumptions.

The basis of the model is a two-fluid description of the electrons and ions, in which no account is taken of any neutral component, *i.e.* total ionisation is assumed. Cylindrical symmetry is also assumed so that all dependent variables are functions of the radius r, the distance along the electrode z and the time t. The thermal energy densities, $\rho\varepsilon_i$ and $\rho\varepsilon_e$, are functions of the temperatures, T_i and T_e as

$$\varepsilon_{i,e} = T_{i,e}/(\gamma - 1) \quad ,$$

where γ is the ratio of specific heats and assumed constant. The system can then be described by six variables

ρ = density,

ρy = centre of mass momentum,

B_θ = azimuthal magnetic field, and

$\rho\varepsilon_i$ and $\rho\varepsilon_e$ = thermal energy densities for the ions and the electrons respectively.

Since the Hall parameter $\beta = \omega_c \tau_i$ (where ω_c is the cyclotron frequency and τ_i is the collision time of the particle with the ions) is of the order unity or greater at some stages of the focus, cyclotron orbiting effects must be taken into account. Since the magnetic field is always perpendicular to the r - z plane, there is no flow along the field lines and isotropy is maintained in the r - z plane. Therefore, only one heat conductivity coefficient for each of the fluids is required.

The boundary conditions are summarised in Figure A1 and the domain of dependence is coupled to an external LC circuit.

The fluid equations are integrated using a second-order two-step Lax-Wendorff method on an Eulerian mesh. A finer mesh is introduced at the end of the centre electrode to improve the resolution during the pinch stage.

The geometry and initial conditions for the following results are:

Radius of inner electrode	r_1 = 2.5 cm
Radius of outer electrode	r_2 = 5.0 cm
Length of inner electrode	10.0 cm
Capacitance of external condenser	C = 40 μF
External inductance	L_e = 15 nH
Gas	deuterium
Initial temperature	$T_e = T_i$ = 2 eV
Voltage on condenser	V = 40, -40 kV
Ambient filling density	4.5×10^{16}
	$n_e = 1.8 \times 10^{17}$ cm^{-3}
	1.2×10^{16}
Number of mesh points	2025

The calculation is started with a small current flowing on the insulator B (Figure A1). A shock develops between the electrodes and reaches an equilibrium configuration in around 0.4 μsec. The equilibrium shape and velocity is very similar to the snowplough calculation in Section 2. A typical shock structure at a radius of 2.5 mm from the centre electrode at this stage is shown in Figure A2. We notice that the compression and temperature rise occur approximately 5 mm in front of the rise in the magnetic field (the current sheath is a thin layer in the rising $\underset{\sim}{B}$ region). The temperature maximum in the shock is 20 to 30 eV.

The shock structure during the collapse phase prior to meeting on the axis at an axial distance of 5.6 mm from the electrode is shown in Figure A3. The general structure is similar to that for the current sheath between the electrodes. The ion temperature is lower than the electron temperature because ohmic heating contributes mainly to the internal energy of the electrons owing to the long equipartition time. Notice the very large collapse velocity, up to 60×10^6 cm sec^{-1} and the increased magnetic field - a factor of two greater than during the run-down stage.

Figure A4 shows the structure at the beginning of the compression on the axis as a function of radius at an axial position 7.5 mm from the electrode. Note that within a 2 mm radius of the axis the ion temperature is around 1 keV and twice the electron temperature. The main contribution to the extra ion temperature appears to be the ion viscosity. Also the temperatures are somewhat higher away from the axis owing to the lower heat

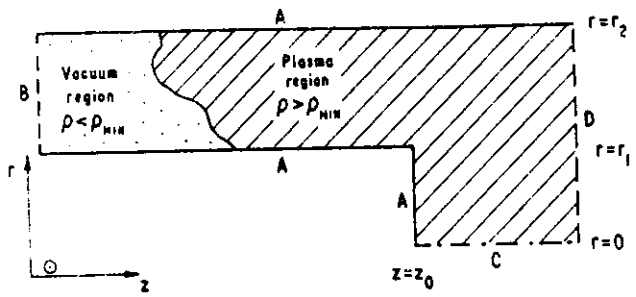

FIGURE A1

Domain and boundaries in the focus calculation. The domain is divided into two regions by an intemally moving boundary. In the vacuum region no currents are permitted to flow, and the magnetic field is defined by the total current flowing in the external circuit. The domain is bounded by: (A) perfectly conducting impermeable walls ($V_\perp = 0$, $E_{11} = 0$); (B) intemally conducting wall, with a perfect insulating surface ($j_\perp = 0$, $v_\perp = 0$); (C) the axis; (D) free flow symmetry boundary. (Source: Potter 1971)

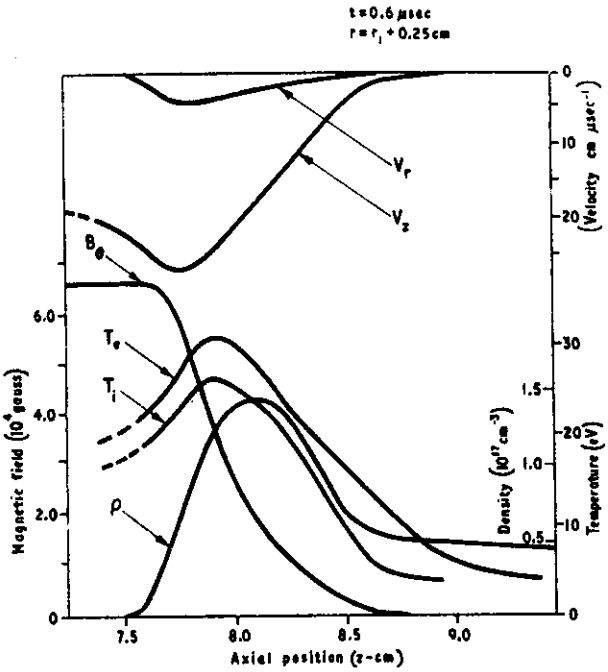

FIGURE A2

Dependent variables through the shock in the run-down stage. The compression ratio remains small as flow parallel to the current sheet removes plasma : consequently the shock is strongly supersonic and the electrons are preferentially heated through Joule heating. (Source: Potter 1971)

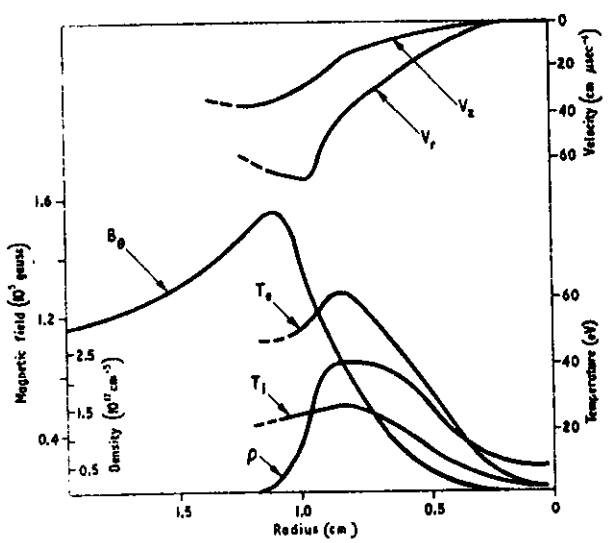

FIGURE A3

Shock structure in the collapse phase prior to meeting the axis at an axial position 0.56 cm from the anode. Unlike the z pinch, momentum flow parallel to the current sheet ($\sim V_z$) acts as a sink for the snow-plowed plasma and the compression ratio in the shock remains low. The shock, therefore, remains strongly supersonic, and the electrons are preferentially heated by Joule heating. (Source: Potter 1971)

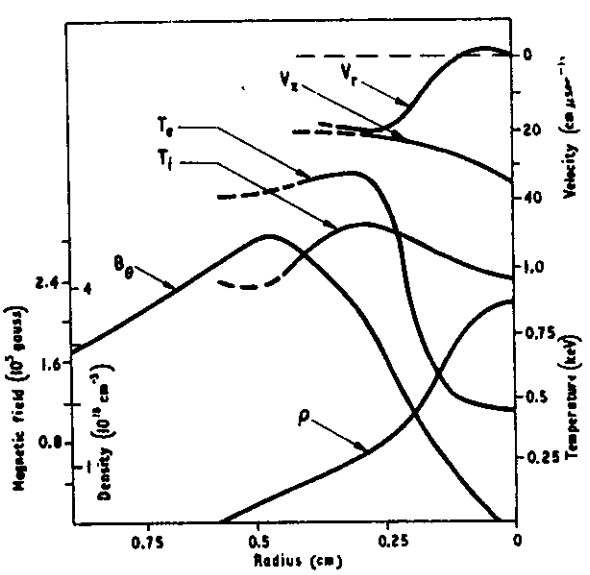

FIGURE A4

Radial dependence of the variables during the initial compression on the axis in the plasma focus. Adiabatic heating increases the electron and ion temperatures while viscous heating preferentially heats the ions. Temperatures are higher on the outside of the pinch due to the limitation of heat conductivities through cyclotron orbiting ($t = 0.820$ μsec).
(Source: Potter 1971)

conductivity at larger magnetic fields. The mesh size smears out the pinch somewhat, and averages the temperature and density so that a finer mesh would probably give sharper gradients and higher values in small regions.

The axial structure (Figure A5) at a slightly later time shows the pinch has occurred only within the first 10 mm so far, confirming its non-cylindrical nature. The axial velocity rises to over 60 x 10^6 cm sec^{-1} owing to the axial pressure gradients and this carries much of the plasma out of the pinch region. A high density cold region exists at the end of the anode acting as a source of plasma.

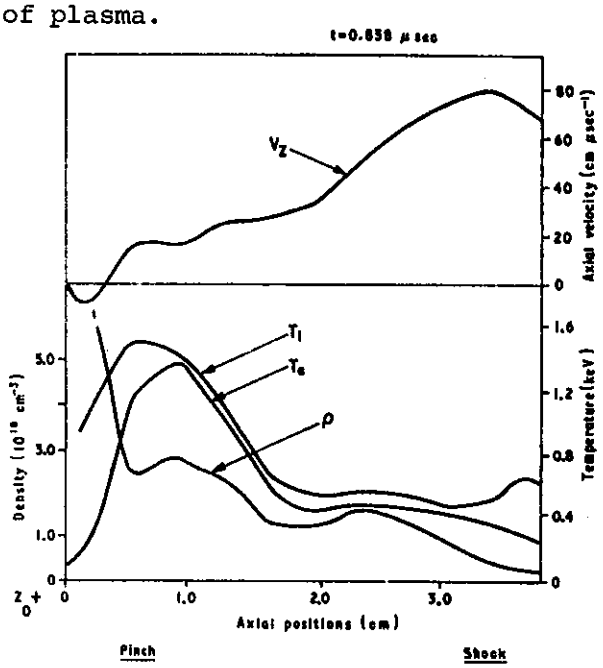

FIGURE A5

Axial structure in the plasma focus (time $t = t_{pinch} + 10$ nsec). Three features are apparent: a cold anode source, a hot pinch region, and a fast axial shock. Viscous heating insures a higher ion than electron temperature particularly in the axial shock.
(Source: Potter 1971)

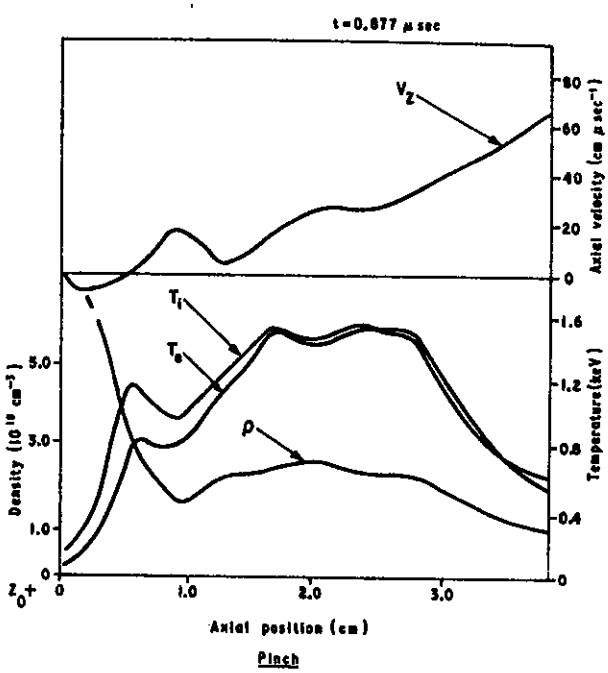

FIGURE A6

Axial structure in the plasma focus (time $t = t_{pinch} + 49$ nsec). At later times the hot pinch region is more than a centimeter long and axial flow occurs. The axial shock has moved downstream (outside the diagram) a considerable distance while the pinch does not translate significantly.
(Source: Potter 1971)

Thirty-nine nsec later (Figure A6) a similar situation exists, but the pinched column is now well established and about 30 mm long. Axial flow occurs through the pinched region with a typical velocity of 30 x 10^6 cm sec^{-1} with increasing velocities beyond the pinch due to the nozzle effect of the non-cylindrical pinch.

The m = 0 instability which disrupts the pinch starts to grow 40 to 50 nsec after the compression. The time is a factor of ten longer than the usual pinch theory prediction and is probably caused by ion viscosity damping and the non-cylindrical geometry. (Other instabilities cannot arise in the model owing to the assumed azimuthal symmetry.) At later times the results of the

calculation must be treated with caution owing to the finite mesh and its inability to describe the turbulent conditions after the growth of the instability.

Butler *et al.* [1969] give the dynamics of the shock with a fluid model using the particle-in-cell method for integrating the equations, but they do not include heat conduction or ion viscosity. Hence, only the general dynamics of the shock can be described, but not the detailed shock structure. Dyachenko & Imshennnik [1969] give a similar calculation, but use a single fluid model.

APPENDIX B

RECENT DEVELOPMENTS

B1. ELECTRON AND ION TEMPERATURES

Recently reported investigations have given new measurements of the electron and ion temperatures by laser scattering during the 50 nsec life of the dense pinch phase [Peacock, *et al.* 1972]. These give $T_e > T_D$ from the shape of the scattering profile and are consistent with $T_e \sim 2$ keV, $T_D \sim 0.7$ keV and $T_{Ne} \sim 9$ keV (the plasma was seeded with a few per cent neon). With interferogram values of density 2×10^{19} cm^{-3}, there will be an output of 10^7 neutrons under such conditions. This is consistent with the neutron measurements by Maisonnier, *et al.* [1972]; they obtained a small neutron pulse, ~ 5 per cent of the total output, during the dense pinch phase and the main output after the pinch broke up. The electron temperature is inconsistent with X-ray spectrum measurements of Bernstein [1972] who obtained $T_e \sim 0.4$ keV.

Maisonnier *et al.* [1972] state that the main neutron pulse occurs from a low density plasma heated by turbulence. Further evidence for turbulence during the dark phase was obtained by infrared emission measurements and infrared laser scattering [Post 1973]. Both thermal and non-thermal emissions were found, together with very bright filaments less than 100 μm diameter; this is evidence for local instabilities. Gross turbulence was not found, but turbulence with $\Delta n/n \sim 0.1$ is consistent with the results.

B2. X-RAYS

A large anisotropy in the emission of X-rays with energy greater than 200 keV has been found with a peak between 38° and 75° to the axis and an intensity 75 per cent greater than along the axis [Jalufka & Lee 1972].

B3. NEUTRON SPECTRUM

The comparison of neutron spectra in the axial direction for operation at 20 kV and 40 kV showed twofold increase in the displacement of the energy peak from 2.45 MeV toward higher energies at 40 kV. At the higher voltage, the highest energy neutrons sometimes form a separate peak, giving further evidence in favour of two mechanisms being involved in the neutron production [Lee & McFarland 1972].

In the radial direction, two distinct types of neutron spectrum were found; one was symmetrical with a FWHM of 350 keV and the other asymmetrical with a FWHM of 550 keV. On the low energy side of the peak the widths were the same. If the asymmetrical distributions were produced by an added

contribution, subtracting the symmetrical spectrum (after normalisation) would give this added contribution. The conclusion is that there are two velocity distributions during the life of the focus. One of these is two-dimensional, in a plane perpendicular to the axis, with an upper average energy limit for the ions of 60 keV; the other is one-dimensional and axial, with an average energy for the ions of at least 0.3 MeV. The density of the ions must be less than 10^{19} cm^{-3} to give the correct total neutron emission [Conrads *et al.* 1972].

B4. COMPUTER CALCULATIONS

Ion kinematic calculations with three-dimensional equations of motion, similar to two-dimensional calculations of Bernstein [1970], yield a strong free-streaming acceleration of the ions within a Larmor radius of the axis [Gary & Hohl 1973]. The model extends that of Bernstein [1970] in the following way:

- the particles have an initial spatial as well as initial Maxwellian velocity distribution, and
- $E_z = 0$ outside the plasma.

A recalculation of Bernstein's model (*i.e.* $E_z(r = 0,t) = 0$) in three dimensions gives similar results for the accelerated number of ions.

The present model uses the different assumption about the electric field because it was considered more appropriate for a coaxial current flow, with a changing current (from Lenz' Law). This model produces run-away ions along the axis away from the anode. It also produces run-away electrons towards the anode (but there will be only $(me/mi)^{\frac{1}{2}}$ as many electrons) which can give rise to the intense X-ray burst from the anode. The number of ions accelerated (and hence the possibility of accelerating electrons at all) is not strongly affected by the collision frequency in this model.